Magnetic Properties of Heisenberg Antiferromagnetic EuTe/PbTe Superlattices

by

James J. Chen
B.A., University of California at Berkeley
(1991)

Submitted to the Department of Physics
in partial fulfillment of the requirements for the degree of

Doctor of Philosophy

at the

MASSACHUSETTS INSTITUTE OF TECHNOLOGY

June 1996

Author .....
Department of Physics
May 24, 1996

Certified by .....
Mildred S. Dresselhaus
Institute Professor
Thesis Supervisor

Accepted by .....
George Koster
Chairman, Departmental Committee on Graduate Students

Magnetic Properties of Heisenberg Antiferromagnetic EuTe/PbTe Superlattices

by

James J. Chen

B.A., University of California at Berkeley

(1991)

Submitted to the Department of Physics
on May 24, 1996, in partial fulfillment of the
requirements for the degree of
Doctor of Philosophy

Abstract

High quality MBE-grown EuTe/PbTe superlattices (SLs) with EuTe thicknesses ranging from one atomic monolayer to seven atomic layers per SL period have recently been made available. High resolution x-ray diffraction measurements and cross-sectional TEM images on these SL samples confirm the SL structure.

Bulk EuTe with its highly symmetric rocksalt structure, spherically symmetric Eu^{2+} $^8S_{7/2}$ ground state and zero magnetic anisotropy is considered to be an ideal Heisenberg antiferromagnet. The small lattice mismatch between EuTe and PbTe allows EuTe in our SLs to retain the same isotropic magnetic couplings as in bulk EuTe. In addition, our SL samples provide a good realization of a 2D Heisenberg antiferromagnet, since (1) the EuTe thicknesses in each SL period are on the order of several atomic monolayers; (2) the non-magnetic PbTe layers separating neighboring EuTe layers are sufficiently thick to prevent any inter-period magnetic coupling. Thus, the study of the magnetic properties of EuTe/PbTe SLs is of great interest, since they provide an experimental realization of an ideal 2D Heisenberg antiferromagnet with localized spins, isotropic exchange interactions and no inter-period coupling.

Having SLs with different EuTe layer thicknesses ranging from one to seven monolayers makes it possible to study the behavior of the magnetization and susceptibility as a function of the layer thickness. High magnetic field $M(H)$ studies show that EuTe/PbTe SLs cross from a canted antiferromagnetic phase to a spin-aligned paramagnetic phase in high fields at low temperatures just like bulk EuTe, although the phase boundary moves toward lower fields and temperatures in the H-T plane as the EuTe thickness is decreased. The temperature-dependent susceptibility measurements show strong anisotropy between the in-plane and out-of-plane susceptibilities, starting at temperatures slightly above T_c and extending to near T=0 K. The isotropic exchange couplings and the absence of magnetic anisotropy in EuTe/PbTe SLs im-

plied by our $M(T, H)$ studies lead us to believe that the dipolar interaction is the main source of anisotropy. Finally, Monte Carlo simulations, using a Heisenberg model with dipolar interactions show that these interactions, can stabilize long-range antiferromagnetic order in EuTe/PbTe SLs.

Thesis Supervisor: Mildred S. Dresselhaus
Title: Institute Professor

Acknowledgments

I would like to thank Millie and Gene Dresselhaus for the opportunity to carry out my thesis research in their group. During the past four years, Millie and Gene have introduced me to physics research and to a group of distinguished scientists along the way.

Dr. Gunther Springholz and Professor G. Bauer at Johannes Kepler University, have generously provided me with the superlattice samples to study for this thesis. I hope that I will soon have an opportunity to visit them in Linz.

I would like to thank my thesis committee members, Professor Roshan Aggarwal and Professor John Joannopoulos, for their unfailing encouragement. I know that 'uncle John' would be a good committee member since I had his recitation for my quantum class.

I would also like to thank Drs. Tom Giebultowicz and Valerie Nunez for teaching me neutron scattering. I want to thank Professor Lourdes Salamanca-Riba at University of Maryland for explaining the TEM studies she and her students have carried out on the same superlattice samples we studied at MIT.

Dr. Lorenzo Bergomi, from CEA, Saclay France is both a collaborator and a friend. His decisive contribution in defining the nature of magnetic phase transitions taking place in the superlattices is noted in Chapter 7.

Help from past and present members of MGM is gratefully acknowledged, with special mention to Drs. Alex Fung and Gillian Reynolds, Sandra Brown, Lyndon Hicks, Manyalibo J. Matthews, Boris Pevzner, and Sun Xiang-Zhong. Jordina Vidal is very special due to the proximity effect. Among many things, I remember that she has once summarily dismissed that all my questions to her were too easy. Nevertheless, I am impressed by her talents and cheerfulness.

I want to acknowledge my friends Rodrigo Capaz, Feng Qiang (MK), Fan Shan-Hui, Hu Wen, Arthur Mateos (Part II study partner, we were going to write a book together),Welles Morgado, Chris Rost, Partha Saha, and Paul Westbrook whom I have spent much time with after school.

Finally, I want to thank my parents Dr. Chen Zhong-Ying and Dr. Zhang Yin who have given me all their love without any diversion to my siblings (and I have none).

Contents

1 Magnetism in Reduced Dimensions **20**

1.1 Introduction 20

1.2 The EuTe Hamiltonian 22

1.3 Heisenberg Antiferromagnetic EuTe/PbTe SLs 23

1.4 Thesis Outline 24

1.5 Special Notation 25

2 Chemical Structure of EuTe/PbTe Superlattices **28**

2.1 Introduction 28

2.2 MBE Growth of EuTe/PbTe Superlattices 29

2.3 In-situ STM 30

2.4 Ex-situ TEM 31

2.5 X-ray Diffraction 32

2.6 Summary 35

3 Spin Structure of EuTe in Superlattices **46**

3.1 Introduction 46

3.2 Triple-Axis Spectrometer 47

3.3 Scattering Geometry 48

3.4 Experimental Conditions 49

3.5 Experimental Results 50

3.5.1 Zero Field Diffraction Experiments 50

3.5.2 Field-Dependent Diffraction Experiments 52

3.6 Computer Simulation 53
3.7 Summary 56

4 Low Field Magnetization **71**
4.1 Introduction 71
4.2 Experimental Setup 72
4.2.1 Background Signal 73
4.2.2 Magnetic Units 74
4.3 Magnetic Anisotropy 74
4.4 $M(T, H)$ near T_c 75
4.5 Determine T_c for SLs 77
4.6 Geometric Effect in $M(T)$ 78
4.7 Mean-Field Analysis of $M(T)$ 79
4.7.1 ξ=odd SLs 79
4.7.2 ξ=even SLs 80
4.8 Mean-Field Analysis of T_c 81
4.9 Discussion 82
4.9.1 Comparisons Between Bulk EuTe and EuTe SLs 83
4.9.2 Relation Between Structural and Magnetic Measurements . . . 84
4.10 Summary 85

5 High Field Magnetization **105**
5.1 Introduction 105
5.2 Experimental Results 106
5.3 Data Analysis 108
5.4 Summary 110

6 Zero Field Susceptibility **118**
6.1 Introduction 118
6.2 Experimental Setup 119
6.3 Frequency Dependence and Linearity 120

6.4 Temperature Dependence of Susceptibility 121
6.4.1 EuTe(1)/PbTe(3) SL 121
6.4.2 SL EuTe(2)/PbTe(6) 122
6.4.3 SL EuTe(3)/PbTe(9) 123
6.4.4 SL EuTe(4)/PbTe(12) 124
6.4.5 SL EuTe(5)/PbTe(15) 124
6.4.6 SL EuTe(6)/PbTe(18) 125
6.4.7 SL EuTe(7)/PbTe(21) 125
6.5 Discussion 126
6.5.1 Anisotropy in the Susceptibility 126
6.5.2 Divergent χ_{in} and T_c 128
6.6 Summary 128

7 Monte Carlo Simulation **146**
7.1 Introduction 146
7.2 Monte Carlo Method 148
7.3 Metropolis Algorithm 148
7.4 Monte Carlo and Error Analysis 150
7.5 Program Validation 152
7.6 Ising Model 153
7.6.1 Input Parameters 153
7.6.2 $M_{rms}(T)$ 154
7.6.3 $\chi_{\|}(T)$ 155
7.6.4 $M_{rms}(T)$ revisited 157
7.7 Heisenberg Model with Dipolar Coupling 157
7.7.1 Heat-bath Method 158
7.7.2 Input Parameters 159
7.7.3 Results on $\chi_{in}(T)$ and $\chi_{out}(T)$ 160
7.8 Clock Model 162
7.8.1 Input Parameters 163

7.8.2 $\chi_\perp(T)$ and $\chi_\parallel(T)$ 163
7.9 Comment on J_1 and J_2 165
7.10 Summary 166

8 Conclusions and Future Work **188**
8.1 Conclusions 188
8.2 Indications for Future Research 189

List of Figures

1-1 Electronic structure of EuTe, reproduced from Ref.[15] 26

1-2 Experimental and computational methods employed in our magnetic studies of EuTe/PbTe superlattices. 27

2-1 STM image of a PbTe epitaxial layer on BaF_2 (111) by G. Springholz, N. Frank, and G. Bauer.[25] 37

2-2 STM image of a 20 ML thick EuTe epitaxial layer on PbTe (111) by G. Springholz, N. Frank, and G. Bauer.[25] 38

2-3 STM image ($2 \times 0.5\ \mu m^2$) of a 25 ML thick EuTe epitaxial layer on PbTe (111). The arrow indicates the end point of a threading dislocation. Inset: Schematic illustration of the strain relaxation process due to misfit dislocation formation by the glide of a pre-existing threading dislocation.[25] 39

2-4 Cross sectional TEM image of a EuTe(5)/PbTe(22) superlattice sample by M. Shima and Lourdes Salamanca-Riba.[29] 40

2-5 $(\bar{1}\bar{1}2)$ high resolution lattice image of the EuTe(3.5)/PbTe(9) superlattice. The upper left inset shows the electron diffraction pattern of the same SL sample by M. Shima and Lourdes Salamance-Riba.[29] . . . 41

2-6 A schematic drawing of the cross sectional view of an EuTe(3)/PbTe(9) superlattice. 42

2-7 The (222) (Cu $K_{\alpha 1}$ radiation) Bragg x-ray diffraction patterns for the EuTe(3)/PbTe(9) (a), EuTe(4)/PbTe(12) (b), and EuTe(5)/PbTe(15) (c) superlattice structures (full lines). The dashed lines represent calculated diffractograms using the structural parameters obtained from the strain analysis. Both the x-ray data and their analysis were carried out by Dr. G. Springholz and Mr. C. Pichler. 43

2-8 The scattering geometry used in the x-ray diffraction measurement. Both the scattering plane (SP) and the scattering vector ($\vec{Q}$) are normal to the sample surface, giving information about the atomic arrangements in the 111 direction. 44

3-1 Spin arrangements of type II antiferromagnets. 58

3-2 A schematic layout of a triple-axis spectrometer. 59

3-3 The scattering geometry used in the magnetic neutron diffraction experiments. Both the scattering plane (SP) and the scattering vector ($\vec{Q}$) are normal to the sample surface, so that scattering experiments with this geometry provide information on the spin ordering within the (111) plane spin arrangement along the 111 direction between adjacent (111) planes. The scattering plane is defined by the incident neutron and the scattered neutron beam directions. 60

3-4 Diffraction scans at T=4.2 K for $\vec{Q}$ along the 111 direction through the position of the $(\frac{1}{2}, \frac{1}{2}, \frac{1}{2})$ AF reflection (Q_z=0.84 $Å^{-1}$) for an EuTe(2)/PbTe(6) SL. 61

3-5 Diffraction scans at T=1.8 K along the 111 direction through the position of the $(\frac{1}{2}, \frac{1}{2}, \frac{1}{2})$ AF reflection (Q_z=0.84 $Å^{-1}$) for an EuTe(2)/PbTe(10) SL. 62

3-6 Diffraction scans at T=4.2 K along the 111 direction through the position of the $(\frac{1}{2}, \frac{1}{2}, \frac{1}{2})$ AF reflection (Q_z=0.84 $Å^{-1}$) for EuTe(3)/PbTe(9), EuTe(4)/PbTe(12), EuTe(5)/PbTe(15), and EuTe(6)/PbTe(18) SLs. . 63

3-7 Diffraction scans at T=4.2 K along the 111 axis through the $(\frac{1}{2}, \frac{1}{2}, \frac{1}{2})$ AF reflection position for an EuTe(3)/PbTe(15) SL. The absence of the SL peaks implies absence of the inter-period magnetic coupling. . 64

3-8 Diffraction scan at T=4.2 K along the [111] axis through the (1,1,1) FM reflection position at H=6 T for an EuTe(4)/PbTe(12) SL. 65

3-9 Diffraction scan at T=4.2 K along the 111 axis through both $(\frac{1}{2}, \frac{1}{2}, \frac{1}{2})$ reflection the (1,1,1) reflection positions at H=5 T for an EuTe(5)/PbTe(15) SL. 66

3-10 Neutron scattering from superlattices is like diffracting light from two superimposed diffraction gratings, each with grating separations of d and L, respectively. 67

3-11 A simulated zero field diffraction scan for T< T_c along the 111 axis through the $(\frac{1}{2}, \frac{1}{2}, \frac{1}{2})$ AF reflection point for an EuTe(4)/PbTe(12) SL. 68

3-12 A simulated in-field (with a sufficiently large H field to align all the spins) diffraction scan for T< T_c along the 111 axis through the (1,1,1) reflection point for an EuTe(4)/PbTe(12) SL. 69

4-1 A block diagram for the MPMS5 SQUID system by Quantum Design Inc. 87

4-2 Sample mounting and orientation for magnetization studies. 88

4-3 Normalized magnetization of BaF_2 vs. temperature measured with an external magnetic field H=1000 gauss (a); BaF_2 magnetization vs. magnetic field at T= 5 K (b). 89

4-4 Normalized magnetization of PbTe vs. temperature measured with an external magnetic field H=1000 gauss (a); PbTe magnetization vs. magnetic field at T= 5 K (b). 90

4-5 Spin arrangements of type II antiferromagnets. 91

4-6 Hysteresis magnetization measurements at 4 K for an EuTe(3)/PbTe(9) SL (a), an EuTe(4)/PbTe(12) SL (b), and an EuTe(5)/PbTe(15) SL (c) for the magnetic field perpendicular and parallel to the (111) layer planes. 92

4-7 Magnetization vs. field for two randomly chosen directions (closed triangles represent the measurements in one direction, and the open circles represent the measurements in another direction) within the (111) plane, for the EuTe(3)/PbTe(9) SL sample at T=4.7 K. 93

4-8 M vs. T for an EuTe(1)/PbTe(3) SL sample at H= 8 gauss (a). Same set of data as in (a) but plotted as MT^2 vs. T (b). 94

4-9 Normalized $M(T)$ measurements for an EuTe(2)/PbTe(6) SL (a), an EuTe(3)/PbTe(9) SL (b), an EuTe(4)/PbTe(12) SL (c), an EuTe(5)/PbTe(15) SL (d), an EuTe(6)/PbTe(18) SL (e), and an EuTe(7)/PbTe(21) SL (f). 95

4-10 Normalized $M(T)$ measurements taken with H=1000 gauss for an EuTe epilayer 3.1 μm thick. The magnetization data, expressed in terms of emu per Eu atom, closely approximate the $M(T)$ behavior of a bulk antiferromagnet. 96

4-11 $M(T)$ for an EuTe(4)/PbTe(12) SL with different in-plane H measuring fields. 97

4-12 Normalized $M(T)$ measurements for an EuTe(2)/PbTe(6) SL (a), an EuTe(3)/PbTe(9) SL (b), an EuTe(4)/PbTe(12) SL (c), an EuTe(5)/PbTe(15) SL (d), an EuTe(6)/PbTe(18) SL (e), and an EuTe(7)/PbTe(21) SL (f), measured after FC (open circles) and ZFC (closed circles) cycles. 98

4-13 Asymptotic limits of $M(T \longrightarrow 0)$ for SLs with varying thicknesses of EuTe per SL period measured in the number of magnetic monolayers. 99

4-14 Mean-field fit to the field cooled $M(T)$ data of an EuTe(3)/PbTe(9) SL (a); and an EuTe(5)/PbTe(15) SL (b). The broken lines are Brillouin functions and the solid curves represent the mean-field model containing a biquadratic exchange term. 100

4-15 Temperature dependence of the interface and interior layer magnetizations in an EuTe(4)/PbTe(12) SL obtained by a mean-field calculation including biquadratic coupling. 101
4-16 Mean-field fit to the $M(T)$ of an EuTe(4)/PbTe(12) SL. 102

5-1 Phase diagram of EuTe in the $H - T$ plane, from Ph.D. thesis by R. P. Silberstein at M.I.T., 1978. 112
5-2 Spin-flop transition. 113
5-3 $M(H)$ curves for an EuTe(2)/PbTe(6) SL (a), an EuTe(3)/PbTe(9) SL (b), an EuTe(4)/PbTe(12) SL (c), and an EuTe(5)/PbTe(15) SL (d). 114
5-4 Canted AF (left side) to paramagnetic (right side) boundaries for EuTe/PbTe SLs and bulk EuTe. Values of T_c are given in Table 5.1. . 115
5-5 $M(H)$ curve of antiferromagnets where H_F is the field at the saturation value of the magnetization M_s (a). Directions of sublattice (adjacent (111) planes) magnetizations M_1 and M_2 with respect to H make an angle of θ with respect to the positive y direction (b). 116

6-1 The two principal orientations of the sample with respect to the AC probing field for the χ_{in} (a), and χ_{out} (b) susceptibility measurements. 130
6-2 χ_{in} for an EuTe(6)/PbTe(18) SL measured with a 20 Hz AC magnetic field of h=4 gauss and a static external magnetic field of H=4 gauss (closed circles); χ_{in} for the same sample but measured with a 20 Hz AC field of h=4 gauss and zero nominal static external field (open circles) 131
6-3 Temperature dependence of the χ_{in} for an EuTe(7)/PbTe(21) SL sample measured with h= 4 gauss and zero external field at 0.1 Hz, 20 Hz and 1000 Hz. 132
6-4 Temperature dependence of χ_{in} for an EuTe(3)/PbTe(9) SL measured at three different AC fields) (a); the same data as in (a) but the data χ_{in} are normalized to the size of the AC field h= 1 gauss for the same EuTe(3)/PbTe(9) SL (b). 133

6-5 Normalized χ_{in} vs.T (closed circles) and χ_{out} vs. T (open circles) (a), and $\chi_{in}T^2$ vs. T (closed circles) and $\chi_{out}T^2$ vs. T (open circles) (b) for an EuTe(1)/PbTe(3) SL measured at a probing field of h=4 gauss and f=20 Hz. 134

6-6 Normalized χ_{in} vs. T (closed circles) and χ_{out} vs. T (open circles) for an EuTe(2)/PbTe(6) SL; the same set of data plotted as χT^2 vs. T including data for χ_{in} in the paramagnetic phase up to 40 K(b). . . . 135

6-7 Normalized χ_{in} vs. T (closed circles) and χ_{out} vs. T (open circles) for an EuTe(3)/PbTe(9) SL (a); the same set of data as in (a) plotted as χT^2 vs. T with data for χ_{in} up to 60 K in the paramagnetic phase included (b). The solid line in (b) represents the Curie-Weiss paramagnetic susceptibility. 136

6-8 (a) Normalized χ_{in} vs. T (closed circles) and χ_{out} vs. T (open circles) for an EuTe(4)/PbTe(12) SL; (b) same set of data as in (a) plotted as χT^2 vs. T with the data for χ_{in} in the paramagnetic phase up to 50 K included in (b). 137

6-9 (a) Normalized χ_{in} vs. T (closed circles) and χ_{out} vs. T (open circles) for an EuTe(5)/PbTe(15) SL; (b) the same set of data as in (a) is plotted as χT^2 vs. T with the data for $\chi_{in}(T)$ in the paramagnetic phase below 60 K included in (b). 138

6-10 (a) Normalized plot of χ_{in} vs. T (closed circles) and χ_{out} vs. T (open circles) for an EuTe(6)/PbTe(18) SL; (b) the same set of data as in (a) plotted as χT^2 vs. T, with the data for $\chi_{in}(T)$ in the paramagnetic phase up to 30 Kincluded in (b). 139

6-11 (a) Normalized plot of χ_{in} vs. T (closed circles) and χ_{out} vs. T (open circles) for an EuTe(7)/PbTe(21) SL; (b) the same set of data as in (a) plotted as χT^2 vs. T, with the data for χ_{in} in the paramagnetic phase below 30 K included in (b). 140

6-12 The temperature window above T_c defined by T_s - T_c where T_s is the temperature below which anisotropy in the susceptibility is first observed (a); the same set of T_s - T_c data plotted vs. $1/\xi$ (b). 141

6-13 Values of χ_{in} (closed circles) and χ_{out} (open) circles extrapolated to $T = 0$ K versus ξ, the EuTe thickness per SL period. The dotted line represents the value of the perpendicular component $\chi_{\perp}$ of the susceptibility at $T = 0$ K for a bulk EuTe sample. The χ_{out} value for the EuTe(6)/PbTe(18) is zero at 0 K which is not shown here because it would increase the range of the vertical scale. 142

6-14 The maximum value of χ_{in} vs. the EuTe layer thickness ξ. 143

6-15 The transition temperature T_c vs. the EuTe layer thickness ξ. 144

7-1 M vs. T for a 2D ferromagnet on a triangular lattice size of 100×100, with n=6000 Monte Carlo scans. The vertical line marks the temperature where the transition temperature T_c (=3.6 K) is determined from this simulation. 168

7-2 Root-mean-square magnetization versus temperature from Monte Carlo calculations for two lattice sizes of a two-dimensional square arrays of spins with periodic boundary conditions. The lattice sizes for our simulations are (upper panel) 50×50 and 16×16. Similar results were reported earlier by Watson et. al. in Ref.69 using periodic boundary conditions with lattice sizes of 225 spins and 2025 spins (lower panel). The dashed lines indicate the M_{rms} behavior for isolated two-dimensional arrays, i.e., without periodic boundary conditions. . . . 169

7-3 Normalized $M_{rms}(T)$ vs. T for an EuTe(3)/PbTe(9) SL of dimensions 30x30x3 (a), an EuTe(5)/PbTe(15) SL of dimensions 30x30x5 (b), and an EuTe(7)/PbTe(21) SL of dimensions 30x30x7 (c). For all simulations, at each temperature, 500 Monte Carlo scans were used for equilibriation and 2000 Monte Carlo scans were used for sampling. In these plots, $M_{rms}(T)$ is normalized to M_{total} (see text). Notice that with the above conditions, the computed error bars are so small that they are hardly readable from the graph. 170

7-4 M_{rms}/M_{total} vs. T for an EuTe(4)/PbTe(12) SL of dimensions 30x30x4 (a), and an EuTe(6)/PbTe(18) SL of dimensions 30x30x6 (b). All simulations took 500 Monte Carlo scans for equilibriation and 2000 Monte Carlo scans for sampling at each temperature. 171

7-5 $\chi_{\|}(T)$ vs. T for an EuTe(3)/PbTe(9) SL of dimensions 30x30x3 (a), an EuTe(5)/PbTe(15) SL of dimensions 30x30x5 (b), and an EuTe(7)/PbTe(21) SL of dimensions 30x30x7 (c). All simulations took 500 Monte Carlo scans for equilibriation and 2000 Monte Carlo scans for sampling at each temperature. 172

7-6 $\chi_{\|}(T)T^2$ vs. T for an EuTe(3)/PbTe(9) SL of dimensions 30x30x3 (a), an EuTe(5)/PbTe(15) SL of dimensions 30x30x5 (b), and an EuTe(7)/PbTe(21) SL of dimensions 30x30x7 (c). The straight-line like behavior for T greater than the temperature of teh divergence of $\chi_{\|}(T)$ suggests Curie-Weiss paramagnetic behavior. 173

7-7 $\chi_{\|}(T)$ vs. T for an EuTe(4)/PbTe(12) SL of dimensions 30x30x4 (a), an EuTe(6)/PbTe(18) SL of dimensions 30x30x6 (b). Each of these two simulations uses 500 Monte Carlo scans for equilibriation, and 2000 Monte Carlo scans for sampling at each temperature. 174

7-8 $\chi_{\|}(T)T^2$ vs. T for an EuTe(4)/PbTe(12) SL of dimensions 30x30x4 (a), and an EuTe(6)/PbTe(18) SL of dimensions 30x30x6 (b), in accordance with Fig.7-7. 175

7-9 $\chi_{\|}(T)$ vs. T for an EuTe(4.86)/PbTe(12) SL of dimensions 60x60x4.86 (see text). 176

7-10 Calculated $M_{rms}(T)$ vs. T using a Monte Carlo Ising simulation for an EuTe(4)/PbTe(12) SL of dimensions 30x30x4 (a), and an EuTe(6)/PbTe(18) SL of dimensions 30x30x6 (b) in a 4 gauss external field (see text). . . 177

7-11 χ_{in} (closed circles) and χ_{out} (open circles) vs. T for an EuTe(3)/PbTe(9) SL (a). Large error bars in χ_{in} reflect the instability of the χ_{in} calculations at low tempertures. A zoomed-in plot of χ_{in} (closed circles) and χ_{out} (open circles) vs. T for the same EuTe(3)/PbTe(9) SL (b). These results are obtained from a lattice of 13×13×3 spins using a Heisenberg model with dipolar forces. At each temperature, 2000 Monte Carlo steps are used for equilibriation and 2000 Monte Carlo steps for sampling. 178

7-12 Simulated specific heat C vs. T for the same Heisenberg model calculation for the EuTe(3)/PbTe(9) SL as is shown in Fig. 7-11. The temperature at which C diverges can be identified as the transition temperature T_c. 179

7-13 Experimental χ_{in} (closed circles) and χ_{out} (open circles) vs. T for an EuTe(3)/PbTe(9) SL (a), compared with the simulated χ_{in} (closed circles) and χ_{out} (open circles) vs. T for an EuTe(3)/PbTe(9) SL (b) in the temperature region $T>T_c$. 180

7-14 Simulated χ_{rms} vs. T for an EuTe(3)/PbTe(9) SL based on a Heisenberg model. Notice that χ_{rms} peaks at about the same temperature as the specific heat C diverges (see Fig.7-12). The χ_{rms} simulation is obtained from a lattice of 13×13×3 spins using the Heisenberg model with dipolar forces. At each temperture, 2000 Monte Carlo steps for equilibration, and 2000 Monte Carlo steps are used for sampling. . . . 181

7-15 Geometry of the $M_{\perp}$ and $M_{\|}$ components of the magnetization in relation to M_x, and M_y, and the average angle θ. 182

7-16 Magnetization direction vs. the number of Monte Carlo scans for an EuTe(3)/PbTe(9) SL at 1.3 K (a), 1.9 K (b), 2.5 K (c), 3.2 K (d), and 3.8 K (e). 183

7-17 Specific Heat C vs. T for an EuTe(3)/PbTe(9) SL using the Clock model. We use the peak in C to determine the transition temperature T_c as 3.4 K. 184

7-18 Monte Carlo simulation of $\chi_\perp$ vs. T for an EuTe(3)/PbTe(9) SL using the Clock model with 6-fold symmetry. 185

7-19 Monte Carlo simulations of $\chi_\parallel$ (open circles) and χ_{rms} (closed circles) vs. T for an EuTe(3)/PbTe(9) SL using the Clock model with 6-fold symmetry. 186

7-20 Values of the exchange couplings J_1 and J_2 for various europium chalcogenides as a function of the lattice constant.[50] 187

List of Tables

2.1 SLs parameters obtained from the best fits of x-ray diffractograms . . 45

3.1 Average SL period thicknesses L obtained from neutron diffraction spectra and the best fits of x-ray diffractograms, including also the values of the diffraction linewidths expressed as the Full Width at Half Maximum (FWHM) intensity for the central magnetic peak of each SL and the corresponding coherence length. 70

4.1 Magnetic susceptibilities for bulk BaF_2 and PbTe 103

4.2 Magnetic transition temperatures for SLs obtained from ZFC and FC $M(T)$ measurements 104

5.1 Experimental slopes of $M(H)$ for EuTe(ξ)/PbTe(η) SLs for various values of ξ 117

6.1 Magnetic transition temperatures T_c for SLs obtained from the peak position of χ_{in} (first row $T_{c,\chi}$), compared to the $T_{c,M}$ values previously determined from ZFC and FC measurements of $M(T)$ (second row). T_s values, the temperatures below which anisotropy in the susceptibility is first observed are given in the third row. 145

Chapter 1

Magnetism in Reduced Dimensions

1.1 Introduction

Magnetism has always been a thrust area of research in solid state physics. Magnetism in two-dimensions (2D) not only exhibits rich critical phenomena, but also plays a very important role in other areas of solid state research.

A 2D magnetic system is defined to include any system that consists of parallel planes of spins very large in size and a small number of magnetic planes. Thus a 2D system need not necessarily be a single atomic monolayer of spins.[1]

Broadly speaking, there are two general categories for 2D magnetic systems. The first category, exemplified by the Ising model, is characterized by an axial anisotropic magnetic exchange interaction. Secondly, the XY and Heisenberg models both are characterized by *isotropic* magnetic exchange interactions in two and three spatial directions, respectively. All three models can be represented by the general Hamiltonian

$$\mathcal{H} = 2\sum_{i<j} J_{ij}\vec{S}_i \cdot \vec{S}_j - 2\sum_{i<j}(J_A)_{ij}\vec{S}_i^z \cdot \vec{S}_j^z \tag{1.1}$$

where J_{ij}=0 for the Ising model, $(J_A)_{ij}$=J_{ij} for the XY model, and $(J_A)_{ij}$=0 for the Heisenberg model.

Complete solution for the 2D Ising model was first obtained by Onsager,[2] and

this model is known to have a phase transition at $T_c > 0$ K, where the T_c is identified by a spontaneous magnetization and a divergent susceptibility.[2] In contrast, both the XY and Heisenberg models in 2D do not have a spontaneous magnetization at any temperature above zero Kelvin.[3, 4, 5] However, the 2D XY model does have a divergent susceptibility at $T < T_{KT}$ (Kosterlitz-Thouless transition temperature), which marks the formation of bound magnetic vortices.

Although much of the above-mentioned theoretical work was carried out between 1944 and 1976, there has been a persistent difficulty in finding experimental systems that exactly fit the descriptions of the various 2D theoretical models. For this thesis, we focus our discussion on 2D Heisenberg antiferromagnets.

Starting with the most extensively-studied 2D Heisenberg antiferromagnet K_2NiF_4 (Ref.[6]), along with other less known compounds described in Ref.[7], are layered compounds with weak magnetic couplings along the direction perpendicular to the layers. Most of these compounds also have a very small amount of magnetic anisotropy. These two deviations, namely interlayer coupling (10^{-6} compared to the exchange coupling within the layer) and anisotropy (10^{-3} compared to the exchange coupling within the layer), are large enough to induce 3D magnetic ordering at temperatures above zero Kelvin.

The above-mentioned deviations are almost non-existent in EuTe/PbTe superlattices (SLs) as explained further in this thesis. Thus we propose to study the EuTe/PbTe SL as an ideal 2D Heisenberg antiferromagnet. Although Mermin and Wagner have shown rigorously that a 2D Heisenberg system will not have long range order[5], S. V. Maleev has shown analytically that long range order in a 2D Heisenberg system can be stabilized by a dipolar interaction.[8] Both of these theoretical studies are key to our experimental studies of EuTe/PbTe SLs.

Finally, we take note of two research areas that are closely related to the topic of this thesis. Firstly, at present, there is a considerable interest in 2D Heisenberg antiferromagnets due to their possible relevance to the mechanism of high temperature superconductivity. This connection was suggested by P. W. Anderson,[9] in part because the new class of high temperature superconductors (see Ref.[10]) all

have a copper-oxygen plane within the unit cell, and an antiferromagnetic spin arrangement on a square lattice, as a common structural feature. A review by T. Barnes summarizes the role of the 2D Heisenberg antiferromagnet in high temperature superconductivity.[11] Secondly, metallic magnetic SLs have received much experimental and theoretical attention recently, because of the giant magnetoresistance and oscillating magnetic inter-layer couplings observed in these SLs.[12, 13]

1.2 The EuTe Hamiltonian

EuTe has a spherically symmetric $^8S_{7/2}$ ground state and has no magnetic anisotropy reported from the antiferromagnetic resonance studies.[14] Thus EuTe is considered as an ideal Heisenberg magnet described by the Hamiltonian

$$\mathcal{H} = -J_1 \sum_{nn} \vec{S}_i \cdot \vec{S}_j - J_2 \sum_{nnn} \vec{S}_i \cdot \vec{S}_j \tag{1.2}$$

where nn and nnn denote the nearest and next-nearest-neighbor spin pairs, and J_1 and J_2 are exchange couplings.

The numerical values of J_1 and J_2 have been computed from the experimental Curie-Weiss temperature θ and the magnetic phase transition temperature of bulk EuTe by P. Wachter.[15] The nearest- neighbor exchange coupling J_1/k_B is ferromagnetic and is approximately 0.04±0.01 K, where k_B is the Boltzmann constant. The next-nearest-neighbor exchange coupling J_2/k_B is antiferromagnetic and is approximately 0.15±0.01 K. Note that the absolute value of J_2 between two next-nearest Eu atoms is larger than that of J_1 which couples two nearest-neighbor Eu atoms. The differences in both magnitude and sign between J_1 and J_2 are consequences of different exchange mechanisms. For the ferromagnetic J_1 coupling, a 4f electron is transferred to a 5d t_{2g} state of a nearest-neighbor Eu ion, which then polarizes the 4f spin through the f-d exchange mechanism (see Fig.1-1 for the electronic structure of EuTe). For the antiferromagnetic J_2 coupling, a p electron from a Te ion is transferred to the 5d e_g bands of a nearest-neighbor Eu ion and polarizes the $4f^7$ spins by means

of a f-d exchange. The exchange interaction can be very strong since the overlap between the p and d states is not small (see Fig.1-1). The exchange mechanism of J_2 that involves the virtual electron transfer between two Eu ions via an intermediate Te ion is the so-called true superexchange, and the exchange interaction is always antiferromagnetic.[16]

1.3 Heisenberg Antiferromagnetic EuTe/PbTe SLs

Short-period EuTe/PbTe SLs refer to the structure of several atomic monolayers (MLs) of EuTe separated by non-magnetic PbTe to form a single SL period. In the SL samples used in this thesis, the number of PbTe layers in one period was three times the number of EuTe layers so that the strains at each interface would be the same. The presence of straining is essential in maintaining 2D layer by layer growth of EuTe on PbTe as we shall see in Chapter 2. We will show in this thesis that EuTe remains antiferromagnetic and shows no detectable magnetic exchange anisotropy, even when the SLs are made with only two EuTe MLs per SL period. Thus we have given the thesis title "Magnetic Properties of EuTe/PbTe Heisenberg Antiferromagnetic Superlattices".

In the present EuTe/PbTe SLs, because of the nature of the short-range exchange interaction in EuTe and the absence of free electrons in PbTe ($10^{17}/\text{cm}^3$), the coupling between the EuTe block in one SL period to the adjacent EuTe block in the next SL period is limited to the dipole-dipole interaction. However, in order to maintain epitaxial growth, the PbTe layer thickness is always selected to be 3 times that of the EuTe layer thickness in a single SL period. Thus the inter-period separations (L) tend to be very large, and for those distances the dipole-dipole coupling (which depends inversely on L^3) becomes very small. Formally, the inter-period dipole-dipole coupling can be computed using the formalism developed in Ref. [8], and it is effectively zero in SLs.

The interest in the short-period EuTe/PbTe SLs arises from two attributes of these SL samples. First is the geometric attribute. The SLs are grown along the [111]

direction. Bulk EuTe in the magnetically ordered phase has ferromagnetically ordered (111) planes and the adjacent (111) planes are antiferromagnetically coupled. Thus we hope to observe different temperature dependences for the magnetization as we increase the EuTe thickness (which ranges from 1 to 7 layers in this study), especially with regard to SLs with even number of EuTe monolayers in contrast with odd number of EuTe monolayers. Second is the thickness attribute. In each SL period, the EuTe block consists of a few EuTe atomic MLs with macroscopic x-y dimensions. This by definition is a 2D magnetic system.[1] Specifically, with localized spins, isotropic exchange interactions and no inter-period coupling, EuTe/PbTe SLs are ideal 2D Heisenberg antiferromagnets.

All EuTe/PbTe SLs studied in this thesis have their [111] direction perpendicular to the SL planes. EuTe/PbTe SLs of the same orientation were studied by J. Heremans and D. L. Partin in 1988.[17] Specifically, temperature and magnetic field dependent magnetizations of three SLs, EuTe(1)/PbTe(3), EuTe(2)/PbTe(6) and EuTe(4)/PbTe(4) were reported in the temperature range $4<T<$ 200 K. A magnetic phase transition was reported for the EuTe(4)/PbTe(4) SL, but no magnetic phase transition was seen for the other two SLs. Recently, EuTe/PbTe SLs with the [100] direction perpendicular to the SL planes were studied by Kostyk *et al.* by $M(T,H)$ measurements.[18] Magnetic phase transitions were observed for an EuTe(4)/PbTe(30) SL and an EuTe(8)/PbTe(30) SL. The transition temperatures were used to infer information concerning EuTe/PbTe interfaces based on a mean-field model. We make further comments on their findings in relation to our present work in Chapter 4, where we discuss the magnetization measurements of our SLs. However, the two above-mentioned reports did not provide either x-ray or TEM characterization dat regarding structural information for their SL samples.

1.4 Thesis Outline

This thesis consists eight chapters.

Chapter 1 serves as an introduction to the thesis. Chapter 2 presents details

about the sample structure, including sample characterization by the TEM, STM and x-ray diffraction techniques. In Chapter 3, results from neutron diffraction measurements are summarized and are used to show the spin arrangements in our SL samples for $T<T_c$. Chapter 4 surveys the temperature dependent magnetization properties for our SLs, and the interpretation of the magnetization measurements is directly tied to the x-ray measurements in Chapter 2 and the neutron diffraction measurements in Chapter 3. In Chapter 5, results are presented on the field dependent magnetization for our SLs in the field range from 0 to 10 tesla; the results are found to be less sensitive to the x-ray measurements, but are relevant to some of the neutron diffraction measurements carried out in an external magnetic field. In Chapter 6, AC susceptibility measurements provides valuable information on the magnetic long-range order in SLs. Key features of the susceptibility data are the anisotropic susceptibility behavior immediately above T_c and extending to below the transition temperature, and the anomalous peak observed in the in-plane susceptibility. A comprehensive Monte Carlo study is presented in Chapter 7 to explain the above-mentioned features of the susceptibility based on various models for idealized magnetic systems. The approach taken in this thesis toward describing the magnetic properties of EuTe/PbTe SLs is illustrated in Fig.1-2. Chapter 8 includes an overall summary of the research results of the thesis and a commentary on research areas opened up by this thesis and further research remaining to be investigated. At the end of each chapter, a brief summary is given to outline the key results of that chapter.

1.5 Special Notation

The experimental plots presented in this thesis were made by *xvgr*, a Unix graphics program. This program uses so-called scientific notation. That is the program denotes 1×10^{-1} by 1e-01, so that the symbol e used to label our plots is not to be interpreted as the base of a natural log.

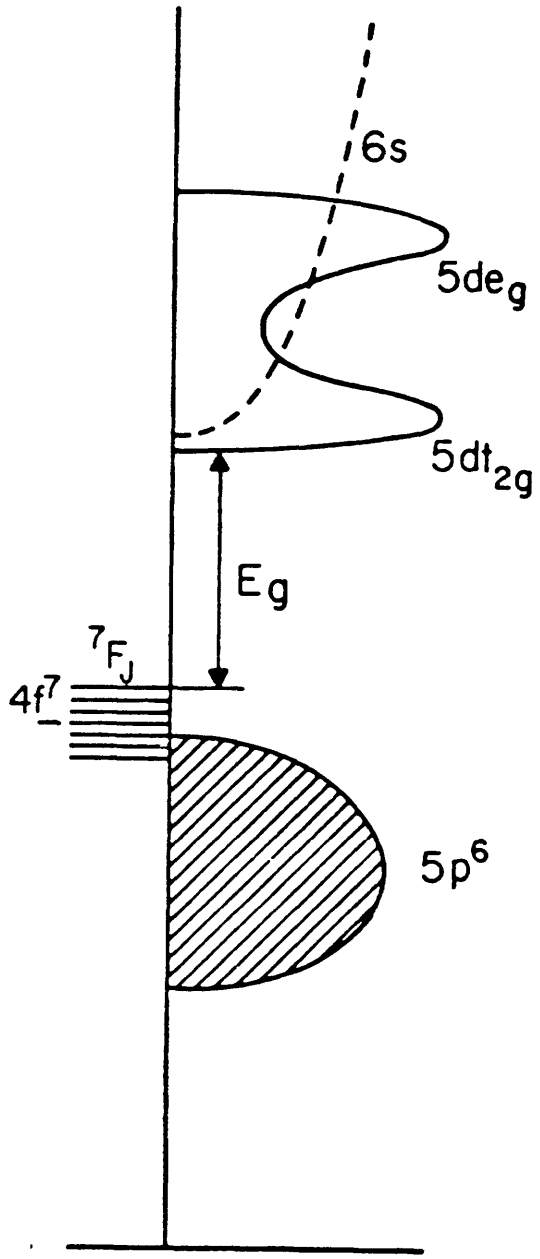

Figure 1-1: Electronic structure of EuTe, reproduced from Ref.[15]

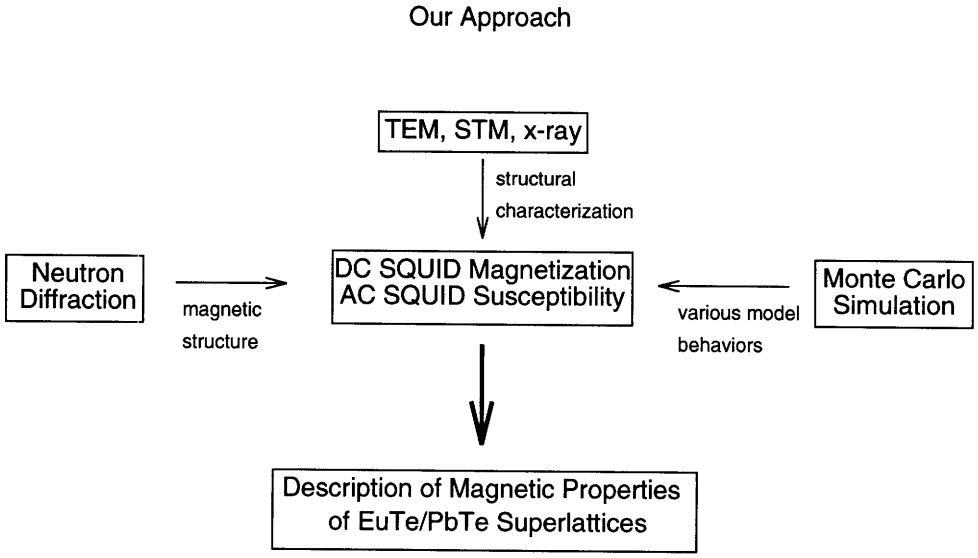

Figure 1-2: Experimental and computational methods employed in our magnetic studies of EuTe/PbTe superlattices.

Chapter 2

Chemical Structure of EuTe/PbTe Superlattices

2.1 Introduction

In this chapter, we will briefly review the Molecular Beam Epitaxial (MBE) growth process of EuTe/PbTe SLs, followed by a review of the chemical structure of these superlattices. As is well known in the field of nanostructure fabrication, MBE technology is capable of yielding layered structures of the highest quality, but it also is the most costly method to fabricate artificially layered structures. However, even the highest quality EuTe/PbTe SLs prepared by MBE are not perfect. Therefore, we will also review various structural characterization measurements performed on EuTe/PbTe SLs to provide essential background information for the subsequent chapters which report on magnetic studies. The structural characterization tools mentioned in this chapter include: Scanning Tunneling Microscopy (STM), Transmission Electron Microscopy (TEM), and x-ray diffraction. The samples studied by TEM and x-ray diffraction are the same samples that were used for the magnetic measurements, while the samples used for STM imaging are not. Nevertheless, the results of the STM characterization studies provide important information which is used for interpreting the magnetic measurements on the EuTe/PbTe SLs.

2.2 MBE Growth of EuTe/PbTe Superlattices

MBE growth of EuTe/PbTe SLs was first attempted by D. Partin at the GM Research Laboratory.[19] Since then, considerable improvement in the technique for growing these SLs has been made by Dr. G. Springholz, who worked on the MBE growth of EuTe/PbTe SLs in the group led by Professor G. Bauer, a group that is experienced in lead salt compounds,[20, 21] at the Johannes Kepler University, Linz, Austria. This section describes the MBE growth process developed by Dr. G. Springholz.[22]

For the samples used in this study, molecular beam epitaxy growth of PbTe and EuTe on BaF_2 (111) substrates was carried out in a Riber MBE growth chamber by Dr. G. Springholz. The absolute beam flux rates from the effusion cells were measured with a quartz crystal thickness monitor, and the substrate temperature was calibrated using Te_2 condensation points. For EuTe growth, separate beam flux sources for Eu and Te were used. Because of the high Te vapor pressure at the MBE substrate temperatures ($\sim$250°C), excess Te has to be supplied during EuTe growth, and therefore the growth is controlled by the Eu flux impinging on the surface, whereas all the excess Te re-evaporates from the surface.[23] In contrast, since PbTe sublimes in the form of PbTe molecules, it is directly evaporated from a PbTe effusion cell. Since the PbTe molecules adsorbed on the layer surface remain bound in a molecular state until incorporation in the crystal lattice,[24] MBE growth of PbTe is similar to MBE growth of elemental semiconductors, whereas EuTe MBE growth is comparable to that for III-V semiconductors by MBE techniques.

Depending on the substrate temperature and the Te_2 to Eu beam flux ratio, a Te- or Eu-stabilized EuTe growth mode exists, characterized by a different surface reconstruction, depending on the stabilization mode. However, due to the 2.1% lattice mismatch between EuTe and PbTe, 2D layer-by-layer heteroepitaxial growth of EuTe on PbTe (111) exists only in a very narrow regime of growth conditions. This is a result of the fact that in thermodynamic equilibrium, the preferred surface configuration of a fully-strained EuTe overlayer on PbTe (111) is not an ideal 2D layer, but rather that of a strongly corrugated layer, consisting of 3D islands of EuTe on a thin

wetting layer. In such a case, a significant part of the strain energy can be reduced by a lateral elastic deformation of the coherent 3D islands.[25] However, this effect can be suppressed when the mobility of the surface adatoms is drastically reduced during growth, so that the surface diffusion length is smaller than the critical wavelength for strain-induced islanding.[26] Thus for low substrate temperatures and high Te_2-to-Eu beam flux ratios, 2D layer-by-layer growth can be maintained as shown by the appearance of pronounced RHEED (reflection high energy electron diffraction) intensity oscillations.[23, 27]

2.3 In-situ STM

In-situ STM (scanning tunneling microscopy) measurements provide us with a direct image of an EuTe epilayer on PbTe. The scope of the STM image is usually about several μm^2, which is sufficiently large to give global information on the epilayer surface morphology. The surface of PbTe on BaF_2 is atomically flat on a length scale of more than 2000 Å and exhibits only large growth spirals with monolayer (ML) high step edges around the core of threading dislocations originating from the lattice-mismatched growth on the BaF_2 substrates. As shown in Fig.2-1,[27] the EuTe surface is much more corrugated on a length scale of about 200 Å with small monolayer high islands nucleated on the surface and ragged step edges (see Fig.2-2). This is a consequence of the much shorter surface diffusion lengths involved in EuTe MBE growth under such conditions.

Straight monolayer high step lines (see Fig. 2-3) suddenly appear on the surface parallel to the $\langle \bar{1}10 \rangle$ and $\langle \bar{2}11 \rangle$ crystallographic directions when the EuTe thickness exceeds 17 ML. The end points of these step lines can be identified as penetration points of threading dislocations, which apparently have moved by several μm parallel to the surface. As described by the classical model for strain relaxation by Matthews and Blakeslee,[28] this movement is induced by the strain in the layer, and results in the formation of a misfit dislocation segment at the interface, as illustrated in the inset in Fig.2-3. The appearance of these surface step lines indicates the onset

of strain relaxation, and thus the critical layer thickness can be detected with high precision.[29] The information on the critical layer thickness is particularly important to our magnetic studies, since we would like to avoid misfit dislocations at interfaces. All of the SLs that we have measured for magnetic properties have EuTe thicknesses smaller than the critical thickness (17 ML). Even the largest SL has only 7 EuTe MLs per SL period.

2.4 Ex-situ TEM

Transmission Electron Microscopy (TEM) investigations were performed on SLs after they are grown to provide a cross-sectional view perpendicular to the (111) plane. These measurements were carried out by Professor L. Salamanca-Riba at the University of Maryland on sister samples to those used in the magnetic measurements.[30] In two ways, these results complement the STM studies by N. Frank *et.al* described in Section 2.3. Firstly, TEM offers a side view of EuTe epilayers on PbTe. Secondly, TEM tells us the effects, if any, on the surface of EuTe (PbTe) after subsequent growth of PbTe (EuTe). The TEM images usually have a scope of 300 angstroms by 300 angstroms. The limited view is a disadvantage and this should be kept in mind when we look at TEM images, i.e., we can't simply extrapolate the smoothness of the interfaces shown in the TEM images to an arbitrarily large length scale.

The TEM results show smooth EuTe-PbTe interfaces on a length scale of about 200 angstroms (see Fig.2-4), in agreement with STM studies. Within the length scale of TEM images, we can't point out any systematic differences between PbTe on EuTe or EuTe on PbTe. Overall, the cross-sectional TEM images show that the real SLs have nearly the nominal SL configurations that we wanted. However, some TEM images show regions with a double periodicity, e.g., for the SL sample with a nominal thickness of 3.5 EuTe ML and 9 PbTe ML, there are regions where EuTe=7 ML and PbTe=17 ML(see Fig. 2-5). The cause of the double periodicity is not understood; however, its occurrence is rare and is combined with the fact that TEM probes a very small area, and only a few TEM images have shown this phenomena. We shall see

in the next section that x-ray diffraction also displays interference peaks due to SL periodicities that are twice as large as the nominal thickness; again these peaks are considerably broader and weaker when compared to those for SL samples showing x-ray peaks with the nominal periodicities. The increased linewidth and decreased intensity are consistent with smaller domains and less frequent occurrences of the regions with double periods.

2.5 X-ray Diffraction

Altogether, there are two series of SL samples that have been studied in this thesis. The first series, denoted as the 200 series, consists of samples for which ξ=2, 3, 4, 5, and 6 and with η=3ξ, where ξ and η, respectively, are the number of EuTe and PbTe layers per SL period. The second series, denoted as the 400 series consists of samples for which ξ=1, 2, 3, 4, 5, 6, and 7 and again with η=3ξ so that all SLs will have the same amount of strain. The x-ray results for the various samples are quite similar, and we will therefore only show some of the diffraction results here to illustrate the general structural characteristics of the SL samples studied in this thesis.

As shown in Fig. 2-6 the SL samples that have been studied in this thesis for their magnetic properties generally consisted of a 400 period EuTe(ξ)/PbTe(η) superlattice stack grown on a 3000 Å PbTe buffer layer. A 500 Å PbTe cap layer (Fig. 2-6) was used to prevent oxidation of the highly reactive EuTe. In each SL period (i.e., one SL cell), there are nominally ξ MLs (monolayers) of EuTe alternating with nominally $\eta = 3\xi$ monolayers of PbTe (constant EuTe/PbTe thickness ratio of 1/3), with ξ =1,...,7. There are more PbTe layers than EuTe layers in order to maintain the strained 2D layer by layer growth. As we have seen from the STM studies that without the straining, misfit dislocations will form at the EuTe-PbTe interfaces. Thus, given the importance of strain, it is remarkable that SLs with 400 periods can be prepared with few defects limited to the monolayer steps.

For the structural characterization, Dr. G. Springholz and Mr. C. Pichler have used a Philips MRD (materials research diffractometer) employing $CuK_{\alpha 1}$ radiation

and a four crystal Bartels monochromator (set for the Ge(220) reflection mode) in the primary beam. Triple axis (TA) optics were utilized for recording reciprocal space maps, using a channel-cut two-reflection Ge(220) analyzer crystal in the secondary beam. Here we focus our discussion on three SLs using their x-ray diffraction curves around the (222) Bragg reflection obtained by Dr. G. Springholz and Mr. C. Pichler (see Fig. 2-7). The x-ray scattering geometry is shown in Fig. 2-8. These spectra confirm that EuTe and PbTe grow in the fcc structure, with the (111) direction normal to the BaF_2 substrate for all SL samples. The dotted lines represent the simulations of the diffraction curves using dynamical diffraction theory carried out by Mr. C. Pichler. In all samples, the diffraction peaks of the BaF_2 substrate, the SL stack, the PbTe buffer, and the PbTe cap are identified. The peak splitting between the PbTe buffer and PbTe cap layer is due to differences in the strain state of these layers. Whereas the PbTe buffer layer is essentially fully relaxed, the thin PbTe cap layer experiences tensile strain associated with the SL strain relaxation. That is, the relaxed SL stack has a larger in-plane lattice constant than that of the PbTe buffer layer. Due to the additional SL periodicity along the [111] growth direction, several SL satellite peaks (labeled as SL0, SL$\pm$1, SL$\pm$2, and SL$\pm$3) appear on both sides of the 0^{th} order SL peak (SL0).

In order to obtain quantitative structural parameters of the SL samples, we have performed a complete strain analysis using reciprocal space mapping of the (222) and the (224) reflections. From this analysis, the in-plane lattice constant ($a_{\|}$, see Table 2.1) and the average normal lattice constant ($a_{\text{SL}\perp}$) of the SL stack were determined. In addition, we found that the tilt angle between the substrate and the epitaxial layers is less than 0.003°, i.e., it is negligible. Because the individual EuTe layer thicknesses in the superlattice stack are certainly below the critical layer thickness, it is clear that within the SL stack, the EuTe and the PbTe layers assume the same in-plane lattice constant, typical of short-period strain layer superlattices. Although initially for a very small number of periods, the EuTe/PbTe SL assumes the in-plane lattice constant of the PbTe buffer layer, as the number of periods increases, the SL stack starts to relax and the in-plane lattice constant increases. Because of

the very large number of periods in our samples, the SL stack has almost completely relaxed to its free-standing lattice constant, as is also indicated by the results of our strain analysis. However, the slight asymmetry of the SL peaks in the diffractograms shown in Fig. 2-7 indicates the presence of a residual strain gradient in the SL stack as a result of the strain relaxation process.

In order to determine the individual layer thicknesses in the SL stack, first we calculated the normal lattice constants $a_{\mathrm{EuTe}\perp}$ and $a_{\mathrm{PbTe}\perp}$ of the EuTe and the PbTe layers in the SL using the elastic constants and the previously determined SL in-plane lattice constant. The average normal lattice constant of the whole SL stack $a_{SL\perp}$ is then given by the geometrical average of the normal lattice constants of the individual layers, i.e.:

$$a_{\mathrm{SL}\perp} = \frac{d_{\mathrm{EuTe}} \times a_{\mathrm{EuTe}\perp} + d_{\mathrm{PbTe}} \times a_{\mathrm{PbTe}\perp}}{d_{\mathrm{EuTe}} + d_{\mathrm{PbTe}}} \tag{2.1}$$

where d_{EuTe} and d_{PbTe} are, respectively, the average EuTe and PbTe layer thicknesses in the SL.

Since $a_{\mathrm{SL}\perp}$ is known from the strain analysis, the EuTe/PbTe thickness ratio $d_{\mathrm{EuTe}}/d_{\mathrm{PbTe}}$ can be determined by Eq. (2.1), which together with the superlattice period obtained from the spacing of the SL satellite peaks yields the individual thicknesses of the EuTe and PbTe layers (see Table 2.1).

In fact, using the values of the strain parameters and the layer thicknesses derived above, the measured 2θ diffraction curves are well reproduced by the diffractograms calculated using dynamical diffraction theory (dashed lines in Fig. 2-7). However, there remain some notable discrepancies: (1) The SL satellite peak intensities are smaller than the calculated intensities. This is indicative of some interface disorder or the presence of interdiffusion at the hetero-interface. In fact, electron spin resonance (ESR) investigations on these samples gave evidence for the presence of isolated Eu ions in the PbTe region.[31] However, the well-resolved fine and hyperfine structures in the ESR spectra demonstrate that this interdiffusion is only very weak. (2) For all superlattice samples used in this thesis, weak additional diffraction peaks appear at

angular positions which correspond exactly to "half-order" superlattice satellite peaks. This indicates the presence of an additional double period structural modulation within the SL stack (see Fig. 2-7). In wide range x-ray rocking curves, these peaks are observed in between all regular SL satellite peaks, and they are perfectly reproducible for a large number of EuTe/PbTe SL samples with very different layer thickness. It is noted, however, that the intensity of these half-order peaks is much smaller than that of the regular SL satellites (see Fig. 2-7). In addition, the peak width is more than *four* times larger, which implies that the coherence length of the double period modulation is much smaller than the coherence length of the regular SL period ($\sim$ 4500 Å , derived from the FWHM=70 arcsec of the SL0 peak using Scherrer's equation.[32]) The x-ray observation of double period structural modulation agrees with the TEM image shown in Fig.2-5. Although the origin of the double modulation (half-order peaks) is not fully understood yet, its presence, as we shall see in the later chapters, has little effect on our magnetic studies.

In summary, the x-ray diffractograms show *multiple narrow* SLs peaks which indicate that the EuTe/PbTe SLs have high structural perfection and long range coherence. That is, the positions of the atomic planes (along the direction parallel to the (111) direction) are correlated ("coherent") from one SL period to another.[33] These x-ray results are in good agreement with STM and TEM studies.[29, 30]

2.6 Summary

2D layered growth of EuTe on PbTe (111) is achieved by MBE in EuTe/PbTe SLs over many (400) SL periods. In-situ STM images show that EuTe on PbTe (111) maintains layer-by-layer growth, free of misfit dislocations when the EuTe thickness ξ is less than 17 MLs. The EuTe/PbTe interfaces contain only single monolayer steps, with step widths of at least 200 Å.

The ex-situ TEM studies of cross-sectional images perpendicular to the (111) plane find that the interfaces in EuTe/PbTe SLs are smooth on the length scale of 200 Å, in agreement with STM results. Further, TEM images show little difference

between the top interface and the bottom interface in these SLs, i.e., whether PbTe grows on EuTe or EuTe grows on PbTe, there is little difference in interface quality. A few TEM images exhibit double periodicity with unknown origin.

X-ray diffraction offer quantitative global information on the SL structure, in contrast to the local properties probed by the TEM technique. The x-ray results show that, in general, EuTe/PbTe SLs have high structural perfection and long range coherence along the [111] growth direction.

In summary, the MBE-grown EuTe/PbTe SLs studied in this thesis have well-defined structures. This will enable us to conduct meaningful studies of their magnetic properties as a function of ξ, the number of magnetic EuTe monolayers within a SL period.

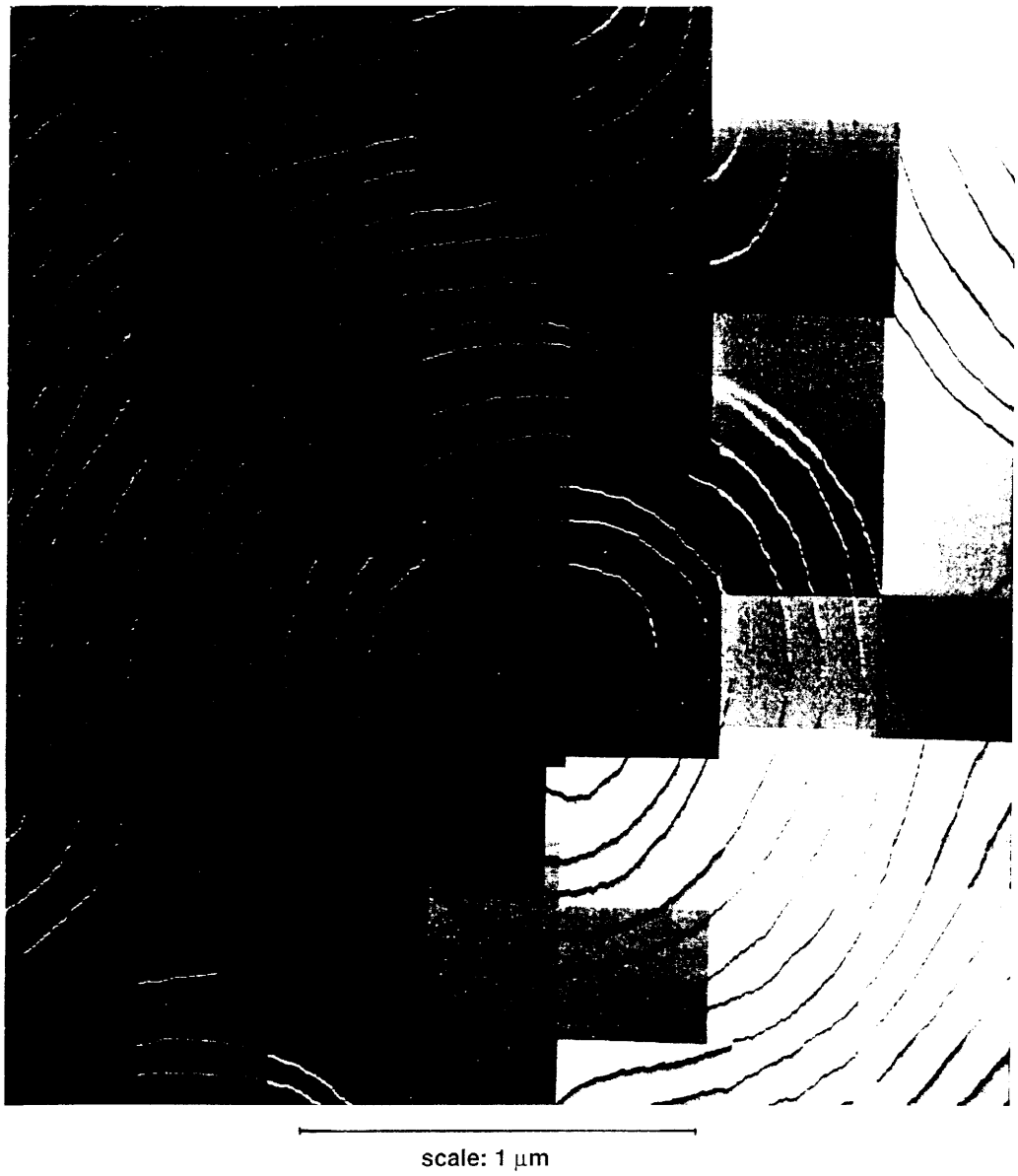

Figure 2-1: STM image of a PbTe epitaxial layer on BaF_2 (111) by G. Springholz, N. Frank, and G. Bauer.[25]

Figure 2-2: STM image of a 20 ML thick EuTe epitaxial layer on PbTe (111) by G. Springholz, N. Frank, and G. Bauer.[25]

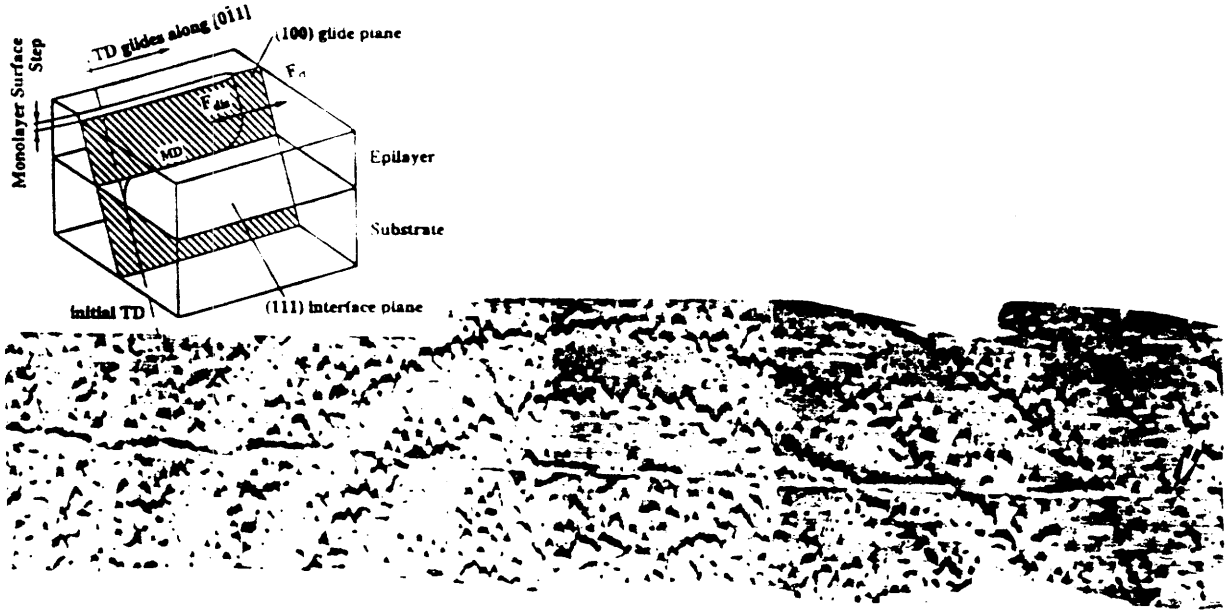

Figure 2-3: STM image ($2 \times 0.5\ \mu m^2$) of a 25 ML thick EuTe epitaxial layer on PbTe (111). The arrow indicates the end point of a threading dislocation. Inset: Schematic illustration of the strain relaxation process due to misfit dislocation formation by the glide of a pre-existing threading dislocation.[25]

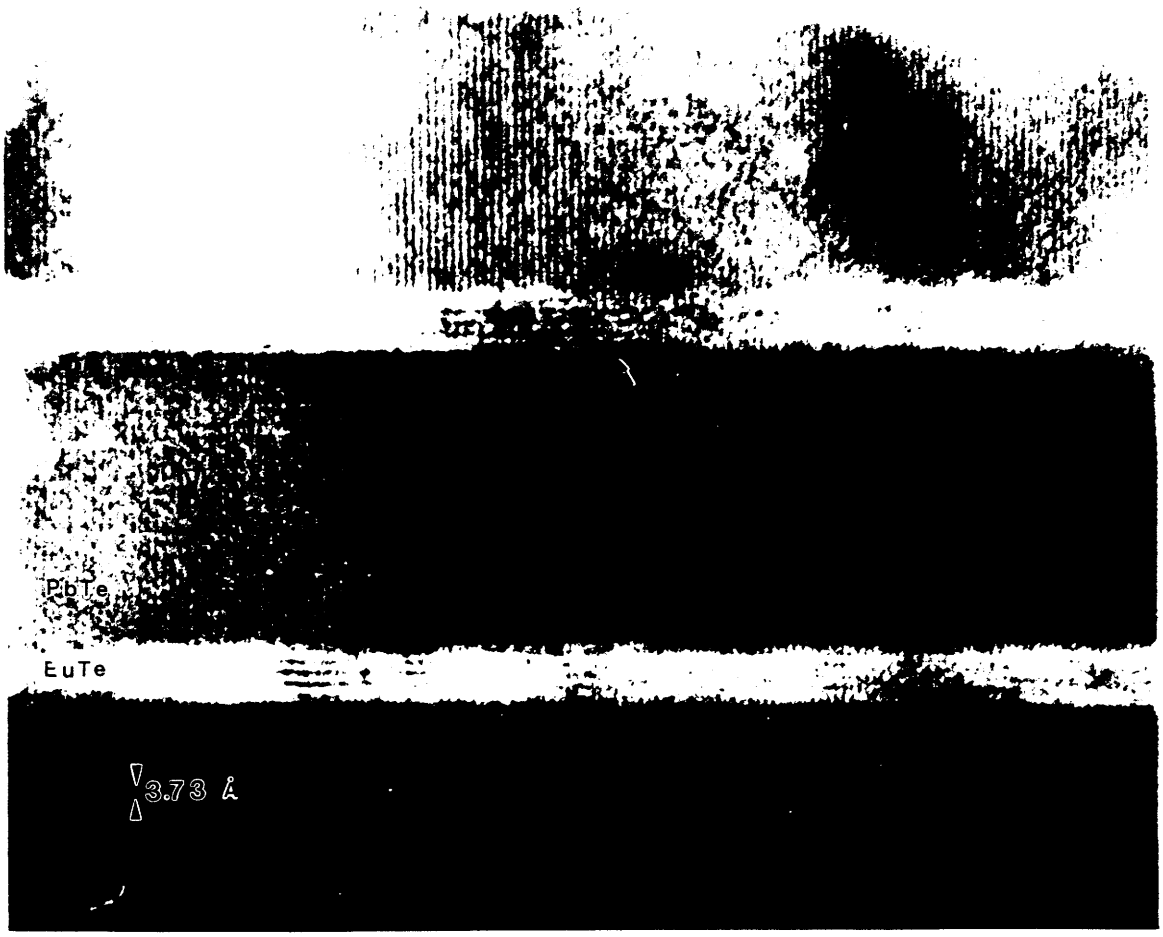

Figure 2-4: Cross sectional TEM image of a EuTe(5)/PbTe(22) superlattice sample by M. Shima and Lourdes Salamanca-Riba.[29]

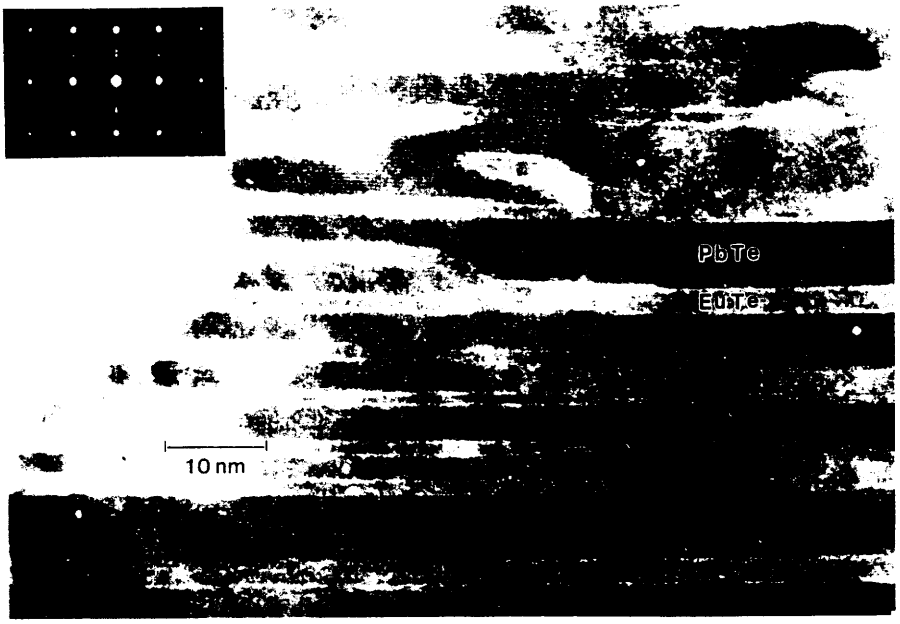

Figure 2-5: $(\bar{1}\bar{1}2)$ high resolution lattice image of the EuTe(3.5)/PbTe(9) superlattice. The upper left inset shows the electron diffraction pattern of the same SL sample by M. Shima and Lourdes Salamance-Riba.[29]

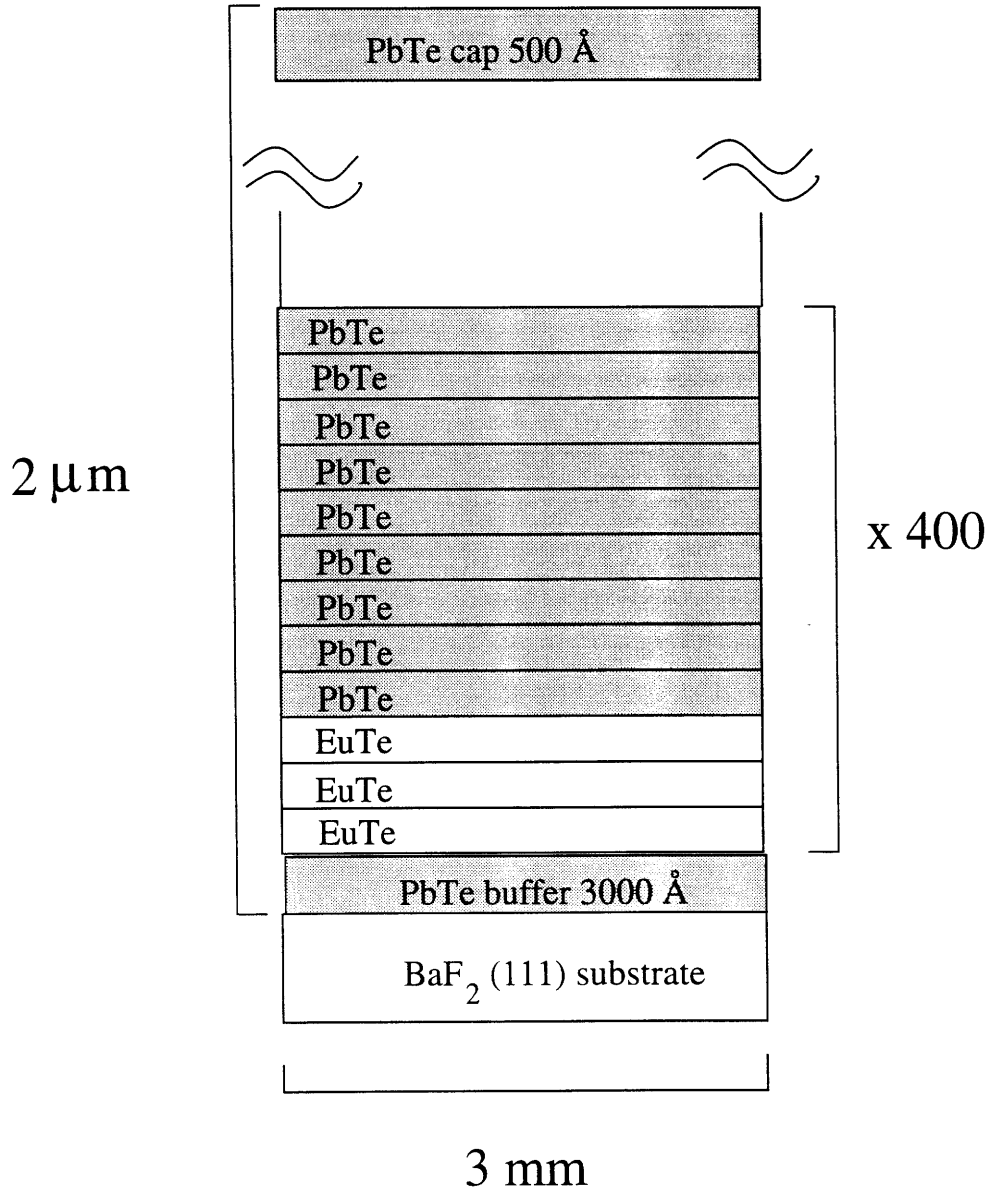

Figure 2-6: A schematic drawing of the cross sectional view of an EuTe(3)/PbTe(9) superlattice.

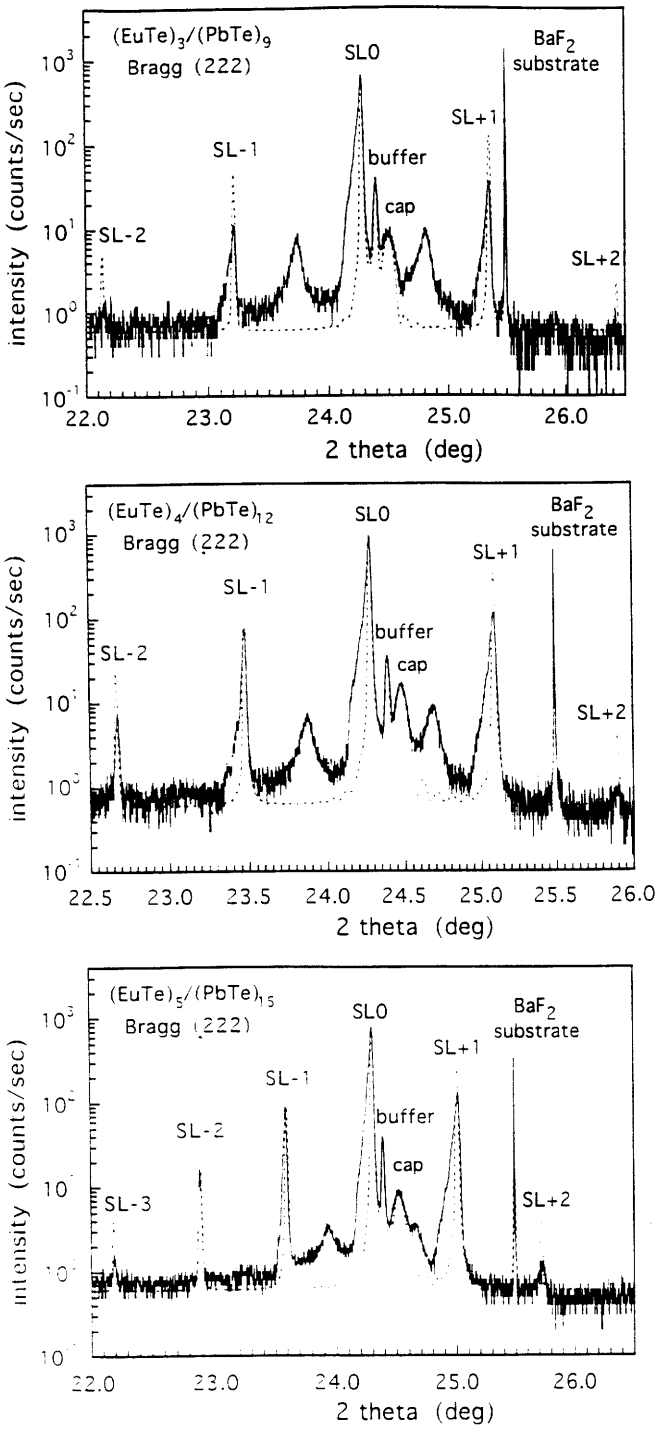

Figure 2-7: The (222) (Cu $K_{\alpha 1}$ radiation) Bragg x-ray diffraction patterns for the EuTe(3)/PbTe(9) (a), EuTe(4)/PbTe(12) (b), and EuTe(5)/PbTe(15) (c) superlattice structures (full lines). The dashed lines represent calculated diffractograms using the structural parameters obtained from the strain analysis. Both the x-ray data and their analysis were carried out by Dr. G. Springholz and Mr. C. Pichler.

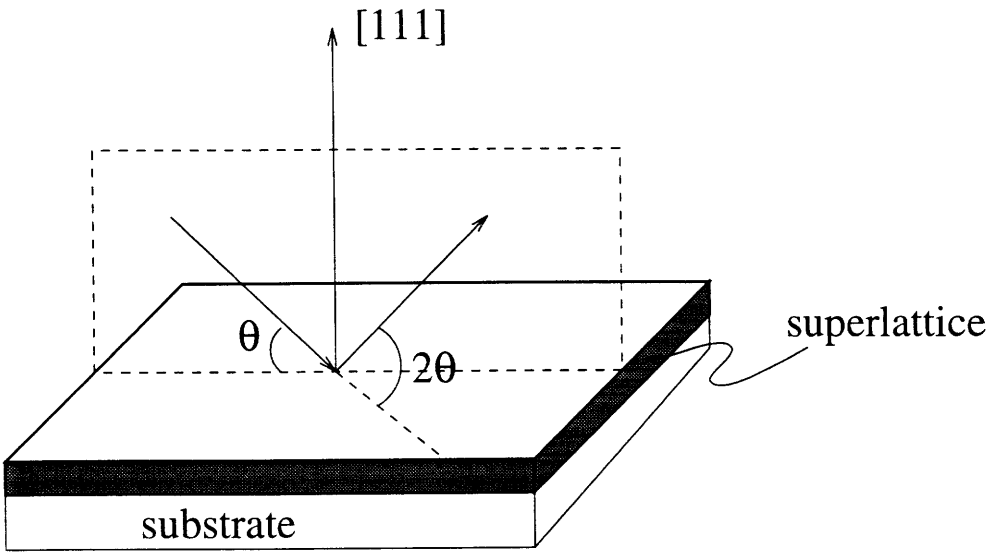

Figure 2-8: The scattering geometry used in the x-ray diffraction measurement. Both the scattering plane (SP) and the scattering vector ($\vec{Q}$) are normal to the sample surface, giving information about the atomic arrangements in the [111] direction.

Table 2.1: SLs parameters obtained from the best fits of x-ray diffractograms

nominal ξ/η	$a_{\parallel}$ (Å)	$a_{\mathrm{EuTe}\perp}$ (Å)	$a_{\mathrm{PbTe}\perp}$ (Å)	d_{EuTe} (ML)	d_{PbTe} (ML)	SL period (ML)
3/9	6.518±0.002	6.667±0.002	6.400±0.002	3.8±0.2	8.2±0.3	12.0±0.1
4/12	6.513±0.002	6.672±0.002	6.406±0.002	4.9±0.2	11.2±0.3	16.1±0.1
5/15	6.511±0.002	6.673±0.002	6.407±0.002	5.1±0.2	13.1±0.3	18.2±0.1

Chapter 3

Spin Structure of EuTe in Superlattices

3.1 Introduction

Magnetic neutron diffraction is the most direct method of identifying the magnetic structure of any material.[34] The spin arrangement of EuTe in the SLs is a key factor which determines the magnetic properties of these SLs. Although bulk EuTe has a type II antiferromagnetic spin arrangement in the magnetically ordered phase,[35] a priori we don't know if magnetic long range order will be stabilized in EuTe/PbTe SLs due to the small number of EuTe MLs per SL period, nor do we know what kind of spin arrangement will be stabilized if there is long range order. The neutron scattering experiments and results described in this Chapter represent the first of its kind for EuTe/PbTe SLs.

Following the success in determining the spin structures of other magnetic SLs by elastic neutron scattering,[36, 37] a comprehensive survey of the spin structure in EuTe/PbTe SLs was carried out by Drs. T. Giebultowicz and V. Nunez at the National Institute of Standards and Technology (NIST). I was invited to participate in several of the neutron scattering measurements at NIST.[38] Virtually all SLs studied in this thesis have their spin structures identified by elastic neutron scattering experiments.

Before presenting the spin structure of EuTe in our SLs, we will review the spin structure of bulk EuTe as a function of temperature and magnetic field. In zero field, EuTe makes a phase transition from the paramagnetic phase to the type-II antiferromagnetic phase at 9.8 K.[14] The type-II antiferromagnetic order is represented by ferromagnetic spin alignment within the (111) planes, the moments of adjacent planes being antiparallel (see Fig.3-1). For elastic neutron scattering experiments in bulk EuTe along the [111] direction, a magnetic diffraction peak will appear at the $(\frac{1}{2}, \frac{1}{2}, \frac{1}{2})$ position in reciprocal space for T<9.8 K, indicating that the magnetic unit cell is twice as large as the chemical unit cell along the [111] direction, consistent with the type II antiferromagnetic spin structure. For T<9.8 K, if an external magnetic field H is applied parallel to the (111) planes, the spins will first rotate in the (111) planes to a direction that is perpendicular to H, and then start to open up and project along the field direction. This is the so-called antiferromagnetic to canted antiferromagnetic transition. After this point, as H continues to increase, another magnetic diffraction peak will start to emerge at the (1,1,1) point in reciprocal space, at the same time that the intensity of the magnetic diffraction peak at the $(\frac{1}{2}, \frac{1}{2}, \frac{1}{2})$ point decreases. Eventually, under sufficiently high magnetic fields, all spins will be aligned parallel to the field, and the only magnetic diffraction peak will be at the (1,1,1) point in reciprocal space, implying that the magnetic unit cell is the same as the chemical unit cell along the [111] direction, i.e., the ferromagnetic spin structure is established. As we shall see in Section 3.4, elastic neutron scattering studies on our SLs, which are layered along the [111] direction, exhibit similar behavior, although the transition temperatures for the SLs are different from that of bulk EuTe and depend on ξ, the number of EuTe monolayers per SL period.

3.2 Triple-Axis Spectrometer

The standard neutron scattering facility includes a nuclear reactor and beam ports. The nuclear reactor at NIST has a circular shape, and nine neutron beam ports are uniformly distributed along the outer circumference of the reactor. The purpose of

the beam ports is to guide thermal neutrons generated by the nuclear fission reaction at the core of the reactor to experimental stations. At the end of each beam port, there is a spectrometer which selects a single wavelength neutron beam, guides it to the sample position and finally collects the diffracted neutron beam from the sample.

Our neutron diffraction studies on EuTe/PbTe SLs were performed at the 20 MW research reactor at NIST which has a (002) pyrolytic graphite (PG) monochromator and an analyzer fixed for elastic scattering, and a PG filter in the incident beam. Incident energies of 13.7 or 14.8 meV with 40 arc minute collimation throughout were used for most of the experiments. Data were taken using BT2 and BT9, two triple-axis spectrometers with similar signal-to-background ratios. The triple-axis refers to the axis for the monochromator, sample holder and detector (see Fig.3-2). For an elastic neutron diffraction experiment, the detector is tuned to the same wavelength as the incident neutron and the detector intercepts diffracted neutrons at an angle of 2θ with respect to the incident beam direction, where θ is the angle between the incident neutron beam and the normal to the plane of the SL.

3.3 Scattering Geometry

If EuTe in superlattices retains its bulk magnetic structure, antiferromagnetic diffraction peaks should appear near the $(\frac{1}{2}, \frac{1}{2}, \frac{1}{2})$ point along the [111] direction in reciprocal space, whereas the Bragg peaks due to the atomic structure should show near the (1,1,1) point. In other words, the $\uparrow\downarrow$ antiferromagnetic unit cell is twice as large as the chemical unit cell. Therefore neutron diffraction spectra taken below the transition temperature with momentum transfer vector $(\vec{Q})$ along any one of four [111] directions in the cubic structure should be suffice to identify the type-II antiferromagnetic spin structure. Of these, the [111] direction perpendicular to the SL plane is a special direction which will be explained in Section 3.5. The scattering geometry associated with elastic neutron scattering from this plane is shown in Fig. 3-3. The scattering plane (SP) is defined by the incident neutron beam and the scattered neutron beam. Both the scattering plane and the scattering vector $(\vec{Q})$ are normal to the sample

surface, so that scattering experiments with this geometry provide information on the spin ordering within the (111) planes and the spin arrangement along the [111] direction between the adjacent (111) planes.

The structure factor for neutron diffraction is sensitive to the angle between the magnetization direction and the momentum transfer direction. Specifically, the structure factor **F** is given by the expression,

$$\mathbf{F} = \sum_{r} \mathbf{q} p e^{i\vec{Q}\cdot\vec{r}} \tag{3.1}$$

where **q** is the magnetic interaction vector defined by

$$\mathbf{q} = \hat{Q}(\hat{Q} \cdot \hat{S}) - \hat{S}. \tag{3.2}$$

Here $\hat{S}$ and $\hat{Q}$ are unit vectors along the spin direction and the direction of momentum transfer, respectively. The factor p is the magnetic scattering length and has a magnitude on the order of the electron radius.[34] From the definition of **q**, the maximum scattering intensity occurs when the spin direction is perpendicular to the momentum transfer. The combination of the diffraction spectra and the formula for the structure factor **F**, enables us to determine the underlying spin structure.

3.4 Experimental Conditions

All diffraction spectra were obtained at fixed temperatures. In this survey, scattering data were obtained at temperatures of 4.2 K and 1.8 K. These temperatures were chosen, considering both the limited available beam time and what was known about the magnetic ordering temperature in the bulk, as well as in the SLs from magnetic measurements (see Chapters 4, 5 and 6). All SLs have magnetic phase transition temperatures above 8 K except for the SL with 2 MLs of EuTe in each SL period, which has a transition temperature below 4.2 K. The EuTe(1)/PbTe(3) SL was not measured by neutron diffraction in this study. However, as will be shown in Chapters 4 and 6, no phase transition is observed in the EuTe(1)/PbTe(3) SL down to 1.7 K,

the lowest temperature attainable with our magnetization and susceptibility equipment. The temperature of the sample during the neutron scattering experments was monitored and controlled by a Lake Shore Temperature Controller. The SL sample orientation with respect to the incident neutron beam is like that shown in Fig. 3-3. SL samples are usually greased onto a sample board (which is approximately 2 in. $\times$ 2 in.) and capped by a sheet of aluminum foil. The sample board is attached to the end of the sample probe, which in turn is lowered into the cryostat during the experiments.

About half of the neutron diffraction spectra were taken with an external magnetic field. In our field-dependent studies, we have covered a field range up to 6 tesla. The magnet we used for this purpose was a custom-made superconducting split coil magnet, with a capability of delivering a magnetic field of 7 tesla.

3.5 Experimental Results

3.5.1 Zero Field Diffraction Experiments

Adopting the scattering geometry shown in Fig. 3-3, we have done elastic neutron diffraction scans with the momentum transfer $\vec{Q}$ perpendicular to the SL plane, i.e., parallel to one of the four [111] directions in the cubic structure. Magnetic diffraction peaks were observed at the $(\frac{1}{2}, \frac{1}{2}, \frac{1}{2})$ AF reflection point (Q_z=0.84 Å^{-1}) for SLs with EuTe thicknesses per SL period larger and equal to 2 MLs, as discussed below.

For an EuTe(2)/PbTe(10) SL, Fig.3-4 shows a neutron diffraction scan near the $(\frac{1}{2}, \frac{1}{2}, \frac{1}{2})$ reflection point along the [111] direction at 4.2 K. The structure-less diffractogram implies that there is no antiferromagnetic order at this temperature in the EuTe(2)/PbTe(6) SL. However, as the temperature is lowered to 1.8 K, a single magnetic peak shows up at the $(\frac{1}{2}, \frac{1}{2}, \frac{1}{2})$ AF reflection point (see Fig.3-5), indicating that spins on each (111) plane of EuTe are ferromagnetically ordered, while the spins on adjacent (111) planes are aligned antiparallel.

Diffraction results showing magnetic peaks near the $(\frac{1}{2}, \frac{1}{2}, \frac{1}{2})$ AF reflection point

are also obtained for SLs with 3, 4, 5, and 6 MLs of EuTe per SL period (see Fig.3-6). The diffractogram for SL EuTe(6)/PbTe(18) is similar to that of the EuTe(2)/PbTe(10) SL, i.e., there is a single broad magnetic peak, with the maximum occuring at Q_z=0.84 Å^{-1}. Even for SLs (i.e., SL EuTe(3)/PbTe(9), SL EuTe(4)/PbTe(12), and SL EuTe(5)/PbTe(15)) which have multiple magnetic peaks, the central peak with the largest intensity is always located at Q_z=0.84 Å^{-1}, indicative of the type-II antiferromagnetic spin structure that is common to all the SL ordered phases in Fig.3-6.

For the EuTe(3)/PbTe(9), EuTe(4)/PbTe(12), and EuTe(5)/PbTe(15) SLs, multiple magnetic diffraction peaks are seen (labeled as SL0, SL±1, SL±2, and SL±3 see Fig.3-6) due to the SL periodicity along the [111] direction, resembling the x-ray data presented in Section 2.5. The distance (in Å^{-1}) between two adjacent peaks (Δ) is related to L (in Å), the thickness of a SL period, by the relationship $\Delta=2\pi/L$. Thus, as ξ increases from 3 to 5 in Fig.3-6, the spacing between the SL peaks becomes smaller, indicative of the larger SL period in real space. For example, for an EuTe(3)/PbTe(9) SL, we have a nominal thickness for a SL period L=(3+9)×3.75 Å= 45 Å, while the average SL period thickness obtained from the neutron diffraction data for the same SL is L = 44.2 Å. In Table 3.1, various values of Δ for SLs with ξ=3, 4, and 5 are summarized, and the corresponding values of L are calculated and compared to those determined from x-ray diffraction data. The agreement between the neutron diffraction and x-ray diffraction data on the average SL period thickness is very good.

Further, Dr. T Giebultowicz postulated that multiple SL magnetic peaks imply some kind of magnetic coupling between the magnetic layers of different SL periods. The value of the Full Width at Half Maximum (FWHM) linewidth for the central magnetic peak at Q_z=0.84 Å^{-1} is a good measure of the coherence length of this magnetic coupling. Specifically, the coherence length$\simeq 2\pi/FWHM$. The results for the FWHM linwidth and for $2\pi/FWHM$ are listed in Table 3.1. The coherence length is limited to about two SL period thicknesses for the ξ=3 SL, three SL period thicknesses for the ξ=4 SL, and one SL period thickness for the ξ=5 SL. The reason

for the EuTe(4)/PbTe(12) SL to have the longest magnetic coherence length among all SLs along the [111] direction is not yet understood. Dr. Giebultowicz's conjecture about inter-period magnetic coupling seems to be supported by the SL data, where the SLs with larger PbTe thicknesses do not show multiple SL magnetic peaks (see the diffractogram for the EuTe(6)/PbTe(18) SL in Fig.3-6). As another example, neutron scattering data for an EuTe(3)/PbTe(15) SL along the [111] direction perpendicular to the SL plane has a diffractogram with only a single peak near $(\frac{1}{2}, \frac{1}{2}, \frac{1}{2})$ AF reflection point (see Fig.3-7). On the other hand, the limited magnetic coherence length suggests that the inter-period magnetic coupling observed here could also be due to SL structural imperfections, such as the double periodicity seen in the x-ray diffraction scans and in the TEM images (see Fig. 2-7 and Fig.2-5). The SL cross-sectional TEM image Fig.2-5 shows a large SL period (twice as large as the nominal SL period), which suddenly bifurcates into two regular SL periods. Such a structure could well induce multiple magnetic diffraction peaks.

Finally, when we changed the momentum transfer direction to any one of the other three [111] directions, i.e., scanning along [111] directions that are not the one perpendicular to the SL plane, we did not observe any neutron diffraction peaks.[38] These results lead to the important conclusion that the SLs have a single (111) magnetic domain, in agreement with the magnetization studies to be presented in Chapter 4.

3.5.2 Field-Dependent Diffraction Experiments

Using the same scattering geometry as that of the zero field diffraction studies, neutron diffraction scans were again taken along the [111] direction perpendicular to the SL plane in the presence of an external magnetic field applied parallel to the SL plane.

Figure 3-8 shows the magnetic diffraction spectrum for an EuTe(4)/PbTe(12) SL at 4.2 K with H=6 tesla. The diffraction peaks are concentrated near the (111) reflection point, with the largest peak centered exactly at Q_z=1.68 Å^{-1}, consistent with ferromagnetic spin alignment. In Chapter 5 we will show that at 4.2 K and H=6 tesla, the EuTe(4)/PbTe(12) SL has just crossed the magnetic phase boundary

from the canted AF phase to the ferromagnetic phase with all the spins aligned in the field direction. There should be two more peaks for SL+1, and SL+2 on the right hand side of the largest diffraction peak at Q_z=1.68 Å^{-1}. However, no such peaks are seen because of the interference from the large signal of the BaF_2 substrate. Figure 3-9 shows the magnetic diffraction spectrum for an EuTe(5)/PbTe(15) SL at 4.2 K with H=5 tesla. Here magnetic diffraction peaks are seen near both the $(\frac{1}{2}, \frac{1}{2}, \frac{1}{2})$ reflection point and the (1,1,1) reflection point. Diffraction peaks near the $(\frac{1}{2}, \frac{1}{2}, \frac{1}{2})$ point are observed as expected at the above-mentioned temperature and field values, since the EuTe(5)/PbTe(15) SL is still expected to be in the canted AF phase under these temperature and magnetic field conditions (see Chapter 5). The values of Δ extracted from Fig.3-8 and Fig.3-9 are 0.106 Å^{-1} and 0.089 Å^{-1}, respectively. These values for Δ agree with those listed in Table 3.1.

As the external magnetic field increases from zero, EuTe will first transform from the antiferromagnetic state to a canted AF state, and eventually to a ferromagnetic state when the external field is larger than the antiferromagnetic exchange coupling J_2. In the ferromagnetic state not only are the spins on each (111) plane ferromagnetically ordered, but spins on adjacent (111) planes are also aligned in parallel. Thus, as the magnetic field is increased, we should see magnetic diffraction peaks at the $(\frac{1}{2}, \frac{1}{2}, \frac{1}{2})$ AF reflection point decrease in intensity, and simultaneously we expect to see new peaks emerge at the (1,1,1) ferromagnetic reflection point. Indeed, Fig.3-8 and Fig.3-9 show exactly the expected field-dependent diffraction behavior for an EuTe(4)/PbTe(12) SL and an EuTe(5)/PbTe(15) SL, respectively.

3.6 Computer Simulation

At MIT, we have developed a simple computer program to simulate qualitatively the neutron magnetic diffraction patterns for EuTe/PbTe SLs. This program explains the origin of the multiple magnetic diffraction peaks observed near the $(\frac{1}{2}, \frac{1}{2}, \frac{1}{2})$ point and the envelope function that defines the relative intensity of the various peaks. This program, however, cannot explain either the asymmetry observed in the diffraction

patterns or the widths of diffraction peaks. More elaborate programs developed at NIST have taken into account the corrections for neutron absorption and extinction, and for the neutron beam profile. Although the NIST programs produce better fits to the data, they, however, give little insights regarding the mechanism of the inter-period magnetic coupling suggested by the data.

In our simulations we assume AF inter-period coupling in zero field. For example, an EuTe(4)/PbTe(12) SL, the AF inter-period coupling implies a ↑↓↑↓ PbTe ↑↓↑↓ spin arrangement. This spin arrangement is called AF coupling because the spins on the last monolayer of one EuTe layer are aligned antiparallel to the spins on the first monolayer of next EuTe layer. In our simulations, we also assume ferromagnetic inter-period coupling in high fields. Again for an EuTe(4)/PbTe(12) SL, ferromagnetic inter-period coupling implies ↑↑↑↑ PbTe ↑↑↑↑) spin arrangement. Although we cannot offer any explanation for the AF inter-period coupling in zero field, we find through our simulations that if the inter-period coupling is like ↑↓↑↓ PbTe ↓↑↓↑ in zero field, then the overall diffraction pattern will be shifted, and the central maximum is no longer at the Q_z=0.84 Å^{-1} point in contrast to the experimental data where the central maximum of all diffraction spectra is always at the Q_z=0.84 Å^{-1} point.

We start the calculation of the diffraction pattern with a familiar result,

$$1 + cos(-\delta) + cos(-2\delta) + ...(toNterms) = \sum_{n=0}^{N} cos(-n\delta) = \frac{sin(N\delta/2)}{sin(\delta/2)}, \qquad (3.3)$$

derived in an undergraduate optics course for an N-slit diffraction pattern.[39] Neutron scattering from superlattices is like diffracting light from two superimposed diffraction gratings, each with a grating separation of d and L, respectively (see Fig.3-10), where d is the inter-atomic plane distance and L is the thickness of each SL period. Therefore the sum from the top to the bottom of the N SL periods, where each period of length L contains N_a magnetic layers, takes the form:

$$cos(-LQ) + cos(-LQ - dQ) + cos(-LQ - 2dQ) + ... + cos(-LQ - N_a dQ)$$
$$+cos(-2LQ) + cos(-2LQ - dQ) + cos(-2LQ - 2dQ) + ... + cos(-2LQ - N_a dQ)$$
$$+cos(-3LQ) + cos(-3LQ - dQ) + cos(-3LQ - 2dQ) + ... + cos(-3LQ - N_a dQ)$$
$$+... + cos(-NLQ) + cos(-NLQ - dQ) + cos(-NLQ - 2dQ) + ... + cos(-NLQ - N_a dQ)$$
$$= \frac{sin(NQL/2)}{sin(QL/2)} \frac{sin(N_a Qd/2)}{sin(Qd/2)},$$

which is identical to the results given in Ref.[40].

Figure 3-11 shows a simulated zero field diffraction pattern for an EuTe(4)/PbTe(12) SL (to be compared to Fig.3-6 showing the experimental diffraction scans). The diffraction peaks are centered around Q=0.84 Å^{-1} (which is the $(\frac{1}{2}, \frac{1}{2}, \frac{1}{2})$ AF reflection point), derived from $2\pi/2d$, where $2d$ indicates the size of the antiferromagnetic unit cell, which is twice as large as the chemical unit cell, and where d=3.75 Å is the inter-planar distance. In a high external magnetic field, the spins in the EuTe layer will be aligned in a ferromagnetic spin arrangement and the corresponding neutron diffraction patterns will have no peaks near $(\frac{1}{2}, \frac{1}{2}, \frac{1}{2})$, but will have peaks at the (1,1,1) reflection point (Q=1.67 Å^{-1}), consistent with a ferromagnetic spin arrangement (see Fig.3-12 and compare it to Fig.3-8). From the simulations, we come to two conclusions. Firstly, SL structures with an AF type-II spin arrangement give rise to multiple magnetic diffraction peaks near the $(\frac{1}{2}, \frac{1}{2}, \frac{1}{2})$ point in Q space. Specifically, the peak to peak separation (Δ) between the diffraction peaks is determined by the relation $\Delta=2\pi/L$, where L is the SL period thickness. In our simulations, the input value of L for the EuTe(4)/PbTe(12) SL was taken as L=60 Å, while the L determined from $2\pi/\Delta$ is 60.4 Å, in good agreement. Secondly, the envelope function that defines the relative intensity of different diffraction peaks is given by the thickness of the EuTe layer in each SL period.

3.7 Summary

The magnetic diffraction peaks observed in all SLs (i.e., ξ=2, 3, 4, 5, and 6) at the $(\frac{1}{2}, \frac{1}{2}, \frac{1}{2})$ position for $T<T_c$ and in zero magnetic field are consistent with the magnetic ordering of EuTe in SLs, consisting of ferromagnetically aligned (111) planes, and spins on the adjacent (111) planes which are antiferromagnetically oriented. This magnetic structure is the same as that of bulk EuTe. Further, out of the four distinct [111] directions in a cubic structure, spins in EuTe/PbTe SLs lie exclusively in a selected single (111) plane, namely the plane that is parallel to the SL plane (to minimize the dipole-dipole interaction energy as will be illustrated in Chapter 7). Moreover, the superlattice peaks at the $(\frac{1}{2}, \frac{1}{2}, \frac{1}{2})$ position, observed for some of the SLs, are consistent with a model assuming an AF inter-period coupling. However, the mechanism behind this coupling is poorly understood at present. We have excluded the possibility that the AF inter-period coupling can be stabilized by inter-period dipole interactions, because of the large intervening PbTe layer thickness between the two adjacent EuTe layers (see Section 7.7.2). The phenomenon of a large SL period (exactly twice as large as the nominal SL period), which suddenly bifurcates into two regular SL periods, as seen in the TEM images (see Fig. 2-5), could give rise to the AF inter-period coupling. On the other hand, this implied AF inter-period magnetic coupling does not play an essential role in the phase transitions observed in these SLs, because SLs without the implied inter-period magnetic coupling also show phase transitions from the paramagnetic phase to the type-II antiferromagnetic phase. Finally, our simple computer simulation demonstrates three qualitative features observed both in zero field and in field-dependent neutron diffraction experiments. They are: (1) the position of the central diffraction maximum is determined by the spin structure; the zero field neutron scattering results are consistent with the type-II antiferromagnetic structure and show a diffraction maximum at the $(\frac{1}{2}, \frac{1}{2}, \frac{1}{2})$ point in Q space, while the field-dependent neutron scattering results agree with the ferromagnetic spin structure and have a diffraction maximum at the (1,1,1) point in Q space; (2) the peak-to-peak separation (Δ) between the diffraction peaks is determined by the relation $\Delta=2\pi/L$,

where L is the SL period thickness; and (3) the envelope function that defines the relative intensity of different diffraction peaks is given by the thickness of the EuTe layer in each SL period.

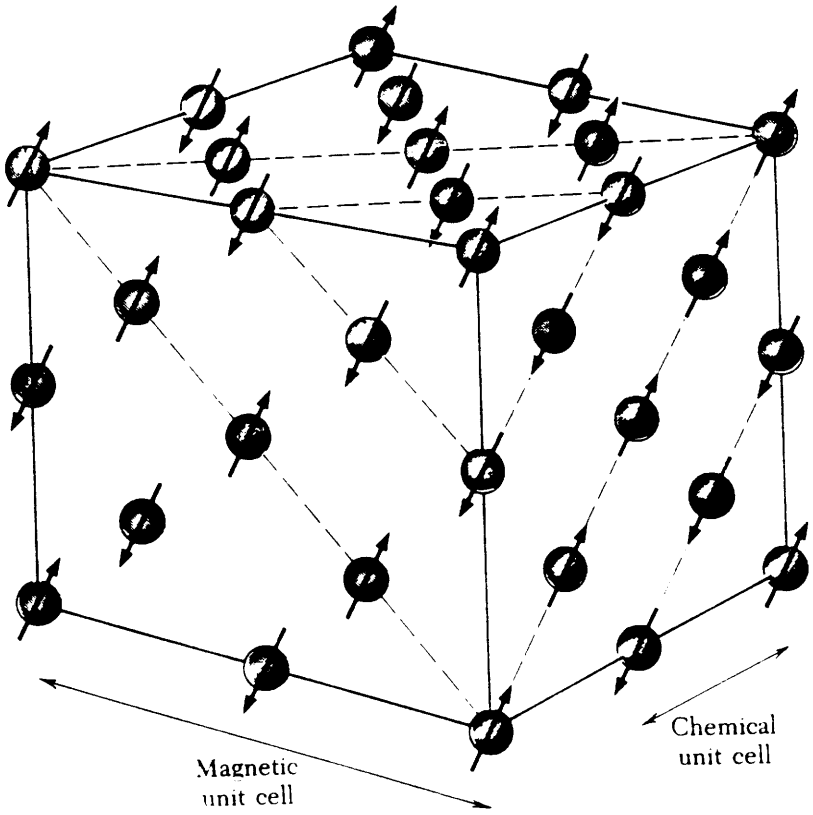

Figure 3-1: Spin arrangements of type II antiferromagnets.

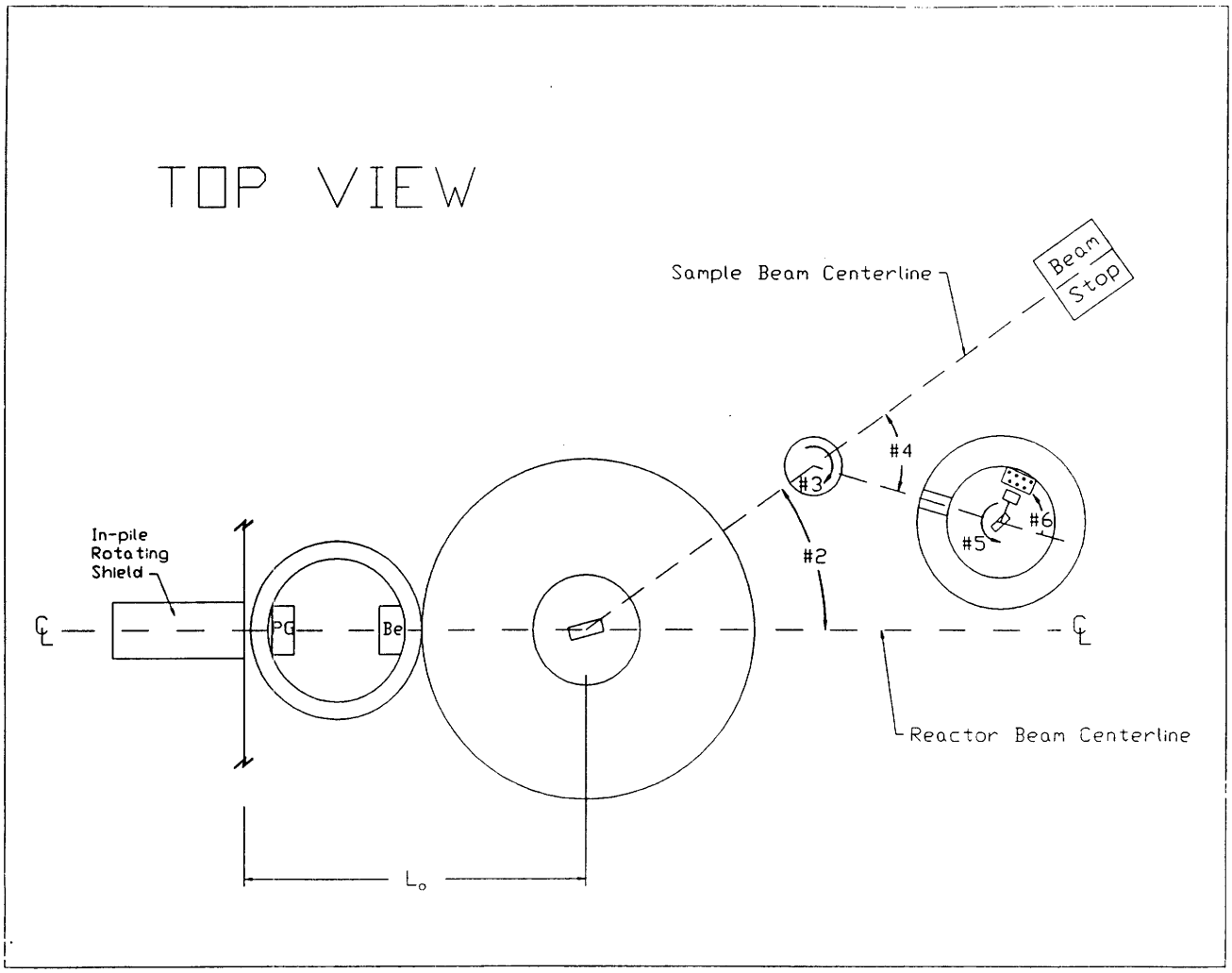

Figure 3-2: A schematic layout of a triple-axis spectrometer.

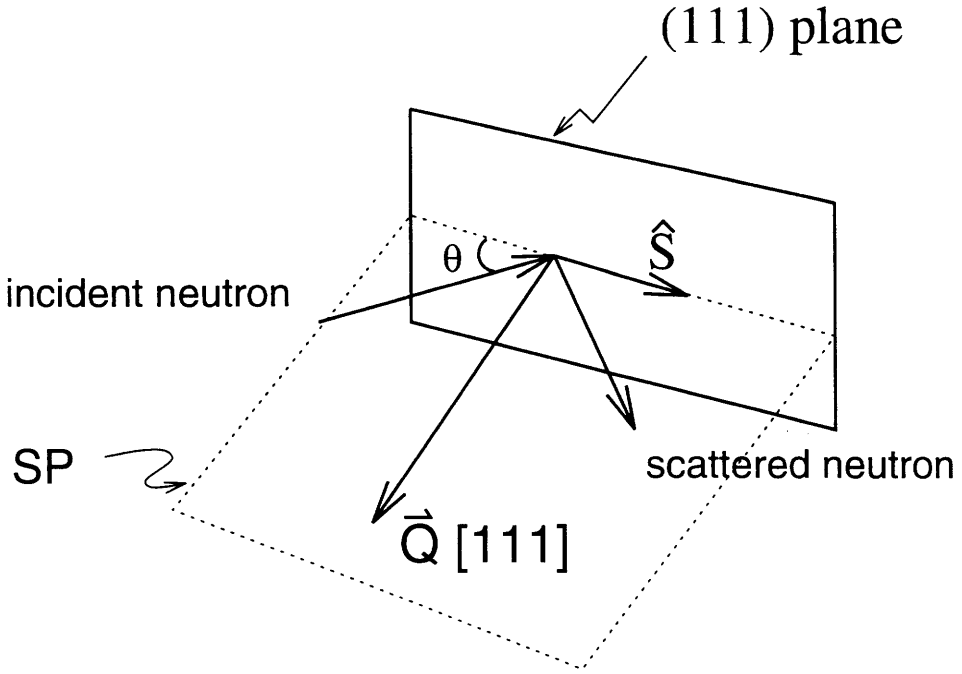

Figure 3-3: The scattering geometry used in the magnetic neutron diffraction experiments. Both the scattering plane (SP) and the scattering vector ($\vec{Q}$) are normal to the sample surface, so that scattering experiments with this geometry provide information on the spin ordering within the (111) plane spin arrangement along the 111 direction between adjacent (111) planes. The scattering plane is defined by the incident neutron and the scattered neutron beam directions.

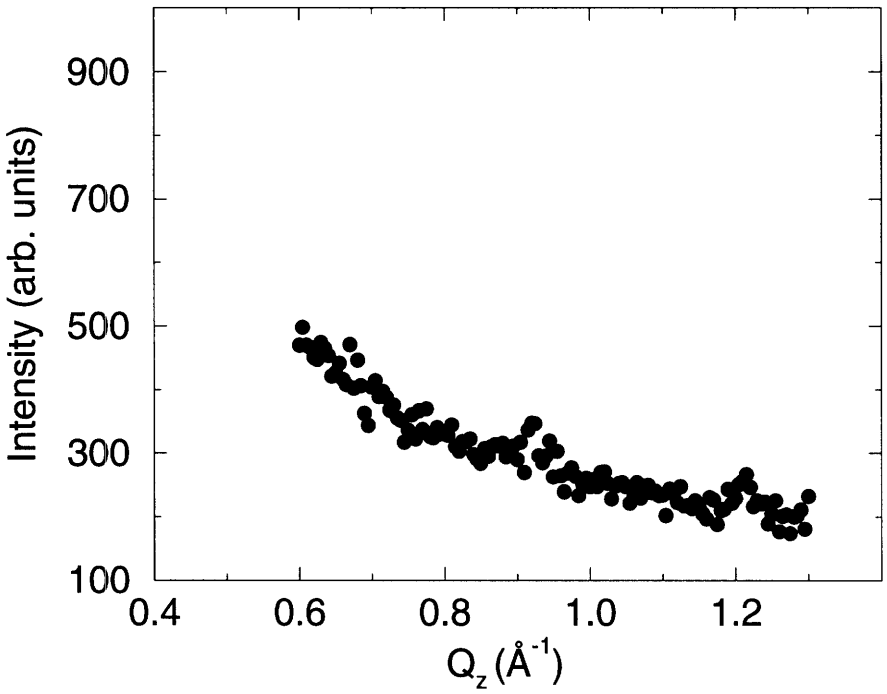

Figure 3-4: Diffraction scans at T=4.2 K for $\vec{Q}$ along the [111] direction through the position of the $(\frac{1}{2}, \frac{1}{2}, \frac{1}{2})$ AF reflection (Q_z=0.84 $Å^{-1}$) for an EuTe(2)/PbTe(6) SL.

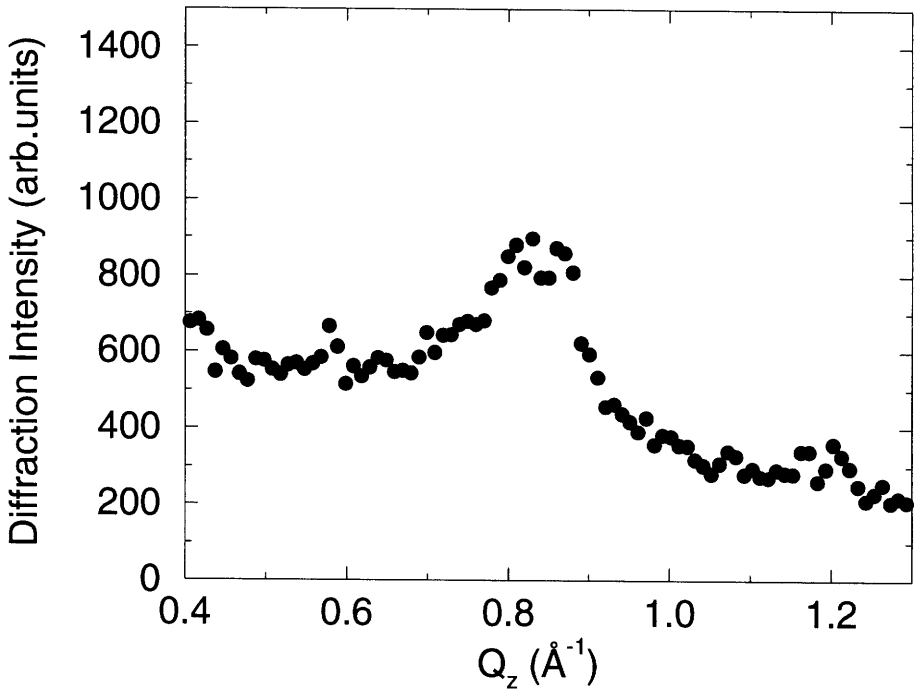

Figure 3-5: Diffraction scans at T=1.8 K along the [111] direction through the position of the $(\frac{1}{2}, \frac{1}{2}, \frac{1}{2})$ AF reflection (Q_z=0.84 $Å^{-1}$) for an EuTe(2)/PbTe(10) SL.

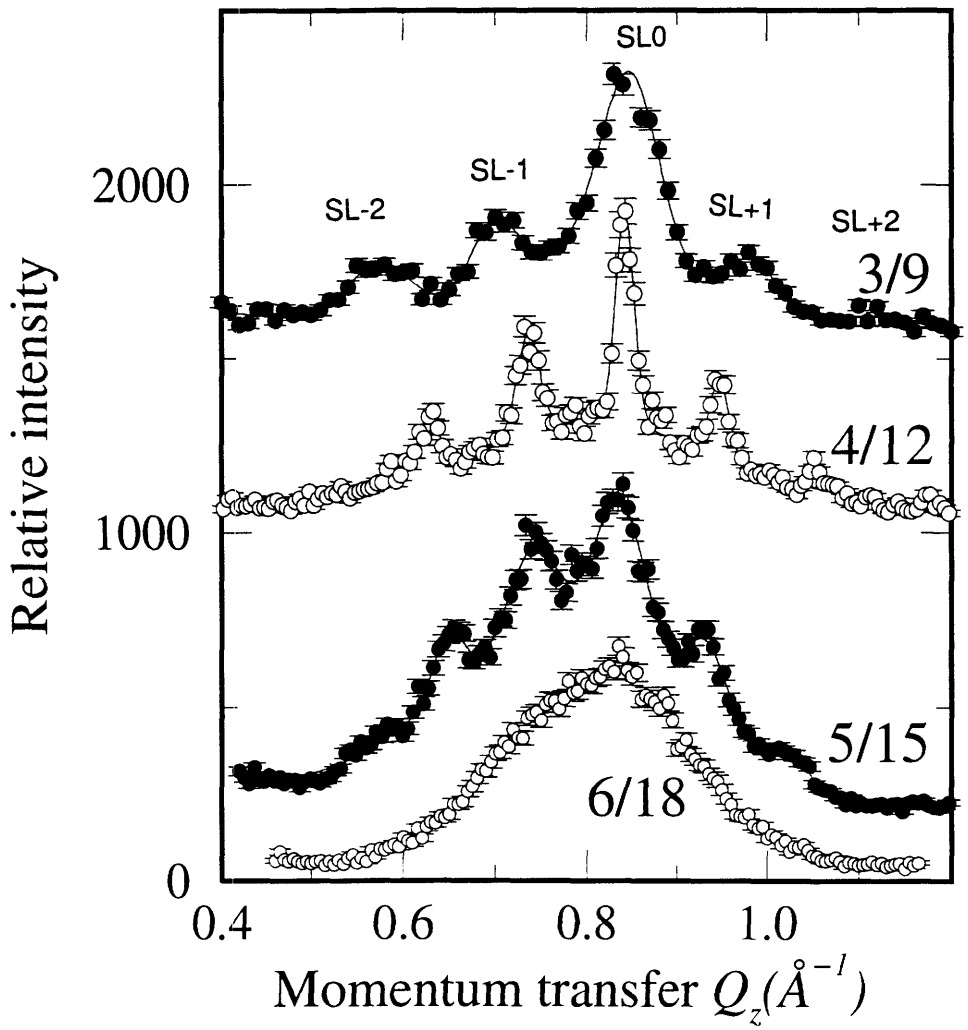

Figure 3-6: Diffraction scans at T=4.2 K along the [111] direction through the position of the $(\frac{1}{2}, \frac{1}{2}, \frac{1}{2})$ AF reflection (Q_z=0.84 $\AA^{-1}$) for EuTe(3)/PbTe(9), EuTe(4)/PbTe(12), EuTe(5)/PbTe(15), and EuTe(6)/PbTe(18) SLs.

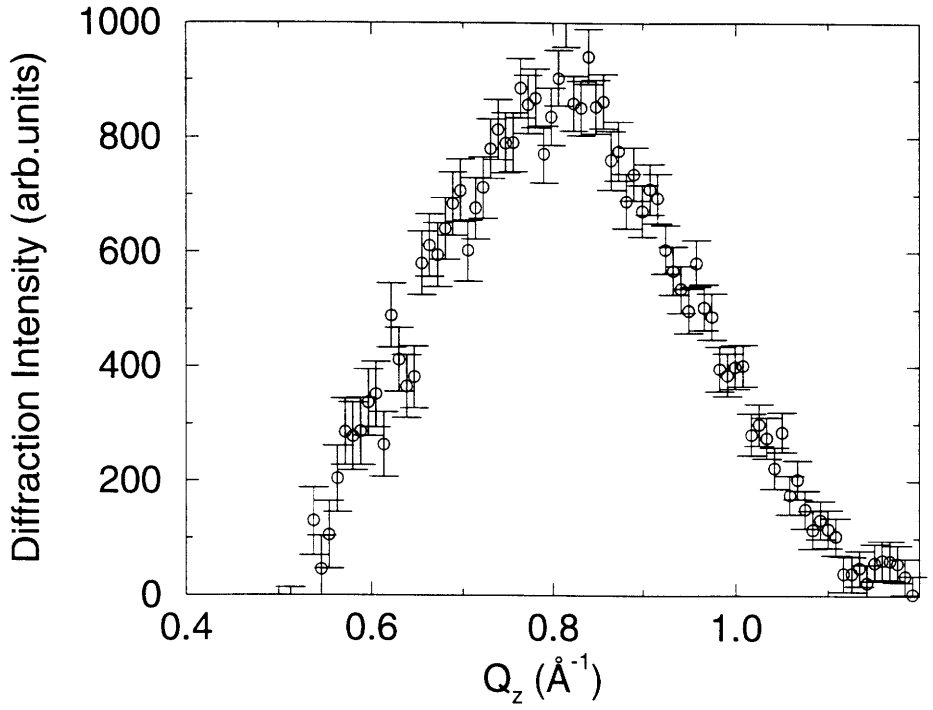

Figure 3-7: Diffraction scans at T=4.2 K along the [111] axis through the $(\frac{1}{2}, \frac{1}{2}, \frac{1}{2})$ AF reflection position for an EuTe(3)/PbTe(15) SL. The absence of the SL peaks implies absence of the inter-period magnetic coupling.

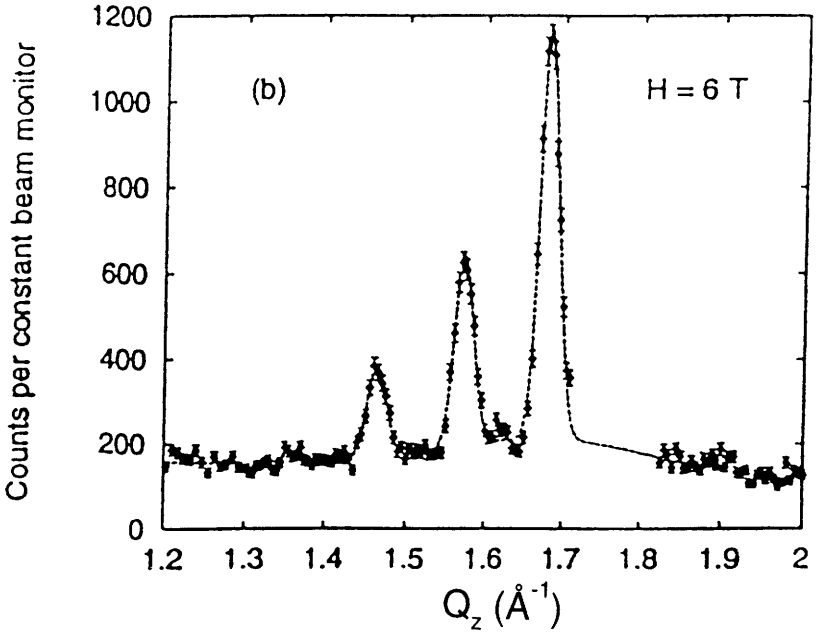

Figure 3-8: Diffraction scan at T=4.2 K along the [111] axis through the (1,1,1) FM reflection position at H=6 T for an EuTe(4)/PbTe(12) SL.

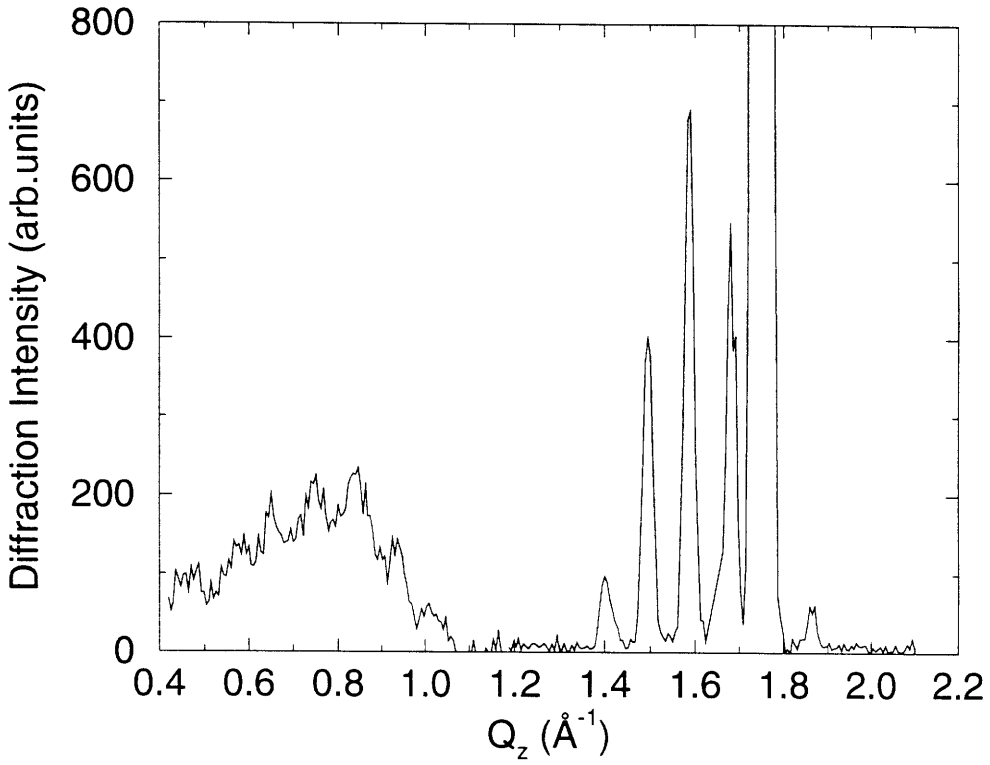

Figure 3-9: Diffraction scan at T=4.2 K along the [111] axis through both $(\frac{1}{2}, \frac{1}{2}, \frac{1}{2})$ reflection the (1,1,1) reflection positions at H=5 T for an EuTe(5)/PbTe(15) SL.

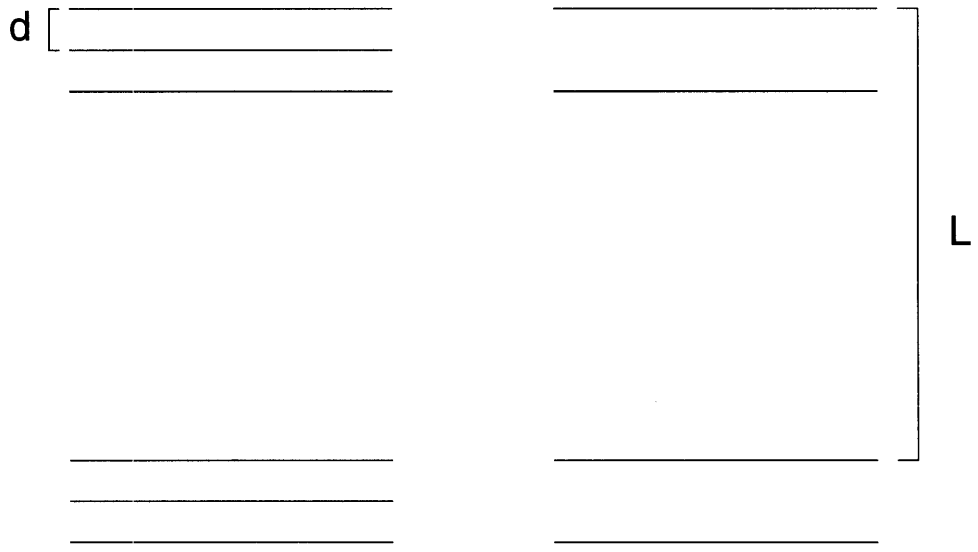

Figure 3-10: Neutron scattering from superlattices is like diffracting light from two superimposed diffraction gratings, each with grating separations of d and L, respectively.

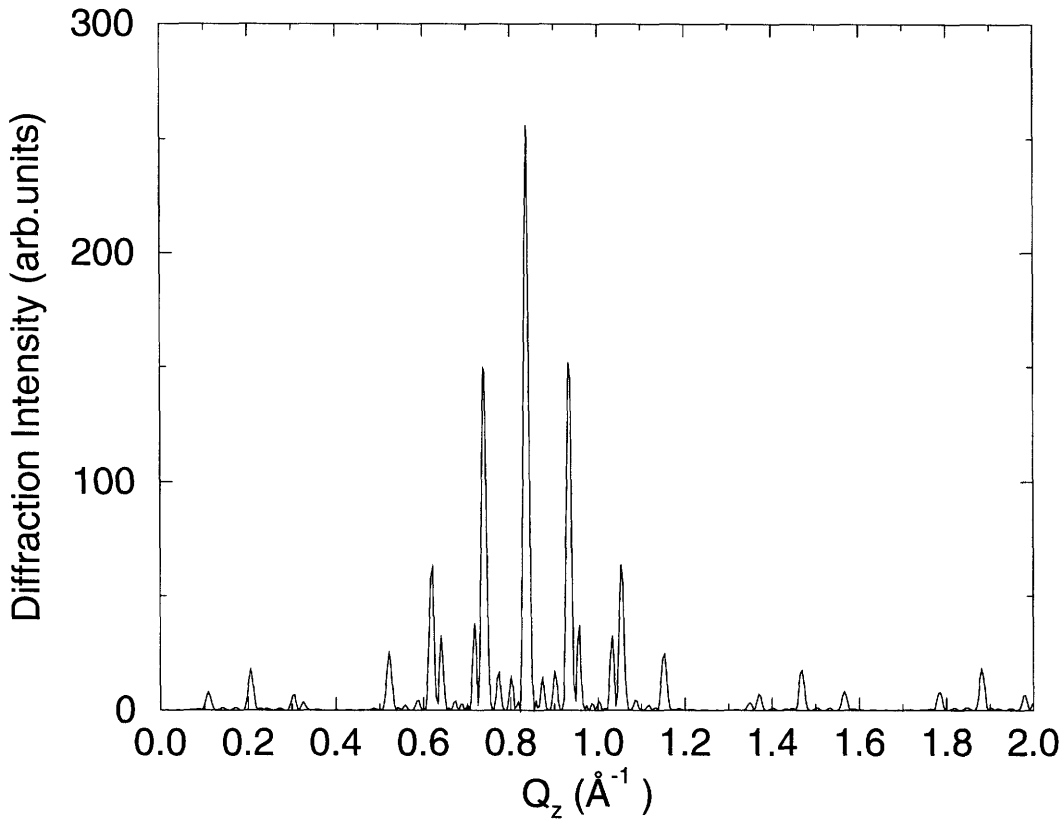

Figure 3-11: A simulated zero field diffraction scan for T< T_c along the [111] axis through the $(\frac{1}{2}, \frac{1}{2}, \frac{1}{2})$ AF reflection point for an EuTe(4)/PbTe(12) SL.

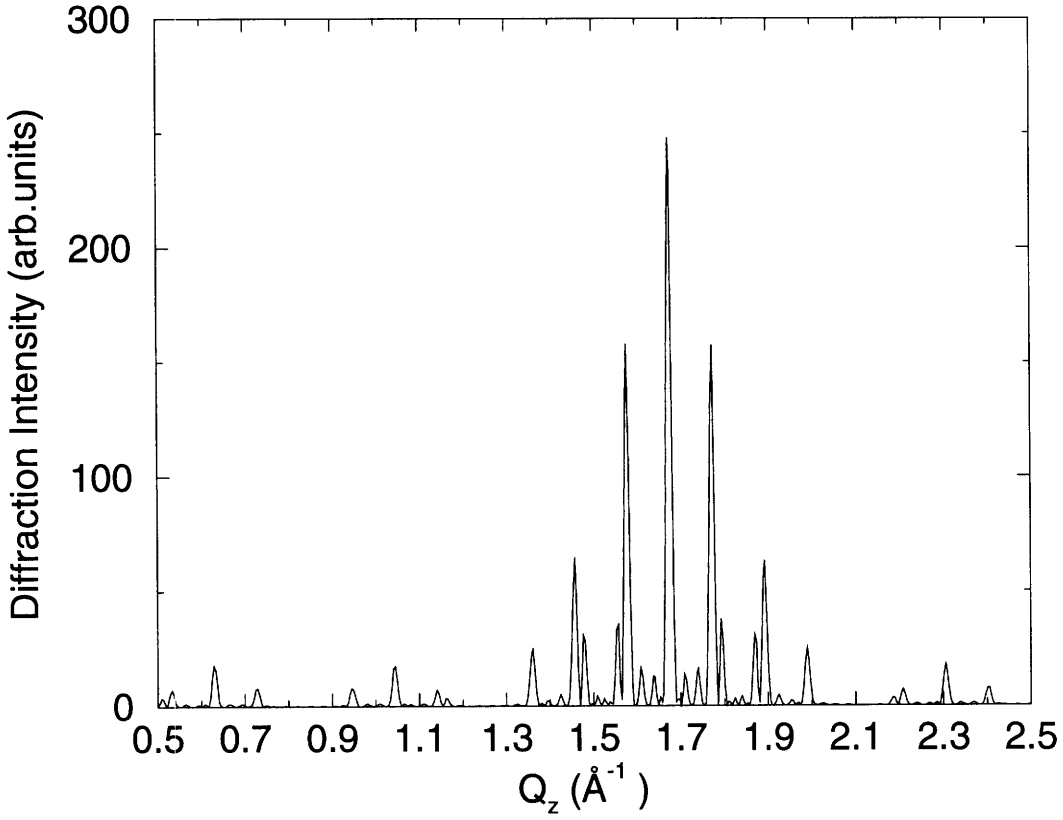

Figure 3-12: A simulated in-field (with a sufficiently large H field to align all the spins) diffraction scan for T< T_c along the [111] axis through the (1,1,1) reflection point for an EuTe(4)/PbTe(12) SL. Note the absence of diffraction structure near the $(\frac{1}{2}, \frac{1}{2}, \frac{1}{2})$ point, indicating suppression of the AF phase. The structure near the (1,1,1) point is consistent with a field-induced ferromagnetic phase, which appears at a sufficiently high external magnetic field.

Table 3.1: Average SL period thicknesses L obtained from neutron diffraction spectra and the best fits of x-ray diffractograms, including also the values of the diffraction linewidths expressed as the Full Width at Half Maximum (FWHM) intensity for the central magnetic peak of each SL and the corresponding coherence length.

nominal ξ/η	Δ (Å^{-1})	$L = \frac{2\pi}{\Delta}$ (Å)	L from x-ray (Å)	FWHM (Å^{-1})	$\frac{2\pi}{FWHM}$ (Å)
3/9	0.142	44.2	45	0.086	73.0
4/12	0.106	59.2	60	0.034	184.7
5/15	0.089	70.6	68	0.112	56.1

Chapter 4

Low Field Magnetization

4.1 Introduction

In magnetic studies, temperature and magnetic field dependent magnetization measurements ($M(T,H)$) provide important information on the magnetic couplings between spins as a function of continuously varying temperature and field. Specifically, we can extract information regarding magnetic anisotropy, different magnetic phases as a function of temperature, geometric effects on the magnetization, and inter-SL period coupling from $M(T,H)$ data.

The complementarity between magnetization measurements and neutron diffraction spectra cannot be over emphasized. Much of the conclusions drawn from the magnetization data rely on the spin arrangement in EuTe/PbTe SLs determined by the neutron diffraction data. However, those conclusions reach beyond what neutron studies alone can tell us. For example, while the spin arrangement deduced from neutron diffraction studies provides us with a basis to interpret the temperature-dependence of the magnetization as a SL geometric effect, the field-dependent magnetization suggests the absence of AF inter-SL period magnetic coupling, thus leading us to understand the neutron data in a new light. Specifically, if AF inter-period coupling is the correct explanation for the SL peaks seen in the diffraction spectra (see Fig.3-5), then we would expect to observe jumps in the $M(H)$ curves for ξ=odd SLs. With a sufficiently large external field H pointing upward $\uparrow$, the AF inter-period cou-

pling in an ξ=3 SL, i.e., ↑↓↑ PbTe ↓↑↓, will no longer be energetically favorable. At a certain threshold value for the H field, the spin arrangement should switch from ↑↓↑ PbTe ↓↑↓ to ↑↓↑ PbTe ↑↓↑ and such a transition should cause a jump in the $M(H)$ curve. However, the scenario described above is not observed in the $M(H)$ data. Therefore, we think that maybe the AF inter-period coupling is not the explanation for the observed SL peaks in the diffraction spectra, or the magnitude of the energy difference between the two spin configurations is too small to cause a measurable jump in the $M(H)$ curve.

4.2 Experimental Setup

All magnetization measurements were made using a commercial SQUID (Superconducting Quantum Interference Device) magnetometer. Detailed information on the instrument can be found elsewhere,[41] and only the essential features are decribed here. Broadly speaking, the SQUID acts as a high sensitivity magnetic flux-to-voltage convertor which translates the sample magnetization to a voltage reading. Specifically, the sample is moved up and down inside a set of superconducting coils. If the sample has a magnetic moment, the changing magnetic flux through the superconducting coil will induce a current. The superconducting coil is coupled to the input coil of the SQUID sensor through a superconducting isolation transformer, so that any current created in the superconducting coil by the sample will induce a current in the input coil of the SQUID (see Fig.4-1 for the block diagram of our SQUID magnetometer). The SQUID sensor in our instrument is a weakly linked single-junction, i.e., a superconducting ring interrupted by a region of weak superconductivity. The sample's magnetic moment is read by the SQUID sensor using the Josephson effect with an RF bias which provides AC flux modulation. An in-depth technical description of the physics and engineering behind the commercial SQUID magnetometer is given by J. C. Gallop.[42]

The experimental setup also concerns the mounting of the sample inside the SQUID magnetometer. The sample is tightly fitted into a transparent plastic tube.

The plastic tube is taped to the end of the sample probe (see Fig.4-2). In addition, all temperature-dependent measurements presented here are obtained with the magnetic field applied parallel to the SL plane, i.e., the (111) plane, since both the hysteresis data and the neutron diffraction measurements (ref.[38]) indicate that the spins lie in the (111) planes below the magnetic ordering temperature. Finally, by choosing the external field parallel to the (111) planes, we also avoid any problems associated with the demagnetization field. The SQUID magnetometer instrument provides measurements for the temperature and magnetic field as well as the magnetization.

4.2.1 Background Signal

The available SQUID magnetometer limits the measurements to a temperature window from 1.7 K to 50 K. The lower limit is contrained by the magnetometer instrument, while the upper limit is constrained by the SL substrate. In each SL sample, there are approximately 50 micro-grams of EuTe, 200 micro-grams of PbTe and 30 milli-grams of BaF_2. Although both PbTe and BaF_2 are diamagnetic, and have a low susceptibility per gram, the amount of BaF_2 and PbTe overwhelms that of EuTe. Thus, above 40 K, the net magnetization signal ($M_{EuTe} - M_{BaF_2}$) is very close to zero and the measurement becomes unreliable.

For the magnetization measurements in the paramagnetic regime of EuTe (i.e., above T_c), we found that an external field of 500 gauss gives the best result for the low field magnetization. Applying fields smaller than 500 gauss will result in an overall signal that is too small for the instrument to capture. On the other hand, applying a field much larger than 500 gauss will add extraneous background from magnetic impurities residing in the sample vessel, i.e., the transparent plastic tube.

In order to systematically account for the diamagnetic contributions from the substrate, we have measured the magnetization of pure PbTe and pure BaF_2 vs. temperature and field (see Figs.4-3 and 4-4). Both BaF_2 and PbTe have a temperature-independent magnetization, and values of their susceptibilities are summarized in Table 4.1. In practice, each SL sample was weighed so that the corrections for the BaF_2 contribution could be made while the PbTe contribution to the magnetization

was not explicitly accounted for, because its mass is negligible compared to that of BaF_2.

4.2.2 Magnetic Units

The magnetometor gives readings of the magnetization in units of emu (electromagnetic units in the Gaussian system), and many published papers use either the Gaussian or SI unit systems. Thus, conversions between the two systems are helpful:

$$1emu = 1erg/gauss \tag{4.1}$$

$$1emu = 4\pi gauss\ cm^3 \tag{4.2}$$

4.3 Magnetic Anisotropy

Bulk EuTe is an ideal Heisenberg antiferromagnet which has isotropic interactions because the magnetic moments come exclusively from the spins of the strongly localized $4f^7$ electrons in the Eu^{2+} ions.[15] Bulk EuTe has a Neél temperature (T_N) of 9.8 K. For $T < T_N$, the spins on a single (111) plane are parallel, but spins on adjacent (111) planes are antiparallel (type II antiferromagnet, see Fig.4-5). The spins lie in the (111) planes in order to minimize the magnetic dipole-dipole interaction. [14, 43, 44, 45] Within the (111) planes, Battles *et. al* (ref.[43]) postulated a phenomenological in-plane anisotropy field H_a to explain their antiferromagnetic resonance (AFMR) data. Analysis of the data gave the value H_a=8 $\pm$ 4 gauss. However, later AFMR experiments by the same group (ref.[14]) negated their initial proposal, instead demonstrating that EuTe is an "easy-plane" antiferromagnet, i.e., H_a=0.

Our magnetization experiments confirm that the EuTe in EuTe/PbTe SLs has the same characteristics as that of bulk EuTe regarding the issue of magnetic anisotropy. In this context, Fig. 4-6 shows magnetic hysteresis measurements for three SLs at 4 K, which is below the magnetic transition temperatures of those three SLs. Hysteresis loops were observed for the H field $\parallel$ to the (111) plane. No hysteresis loops were

seen for H applied $\perp$ to the (111) plane, indicating that the spins are lying in the (111) planes in EuTe/PbTe SLs. The appearance of hysteresis loops in Fig. 4-6 also confirm the existence of long range magnetic order, independently of the neutron diffraction measurements. Furthermore, the absence of in-plane spin anisotropy also is applicable to EuTe/PbTe SLs, where we find that for external fields H applied in various directions parallel to the (111) plane, the corresponding $M(H)$ curves coincide, showing no detectable in-plane anisotropy. Figure 4-7 shows such two $M(H)$ curves measured along two random in-plane directions approximately 80° apart.

4.4 $M(T, H)$ near T_c

Temperature-dependent magnetization studies near T_c on EuTe/PbTe SLs were carried out in a small external magnetic field, i.e., $H \leq$ 10 gauss. We have chosen to use a small field because we are interested in the temperature dependence of the magnetization near the zero field condition. It was possible to measure the magnetization near T_c at such low fields because the magnitude of the signal is larger in this temperature range than at higher temperatures in the paramagnetic regime.

The magnetization increases monotonically for the EuTe(1)/PbTe(3) SL sample as it is cooled from 20 K to 1.7 K, as shown in Fig.4-8(a) where the magnetic moment of the EuTe(1)/PbTe(3) SL sample is plotted as a function of temperature in a measurement field of 8 gauss. When the same set of data is plotted as MT^2 vs. T in Fig.4-8(b), a straight line is obtained. This implies that EuTe(1)/PbTe(3) is in the paramagnetic phase for temperatures above 1.7 K. However, for the rest of the SL samples, with EuTe thicknesses larger than 1 ML per SL period, drastic departures from Curie behavior (i.e., $M \sim N(g\mu_B)^2 H/3k_BT$) are seen at low temperatures in the normalized magnetization plots shown in Fig.4-9(a-f). The sharp increase in the value of $M(T)$ below $\sim$ 10 K indicates that there is a magnetic ordering in these SLs. However the type of ordering, whether ferromagnetic or antiferromagnetic, is not clear from the $M(T)$ measurements alone. The neutron diffraction results, on the other hand, show definitively that the magnetic ordering in all EuTe/PbTe SLs is an-

tiferromagnetic. To further illustrate the ambiguity of using $M(T)$ measurements to determine the type of magnetic order in EuTe/PbTe SLs, we have also measured the $M(T)$ curves for an EuTe epilayer (3.1 μm thick) as an example of the temperature dependence for a bulk EuTe antiferromagnet and the results are shown in Fig.4-10. No doubt, the small thickness of EuTe in the SLs have changed the $M(T)$ behavior drastically, which we will discuss in detail in the subsequent sections.

The magnetic phase transitions observed in $M(T)$ for all SLs are driven by the dominant antiferromagnetic next-nearest-neighbor exchange energy J_2/k_B (-0.15 K) whose magnitude is larger in bulk EuTe than is the magnitude for the ferromagnetic nearest-neighbor exchange energy J_1/k_B (0.04 K). In fact, neutron diffraction measurements have shown clear antiferromagnetic spin arrangements in the various SLs.[38] However, the antiferromagnetic nature remains subtle in the $M(T)$ curves shown above, particularly the $M(T)$ curves for ξ=3 , ξ=5 and ξ=7 SLs. To illustrate the antiferromagnetic nature of these superlattices more clearly, we have measured $M(T)$ for the ξ=4 SLs with different external magnetic fields (see Fig.4-11), to take advantage of the difference between $\chi_\perp$ (magnetic field perpendicular to the spins) and $\chi_\parallel$ (magnetic field along spin direction) expected for an antiferromagnet. As H increases from zero [with $H \parallel$ to the (111) plane], the spins will first rotate in the (111) planes to a direction that is perpendicular to H, and then start to open up and project along the field direction. This is the typical spin dynamics of an antiferromagnet with easy-plane anisotropy.[46] For the ξ=4 SL in a field of H=10 gauss, we observe that $M(T \rightarrow 0)$ approaches zero, reminiscent of the $\chi_\parallel(T)$ of antiferromagnets (see Fig. 4-11(a)). Here we can assume that the susceptibility χ is directly proportional to M for the ξ=4 SL, because M is linear in H at a low temperature of 4 K in the temperature regime $T < T_c$. In contrast, $M(T)$ for the ξ=3, 5, and 7 SLs are strictly non-linear in H for the entire temperature regime $T < T_c$. Referring to Fig.4-11, we see that as the external field is increased, the magnetization $M(T \longrightarrow 0)$ increases. Whereas $M(T) \longrightarrow 0$ as $T \longrightarrow 0$ K for H= 10 gauss, a non-zero value is found for $M(T)$ as $T \longrightarrow 0$ for a probing field of H= 40 gauss. When H is further increased (e.g., to a field of 640 gauss), $M(T)$ for the ξ=4 SL becomes almost constant for $T \ll T_c$. Be-

cause of the very low field required to establish the canted spin phase, we expect the magnetization to probe $\chi_\perp$ increasingly as the field is increased. In Fig. 4-11 we see that $M(T = 0)$=0.91 $M_{\mathbf{max}}$ for H=640 gauss. Further, Fig. 4-11 also demonstrates that the ξ=4 SL has a single (111) magnetic domain, because we are able to observe pure parallel and pure perpendicular magnetic susceptibilities separately at low and high magnetic fields, respectively. In contrast, bulk EuTe, having a multi-domain magnetic structure, shows $M(T = 0) = (2/3)M_{\mathbf{max}}$ at H= 1000 gauss [Fig. 4-10], the factor 2/3 being the signature of the average of the $\chi_\perp$ and $\chi_\parallel$ components.

4.5 Determine T_c for SLs

The determination of the magnetic phase transition temperature (T_c) from magnetization studies is complicated by the external field we have applied in order to measure $M(T)$. An unambiguous probe of T_c usually can be obtained from neutron diffraction measurements. However, no complete temperature-dependent neutron diffraction studies could be carried out because of limited available neutron beam time. Here we present an approximate method to determine T_c using zero field cooling (ZFC) and field cooling (FC) magnetization measurements.

The specific $M(T)$ measurement protocol consists of the following: SL samples are cooled in zero field from $T \sim 300$ K to 2 K, a field of 10 gauss is applied at 2 K, followed by magnetization measurements as SL samples warming up to T=15 K with H=10 gauss, and finally the samples are cooled and their magnetization measurements are taken in the H field back to T=2 K again with H=10 gauss. Figure 4-12(a-f) shows the resulting $M(T)$ data, noting that there is a pronounced difference between the zero field cooled (closed circles) and field cooled (open circles) measurements for EuTe/PbTe SLs. The difference between the ZFC and FC measurements seen in the SL samples is caused by the presence of uncompensated magnetic moments in the SLs. The resultant $M(T)$ is lower in the ZFC than in the FC case, because, after quenching the sample down to 2 K in zero field, the magnetic domains are more randomly oriented. During the warming cycle, as T increases from 2 K upwards,

the ZFC $M(T)$ initially remains constant, then increases and peaks at a temperature where it converges with the FC $M(T)$. The ZFC $M(T)$ closely approximates the static susceptibility, and its rise and fall are due to the critical fluctuations taking place near the transition temperature. Therefore, we can use the convergence temperature of the ZFC and FC $M(T)$ traces in the *low field* limit to determine the magnetic transition temperature T_c in the SLs. The results of T_c so determined are summarized in the Table 4.2. Later in Chapter 6 we will compare the T_c values obtained from the susceptibility measurements to those of deduced from the ZFC and FC magnetization measurements.

4.6 Geometric Effect in $M(T)$

Based on the neutron diffraction experiments, the magnetic ordering of EuTe in SLs consists of ferromagnetically-ordered (111) planes and the spins on the adjacent planes are aligned antiparallel to each other (type II antiferromagnet). Therefore, we would expect to observe differences in $M(T)$ between SLs with odd numbers of EuTe MLs per SL period, and SLs with even numbers of EuTe MLs per SL period. Specifically, the odd-even effect refers to nonzero magnetization at T=0 for SLs with an odd number of EuTe MLs per SL period, while zero magnetization at T=0 would be expected for SLs with even numbers of EuTe MLs per SL period. The issue of inter-SL period magnetic coupling will be addressed further in Chapter 7. However, to quote the conclusion of that study, we believe there is a negligible amount of inter-period coupling, i.e., coupling on the order of 10^{-29} eV between adjacent SL periods for the ξ=4, η=12 SL. In order to demonstrate the qualitative difference in $M(T)$ between odd and even SLs, we have plotted the asymptotic limit of $M(T \longrightarrow 0)$ (extrapolated from Fig.4-9) vs. EuTe thickness per SL period in Fig.4-13 for SLs with ξ=3, 4, 5, 6 and 7 that show magnetic ordering. The EuTe(2)/PbTe(6) SL was not included on this plot. Although some kind of magnetic ordering at $T = 5.8$ K was suggested by the $M(T)$ data for the EuTe(2)/PbTe(6) SL, neutron diffraction measurements do not show type II antiferromagnetic order down to $T = 1.8$ K. Thus

we don't expect $M(T)$ for the EuTe(2)/PbTe(6) SL to behave similarly to the other "even" SLs (ξ=4 and 6) in the temperature range of our magnetization study.

The results of Fig.4-13 are very interesting in two regards. Firstly, there is an oscillation in the magnitude of $M(T \longrightarrow 0)$ from one SL to another as ξ is increased by 1. Secondly, the amplitude of $M(T \longrightarrow 0)$ decreases as ξ the EuTe thickness per SL period increases. Since we have normalized $M(T \longrightarrow 0)$ to units of emu per Eu atom, therefore, the decreasing trend of $M(T = 0)$ agrees with our expectation that the percentage of uncompensated spins out of the total number of spins decreases as the EuTe thickness increases. Further, the experimental ratio of $M(T \longrightarrow 0)$ for a SL with 3 EuTe MLs to that for a SL with 5 EuTe MLs is approximately 1.67, in good agreement with the expected ratio of $\frac{1/3}{1/5}$=1.67. However, a similar comparison between the 5 ML SL to the 7 ML SL yields an experimental ratio of 2.6, much larger than the expected value of $\frac{1/5}{1/7}$=1.4. This deviation may be caused by the differences between the nominal ξ values and the actual ξ values for those two SLs.

4.7 Mean-Field Analysis of $M(T)$

4.7.1 ξ=odd SLs

We have postulated that the monotonic increase of the FC $M(T)$ with decreasing T shown in Fig. 4-14 for $T < T_c$ is caused by the extra plane of uncompensated ferromagnetically ordered spins in ξ = odd SLs (referring to the SL notation EuTe(ξ)/PbTe(η)). It would appear that these $M(T)$ curves should be described by the temperature variation of the sublattice magnetization, i.e., the Brillouin function for a mean field approach. The broken lines in Fig. 4-14 are generated by the Brillouin functions $B_{\frac{7}{2}}(E_{ex}/k_BT)$, where E_{ex} is the exchange energy yielding the observed T_c. The fact that these fits lie consistently lower than the experimental $M(T)$ data, is exactly what has been reported previously for the temperature dependence of the order parameter (i.e., the sublattice magnetization) in EuTe by neutron diffraction.[35] A statistical model based on the existence of a biquadratic coupling in the magnetic

exchange Hamiltonian has previously been successful for explaining a similar discrepancy observed in MnO and NiO,[47] two prototype AFM II antiferromagnets. Thus, using the Hamiltonian

$$\mathcal{H} = -J_1 \sum_{nn} \vec{S}_i \cdot \vec{S}_j - J_2 \sum_{nnn} \vec{S}_i \cdot \vec{S}_j - q \sum_{nn,nnn} (\vec{S}_i \cdot \vec{S}_j)^2 \tag{4.3}$$

where nn and nnn denote the nearest and next-nearest-neighbor spin pairs, and J_1, J_2, and q are the bilinear and biquadratic exchange couplings, we obtain the solid curves shown in Figs. 4-14. In these figures we see that the solid curves fit the $M(T)$ data better than the broken lines [see Fig. 4-14], with q/J_2=1.5×10^{-3}. The g/J_2 value is comparable to the value reported for bulk EuTe in Ref.[35] (where $q/J_2 \sim 4.5 \times 10^{-3}$). The rounded corners in the measured $M(T)$ curves for $T > T_c$ are due to the magnetization in the paramagnetic state, which is not included in our fitting that only models the behavior of $M(T)$ for $T < T_c$.

4.7.2 ξ=even SLs

Equal fractions of the two spin orientations are expected for the EuTe monolayers (ML) in the $\xi = 4$ SL. Two types of EuTe monolayers are nevertheless expected. One type has both sides of a EuTe monolayer surrounded by EuTe MLs (which is called an interior layer), and the other type of EuTe monolayer (called an interface layer) has one side facing EuTe and the other side facing PbTe. In Fig.4-15, results for the calculated temperature-dependent magnetization of the two types of EuTe MLs are shown, where the calculation is based on the magnetic Hamiltonian given in Eq. (4.3), with the same value of the biquadratic coupling q as was used in Fig.4-14. In general, we see that the interface layers and interior layers have noticeable differences in the magnitudes of their magnetizations for $T < T_c$ because of the unequal number of nearest and next-nearest Eu neighbors, except at $T = T_c$ where $M(T_c) = 0$ for both types of layers, and at $T = 0$ K where $M(T)$ reaches the same saturation limit for both types of layers. In addition, the magnetic correlations along the [111] direction, between the first layer and the second layer, are temperature dependent

and have different magnitudes from the magnetic correlations between the first layer and third layer (or fourth layer).[48] Only at $T = 0$ K are all the magnetic interlayer correlations equal. This point is essential for understanding why the $\xi = 4$ SL shows a net magnetization. Therefore, for ξ=4 we have fitted the FC $M(T)$ data in Fig. 4-16 by the *difference* between $M(T)$ for the interface layer and the interior layer [see the solid line in Fig. 4-16], since the spins on the interface layer and on the interior layer are antiferromagnetically aligned with respect to each other.

4.8 Mean-Field Analysis of T_c

The mean-field calculation for the magnetic phase transition temperature T_c usually has about 10% error for bulk materials, and the result is expected to be even less reliable for 2-dimensional structures such as short-period EuTe/PbTe SLs. On the other hand, the reliability of a mean field model is somewhat greater than for most 2D magnetic structures because EuTe is a Heisenberg magnet with localized moments. Further, there have been successful examples of the use of the mean-field approach for studying critical properties of SLs.[49, 50] The Hamiltonian for magnetic interactions in bulk EuTe given in Eq.(4.3) has J_1/k_B and J_2/k_B equal to 0.04±0.01 K and −0.15± 0.01 K, respectively,[15] k_B being the Boltzmann constant. The biquadratic coupling term is very small and changes the T_c value by less than 0.1 K, and thus can be neglected. The mean field expression for T_c for bulk EuTe is $2S(S+1)(-6J_2)/3k_B$,[51] with $S = 7/2$, yielding $T_c = 9.5$ K, which is very close to the observed T_c=9.8 K for bulk EuTe.

For SLs with $\xi = 3$, the T_c (7.8 K) is noticeably lower from that of the bulk, so we use an iterative mean-field approach to find T_c, similar to the one suggested in Refs.[49, 50] Specifically, we obtain a self-consistent set of values for $\langle S_1 \rangle$, $\langle S_2 \rangle$ and $\langle S_3 \rangle$, the average magnetizations for the 3 EuTe monolayers in a SL cell, by computing $\langle S_n \rangle = SB_{7/2}(E_n/k_BT)$ where $B_{7/2}(x)$ is the Brillouin function for S=7/2 and E_n is the energy per atom on the nth layer ($n = 1$ or 2 since by symmetry $\langle S_1 \rangle = \langle S_3 \rangle$). Thus for ξ=3, we obtain $E_1 = 6J_1S_1 + (-3J_2 - 3J_1)S_2$ and $E_2 =$

$(-6J_2-6J_1)S_1+6J_1S_2$, yielding T_c =7.6 K, somewhat below, but close to the observed 7.8 K. When the same iterative procedure is applied to the $\xi = 4$ and 5 SLs, T_c values of 8.3 K and 8.9 K, respectively, are obtained. Again these values are lower than the experimental T_c values. Regarding the discrepancy between calculated mean-field T_c values and the experimental T_c values, we note first of all that the mean-field calculation is only an approximation. Secondly, the input values of J_1 and J_2 used for the mean-field calculations were bulk values. However, we know there is a lattice mismatch between EuTe and PbTe which creates changes in both the in-plane ((111) planes) EuTe lattice constant and the out-of-plane lattice constant along the [111] direction. Although the trends for J_1 and J_2 as a function of interatomic distance have been suggested by previous work,[52] it is difficult to correct J_1 and J_2 quantitatively for the small changes of the interatomic distances in EuTe/PbTe SLs, given the large uncertainties reported in Ref.[52]. Nevertheless, our qualitative estimate shows that the strain possibly causes an increase in T_c by as much as 2 K. In Section 7.9 we will further address the issue of J_1 and J_2 values in SLs by Monte Carlo simulations.

4.9 Discussion

In Chapter 2 and the preceding sections, we have presented data on various aspects of the structural and magnetic properties of the EuTe/PbTe SLs. In this section we bring them together to give a more cohesive view of the EuTe/PbTe system. Before doing that, we put our work in perspective with other closely related studies.

Broadly speaking, much theoretical and experimental effort in studying antiferromagnetic SLs has gone into investigation of the interlayer couplings in FeF_2/CoF_2 and CoO/NiO superlattices,[49, 50, 53, 54] both of which have two antiferromagnetic components. The MnTe/CdTe system is a good example of a superlattice system made of one antiferromagnetic and one non-magnetic component. However, the studies on MnTe/CdTe focus mainly on the influence of strain on the magnetic structure of the frustrated FCC antiferromagnet MnTe (AFM III) and the effect of interlayer coupling.[55, 56] In contrast, the EuTe/PbTe system has a different type of antiferro-

magnetic component (AFM II) and the strain does not change the magnetic structure of EuTe. We therefore focused our work on the magnetic effects associated with the very small thicknesses of the magnetic layers.

Within the EuTe/PbTe SL system, the present work builds on earlier work by Heremans and Partin[17] who investigated similar (111) EuTe/PbTe SLs (Ref. [3]) but mostly focussed on the magnetic properties in the paramagnetic regime,[17] whereas the measurements reported here are almost exclusively on magnetic effects near and below T_c. Their findings, partiularly the values of Curie-Weiss temperature θ could be useful to us, except that the TEM images of their SL samples do not suggest SL structures. Further, no x-ray data about their SL samples were provided in their published work.[17] Recently, Kostyk *et al.*[18] studied (100) oriented EuTe/PbTe SLs,[18] which involve a different lattice geometry from the work presented here. In their SLs, each SL period consists of a few EuTe (100) planes. Specifically, three SLs with ξ=1, 4, and 8 and same η=30 were reported in their paper. The spins in the (100) planes are antiferromagnetically aligned with their nearest-neighbors within the plane. In contrast, in our SLs each SL period is composed of a few MLs of EuTe (111) planes, and the spins within the same plane are *ferromagnetically* ordered. Because of the antiferromagnetic spin arrangement in the (100) planes, Kostyk *et al.*[18] observed a reduction in the magnetic phase transition temperature, with a dependence of T_c on the number of magnetic layers, but the $M(T)$ curves themselves are very similar to those of bulk EuTe. The reduced T_c values they have reported for SLs with 4 and 8 ML per SL period are 7 K and 9 K, respectively. These values cannot be directly compared with T_c values for our SLs of similar thickness, because the number of nearest and next-nearest neighbor spins with J_1 and J_2 couplings are significantly different for (111) and (100) oriented EuTe layers.

4.9.1 Comparisons Between Bulk EuTe and EuTe SLs

In the present work, we have shown important differences in the temperature dependence of $M(T)$ for EuTe/PbTe SLs and bulk EuTe (Figs. 4-9 and 4-10). A second difference involves the incomplete spin cancellation that is observed in the antiferro-

magnetic SLs. For example, in order to obtain a magnetic moment per Eu atom for bulk EuTe (see Fig.4-10) of comparable magnitude as compared with the observed magnetic moment per Eu atom for the ξ=3 SL as shown in Fig. 4-9(b), a magnetic field of more than 20 times larger has to be applied to the EuTe bulk sample than for the ξ=3 SL. This result shows that there is a large enhancement of the magnetization due to the incomplete spin cancellation in the magnetic SLs. This geometric effect is further confirmed by comparison between our results and those obtained from the (100) EuTe/PbTe SLs by Kostyk *et al.*,[18] where the spin structure consists of stacks of antiferromagnets on a square lattice, and where only a factor of two enhancement in M is observed between their SLs and a (100) EuTe film. Furthermore, the (100) EuTe film reported by Kostyk *et al.* has almost an identical magnitude of the magnetization and $M(T)$ profile as we report here for bulk EuTe.

The difference in $M(T)$ among the (111) oriented SLs studied in the present work is not likely to be coincidental. Excluding the ξ=2 SL which does not exhibit the type-II antiferromagnetic order in the temperature regime (i.e., T>2 K) where we carried out our $M(T)$ measurements, we see in Fig.4-9 that the normalized magnetization steadily decreases in going from ξ=3 to ξ=7. The $M(T \longrightarrow 0K)$ limits for $\xi \geq 3$ SLs exhibit oscillations between ξ=odd and ξ=even as shown in Section 4.6 (see Fig.4-13). In addition, the $M(T)$ for the ξ=4 SL mimics a typical antiferromagnet in different H fields (Fig. 4-11), but the SLs with ξ=3, ξ=5 and ξ=7 show a much different $M(T)$ behavior to that of the ξ=4 SL under the same conditions. Finally, the areas within the hysteresis loops (Fig.4-6) for the ξ=3 and ξ=5 SLs are larger than that of the ξ=4 SL, consistent with the $M(T)$ measurements. Further comparisons between the magnetization results for ξ=even and ξ=odd magnetic SLs are made in Section 4.9.2.

4.9.2 Relation Between Structural and Magnetic Measurements

The x-ray diffraction and ESR measurements for our (111) EuTe/PbTe SL samples show that the SLs have approximately square wave compositional modulation with

quite abrupt interfaces and a long range coherence length. However, from the x-ray analysis the actual EuTe layer thicknesses in the SLs turned out to be somewhat larger than the nominal EuTe thickness values. Since also layer thickness fluctuations of the order of typical ± 1 ML due to interface roughness have to be taken into account, our model probably represents an over-simplified description of the magnetic behavior of the SLs. In Chapter 7 we will further address the magnetic effects for ξ=non-integer cases. Nevertheless, there remains a dramatic difference in the temperature-dependent magnetization behavior and the hysteresis loops between the SL samples and bulk EuTe, exhibiting ferromagnetic-like behavior in cases of the $\xi = 3$, $\xi = 5$ and $\xi = 7$ SLs in contrast to the antiferromagnetic-like behavior that is observed for the $\xi = 4$ and $\xi = 6$ short period SL. These differences can be explained by consideration of the uncompensated spins present in the EuTe layers designed to contain only a very small number of ferromagnetically-ordered (111) atomic planes, which are antiferromagnetically coupled between adjacent planes. However, in view of our x-ray results, a more detailed analysis of the magnetic results would be needed to demonstrate that the oscillating magnetic behavior observed as ξ goes from 3 to 7 is related to the presence of even or odd numbers of ferromagnetic monolayers in each SL period. Specifically, a more detailed model would need to take account of the real structure of the SL samples, including interface roughness and layer thickness fluctuations that are inherent to the usual MBE growth process, whereby a sample nominally designated as $\xi = 4$ actually may have local parts with ξ =3 or 5.

4.10 Summary

In this Chapter, we have investigated the spin arrangement and the magnetic anisotropy in our SLs by $M(H)$ measurements. The $M(T)$ data were used to determine the values of the transition temperature T_c for our SLs. The temperature dependence of the magnetization that is unique to different ξ values is due to the small number of EuTe monolayers in each SL period. Specifically, the difference in $M(H)$ between H applied parallel to the SL plane, i.e., the (111) plane, and H applied

perpendicular to the SL plane for $T < T_c$ implies that the spins become oriented within the (111) planes below the magnetic ordering temperature, in agreement with neutron diffraction experiments. The absence of magnetic anisotropy from static magnetization studies verifies that EuTe in the superlattices remains as an "easy-plane" antiferromagnet as in bulk EuTe. Hysteretic magnetization measurements with H applied parallel and perpendicular to the (111) planes and the $M(T)$ behavior for the ξ=4 SL in different H fields show that EuTe/PbTe SLs have a single magnetic (111) domain. Further, EuTe/PbTe SLs show significant differences in $M(T)$, with ferromagnetic-like behavior observed for the (ξ=odd) EuTe(3)/PbTe(9), EuTe(5)/PbTe(15) and EuTe(7)/PbTe(21) SLs, and antiferromagnetic-like behavior for the (ξ=even) EuTe(4)/PbTe(12) and EuTe(6)/PbTe(18) SLs. These differences in the temperature dependence of the magnetization $M(T)$ are attributed to the different number of EuTe MLs present in each SL period. Finally, SL samples with different ξ values show distinctly different magnetic phase transition temperatures, with values of T_c increasing as ξ increases. This trend is reproduced by our calculations for transition temperatures using an iterative mean-field approach.

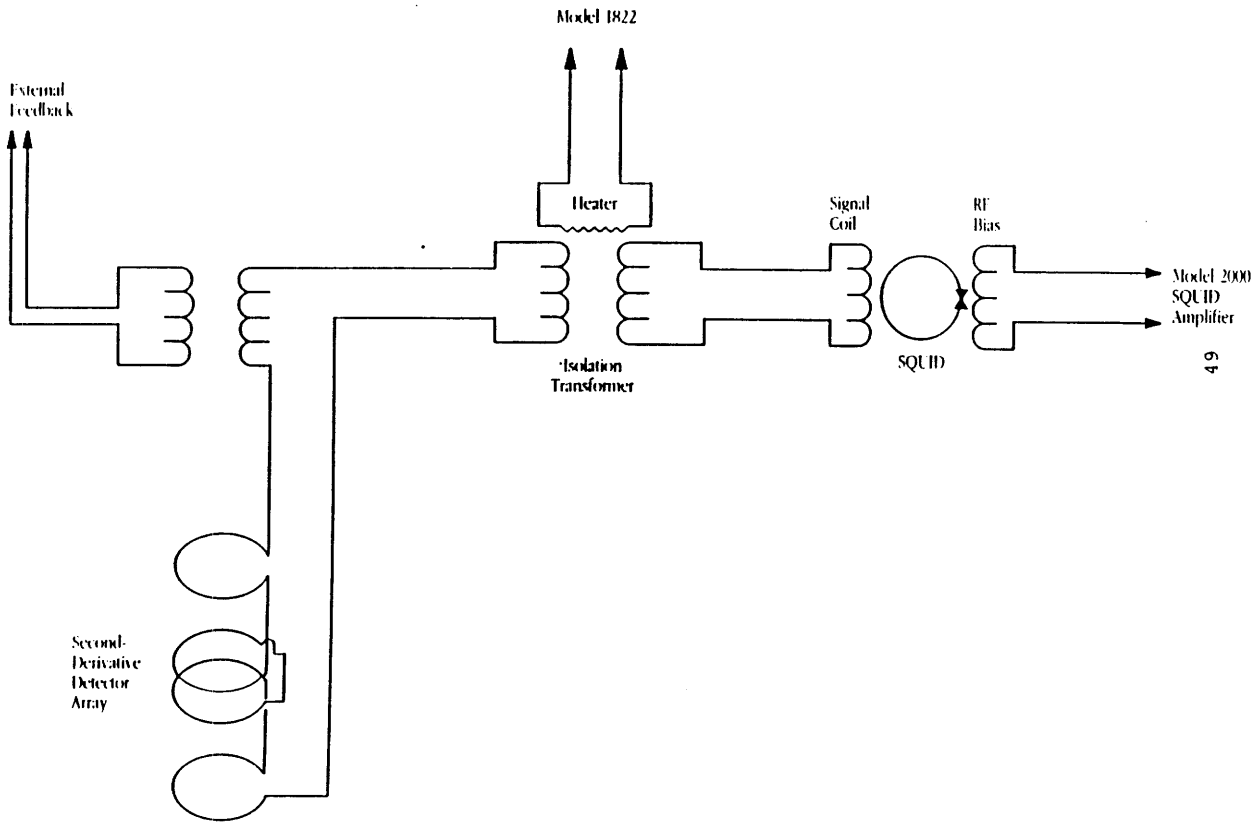

Figure 4-1: A block diagram for the MPMS5 SQUID system by Quantum Design Inc.

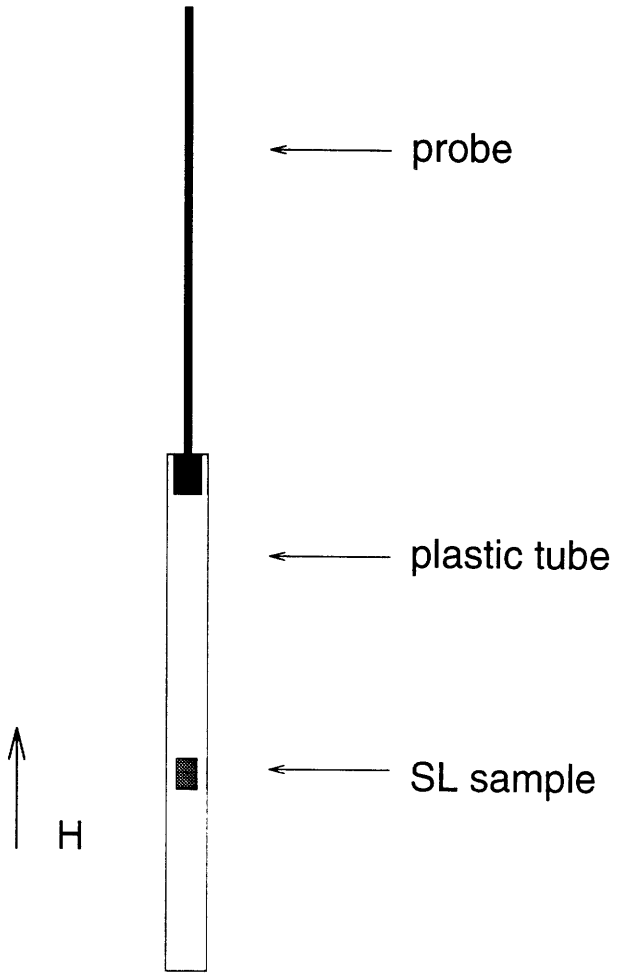

Figure 4-2: Sample mounting and orientation for magnetization studies.

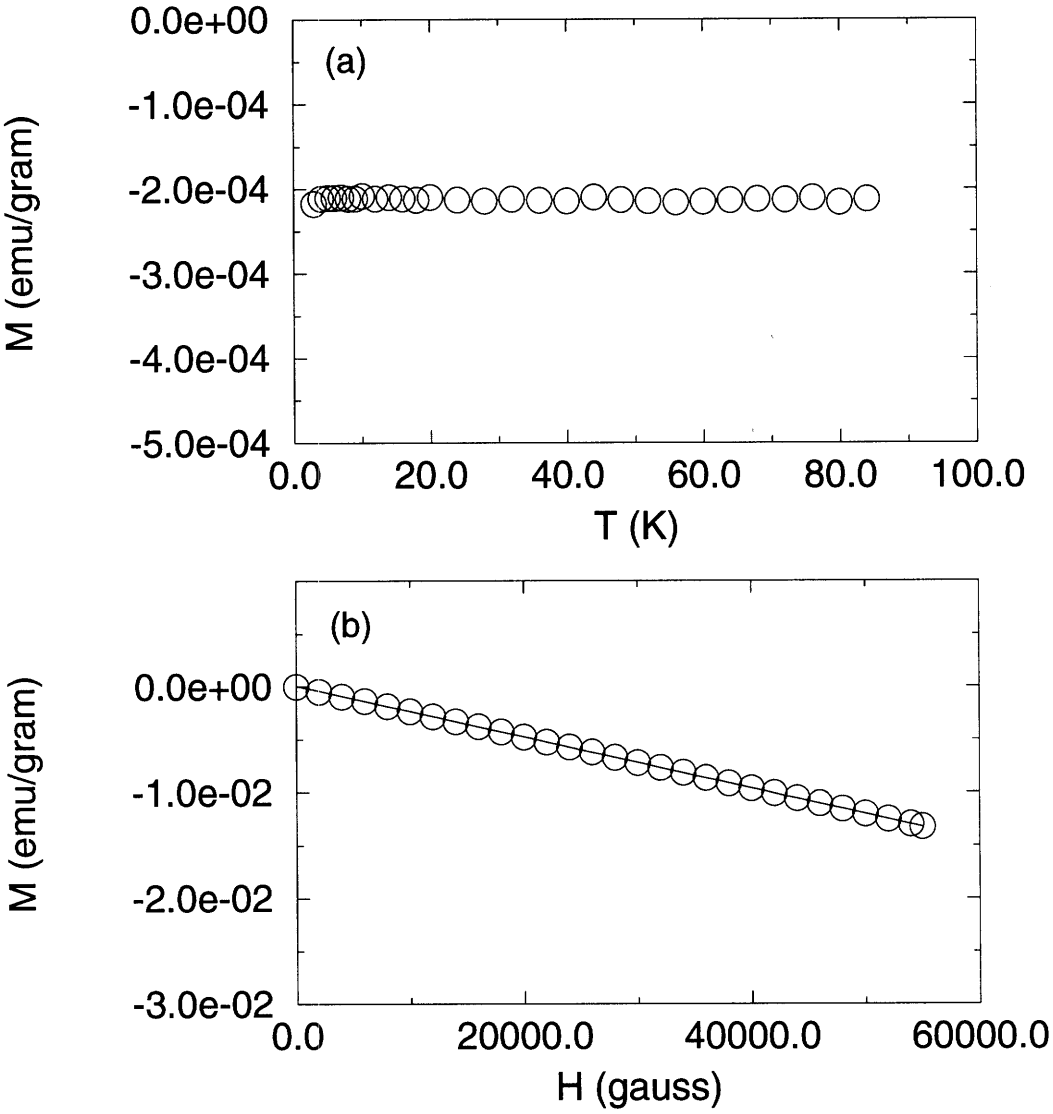

Figure 4-3: Normalized magnetization of BaF_2 vs. temperature measured with an external magnetic field H=1000 gauss (a); BaF_2 magnetization vs. magnetic field at T= 5 K (b). Note that e-04 denotes $10\times^{-4}$.

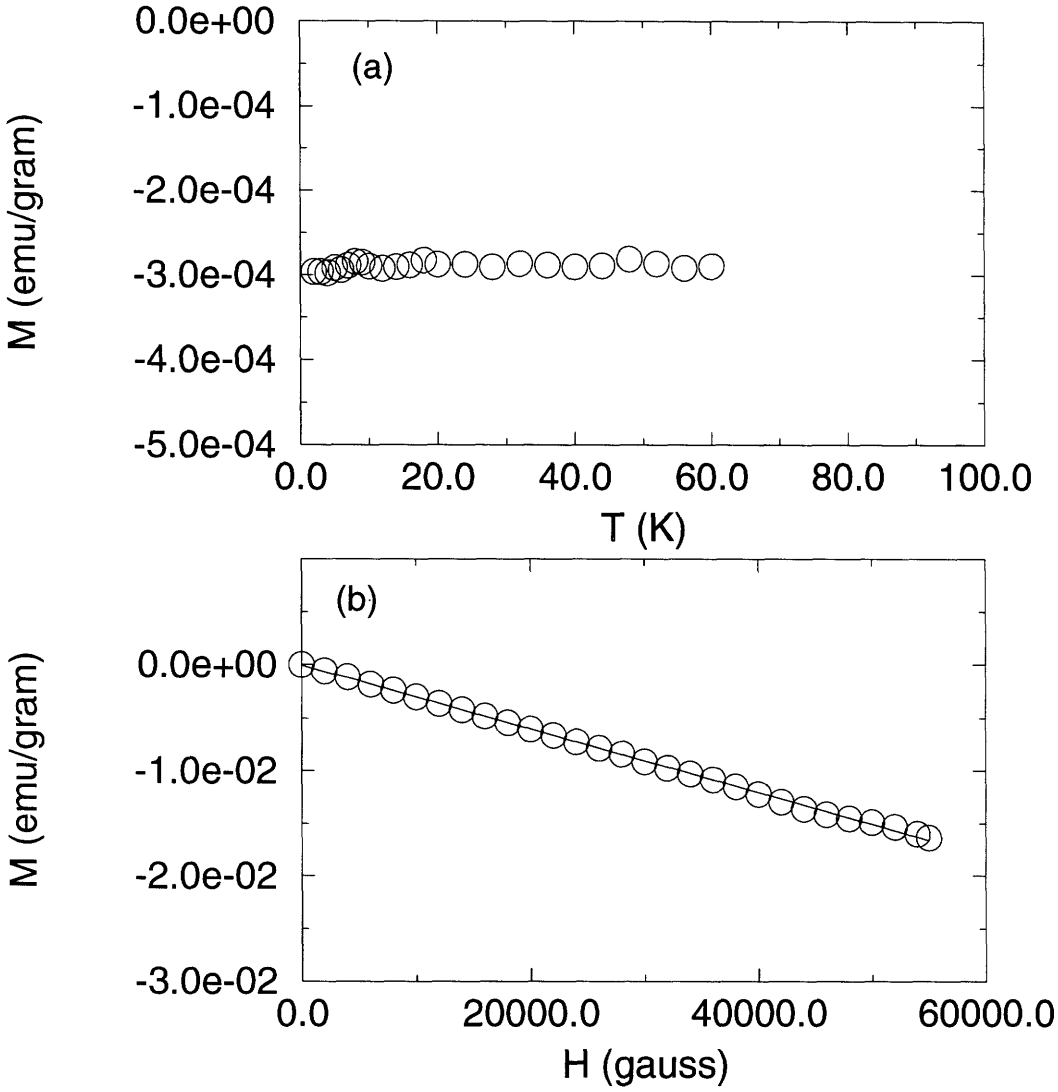

Figure 4-4: Normalized magnetization of PbTe vs. temperature measured with an external magnetic field H=1000 gauss (a); PbTe magnetization vs. magnetic field at T= 5 K (b). Note that e-04 denotes $10\times^{-4}$.

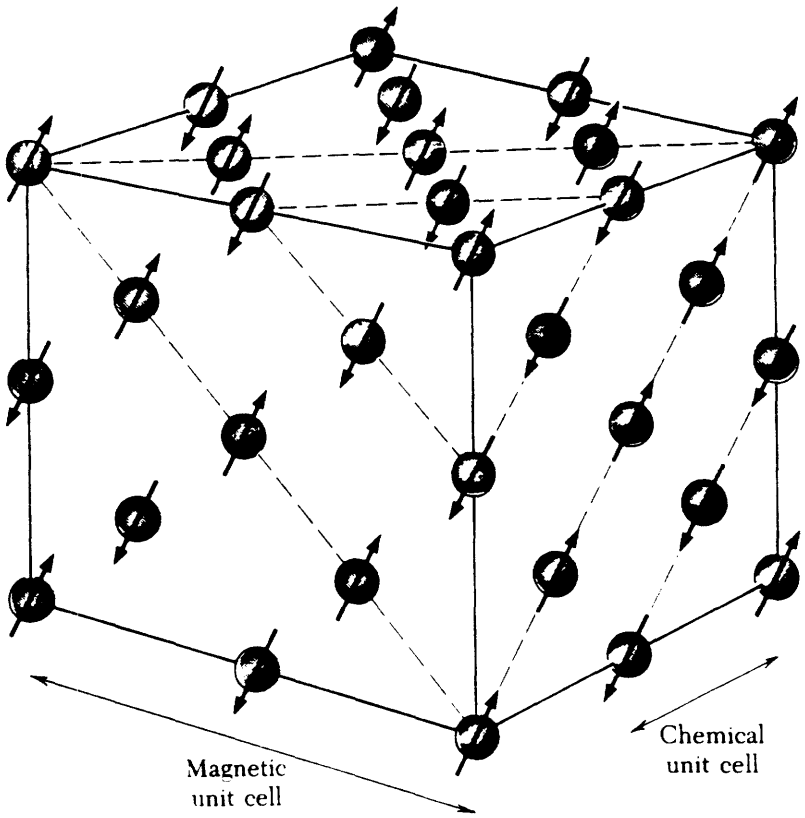

Figure 4-5: Spin arrangements of type II antiferromagnets.

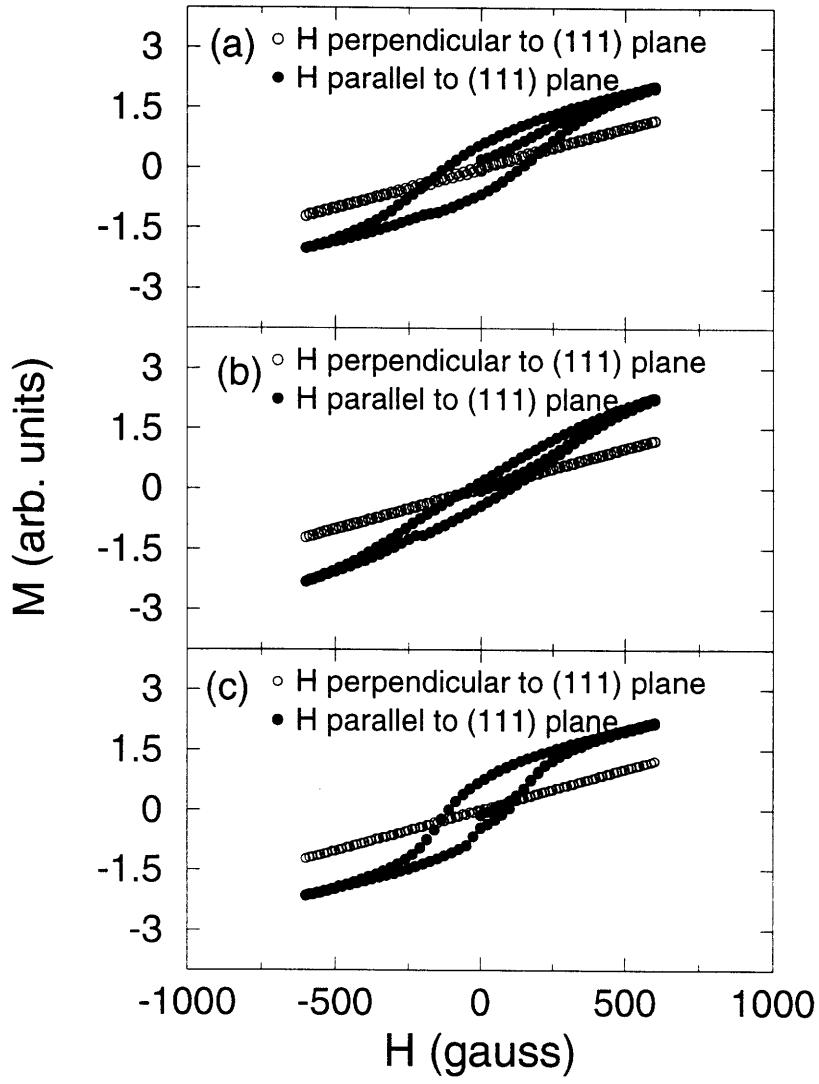

Figure 4-6: Hysteresis magnetization measurements at 4 K for an EuTe(3)/PbTe(9) SL (a), an EuTe(4)/PbTe(12) SL (b), and an EuTe(5)/PbTe(15) SL (c) for the magnetic field perpendicular and parallel to the (111) layer planes.

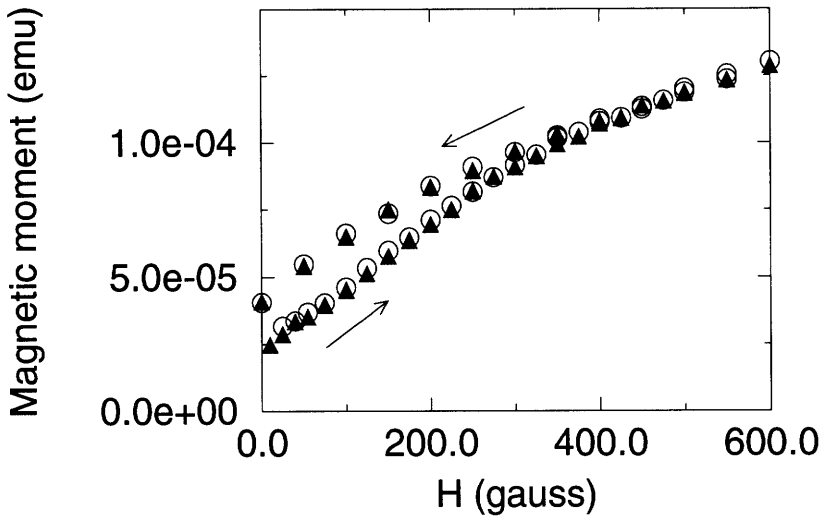

Figure 4-7: Magnetization vs. field for two randomly chosen directions 80° apart (closed triangles represent the measurements in one direction, and the open circles represent the measurements in another direction) within the (111) plane, for the EuTe(3)/PbTe(9) SL sample at T=4.7 K. The arrows indicate that the magnetic moments were measured as the external field H is either increasing or decreasing. The $M(H)$ values are higher when the H is decreasing than when the H is increasing because of the hysteresis effect shown in Fig.4-6. Again, that e-04 denotes $10\times^{-4}$.

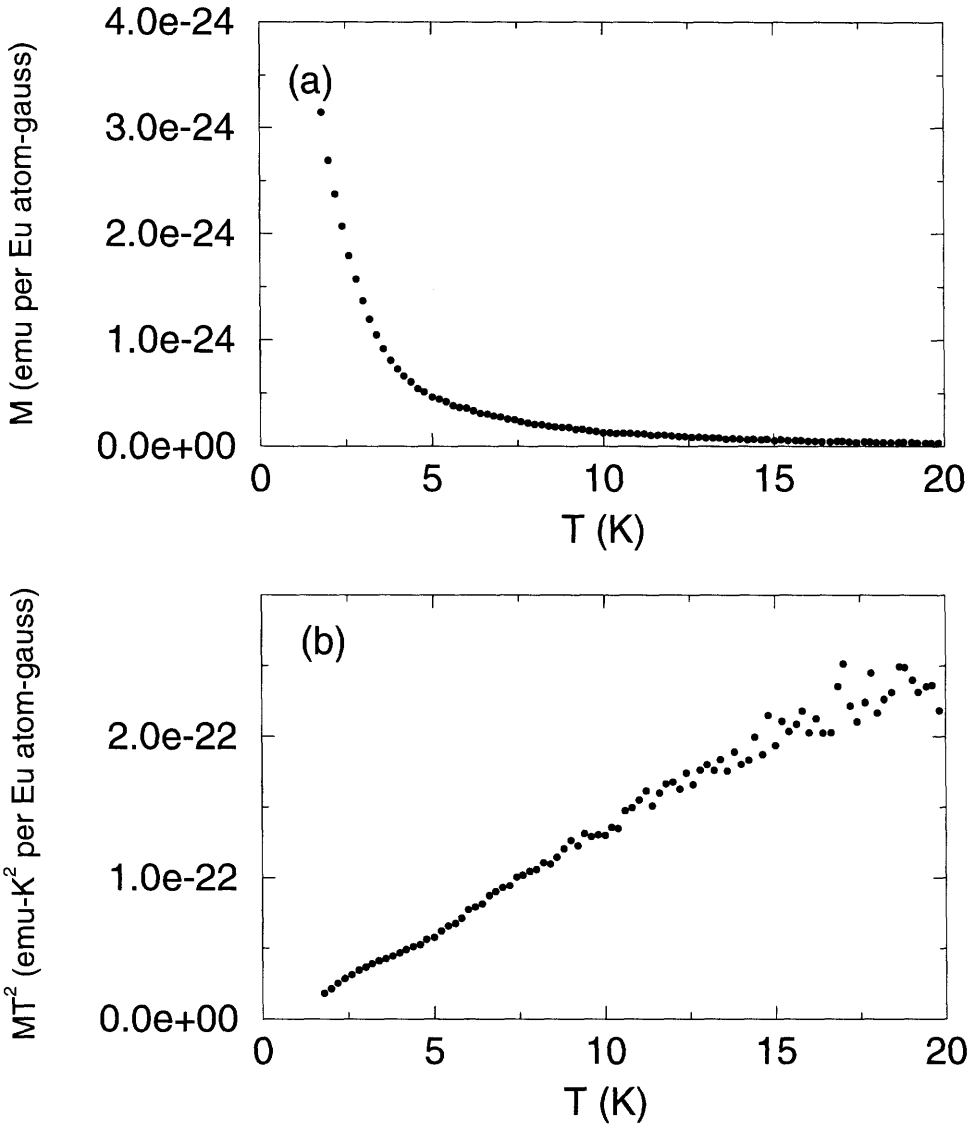

Figure 4-8: M vs. T for an EuTe(1)/PbTe(3) SL sample at H= 8 gauss (a). Same set of data as in (a) but plotted as MT^2 vs. T (b). Again, that e-24 denotes $10\times^{-24}$.

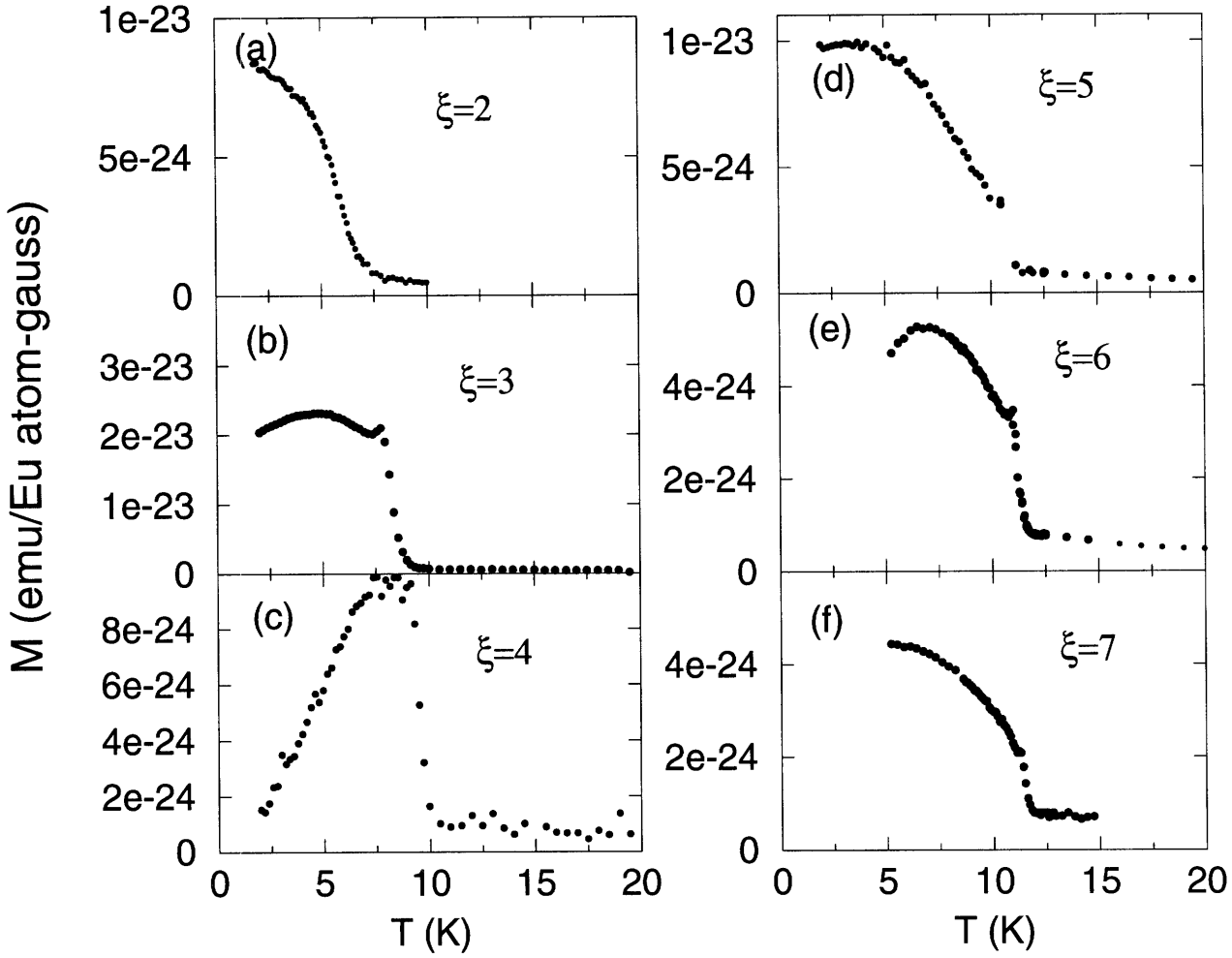

Figure 4-9: Normalized $M(T)$ measurements for an EuTe(2)/PbTe(6) SL (a), an EuTe(3)/PbTe(9) SL (b), an EuTe(4)/PbTe(12) SL (c), an EuTe(5)/PbTe(15) SL (d), an EuTe(6)/PbTe(18) SL (e), and an EuTe(7)/PbTe(21) SL (f). The normalized $M(T)$ is expressed as the magnetization per Eu atom, and e-24 denotes $10\times^{-24}$.

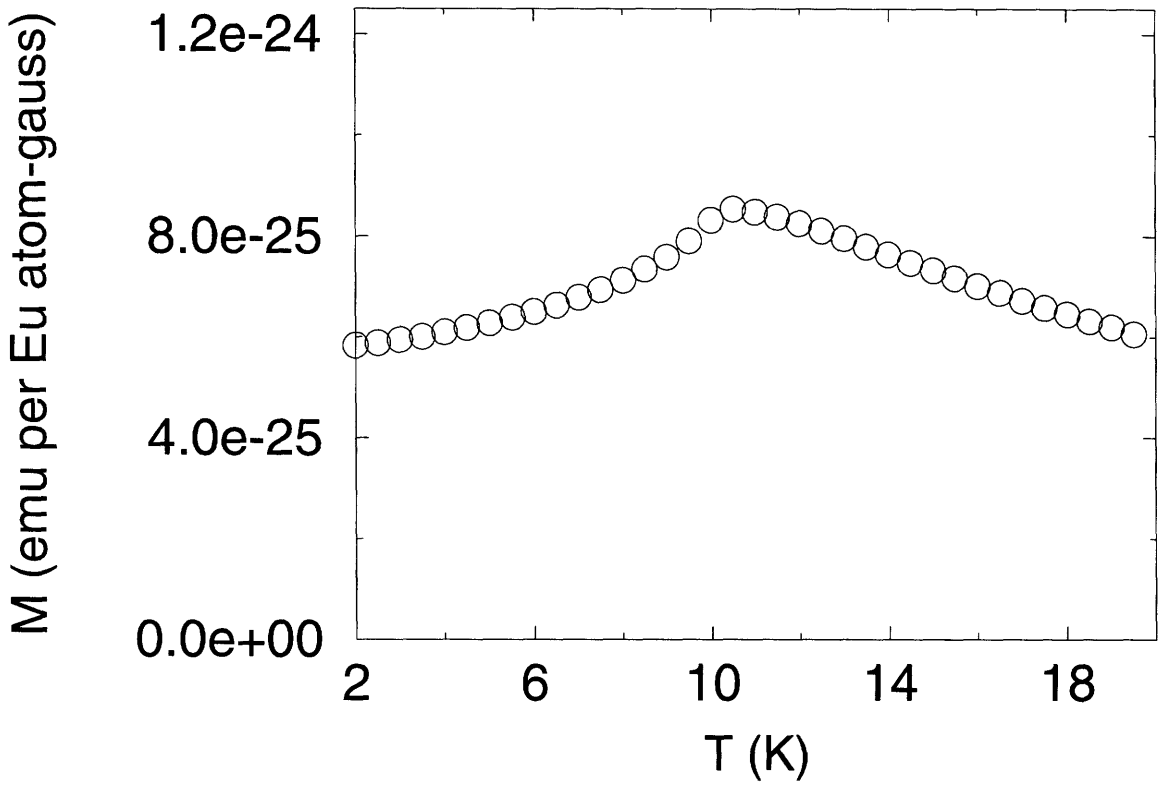

Figure 4-10: Normalized $M(T)$ measurements taken with H=1000 gauss for an EuTe epilayer 3.1 μm thick. The magnetization data, expressed in terms of emu per Eu atom, closely approximate the $M(T)$ behavior of a bulk antiferromagnet. The notation 1.2e-24 represents 1.2×10^{-24}.

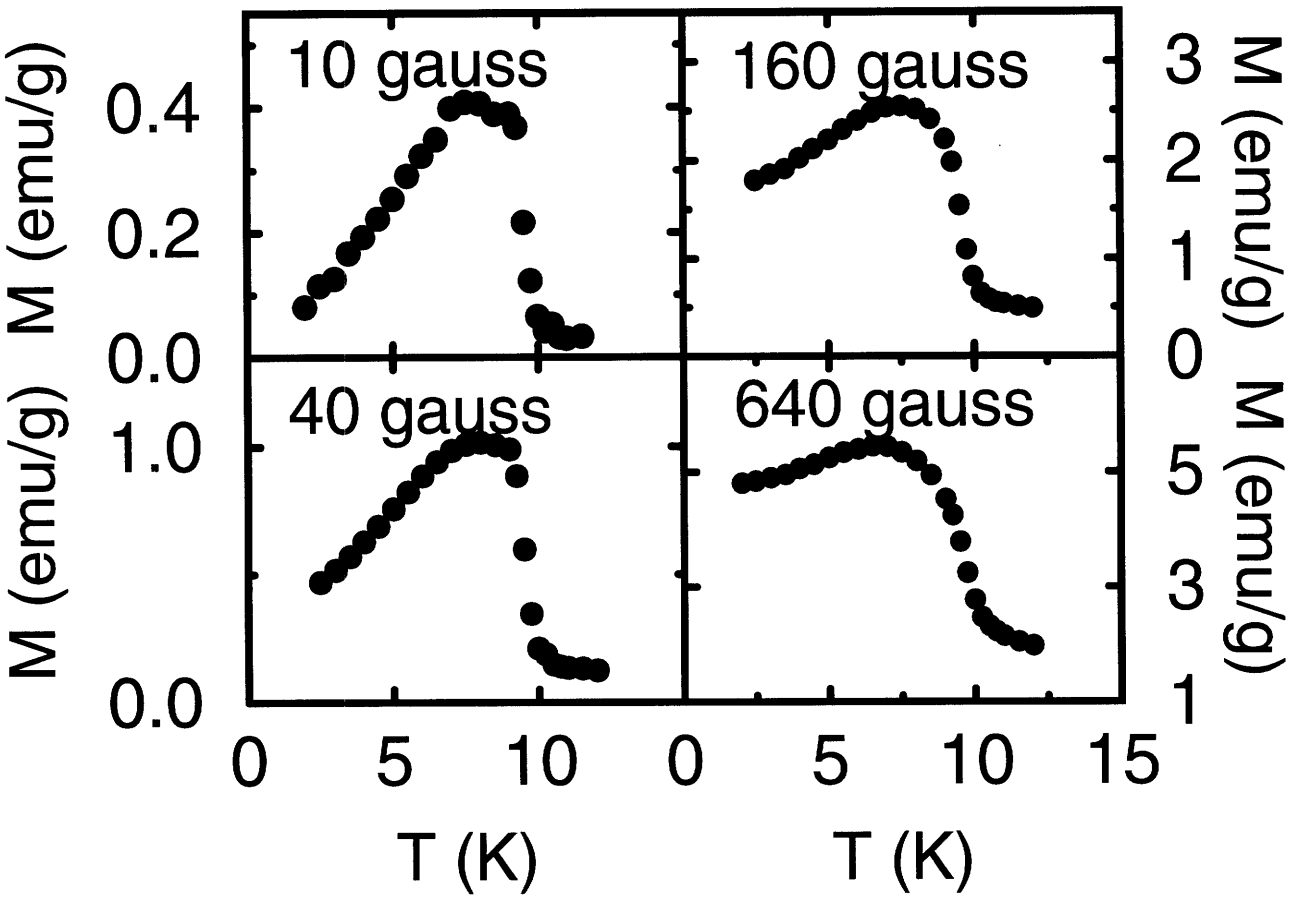

Figure 4-11: $M(T)$ for an EuTe(4)/PbTe(12) SL with different in-plane H measuring fields.

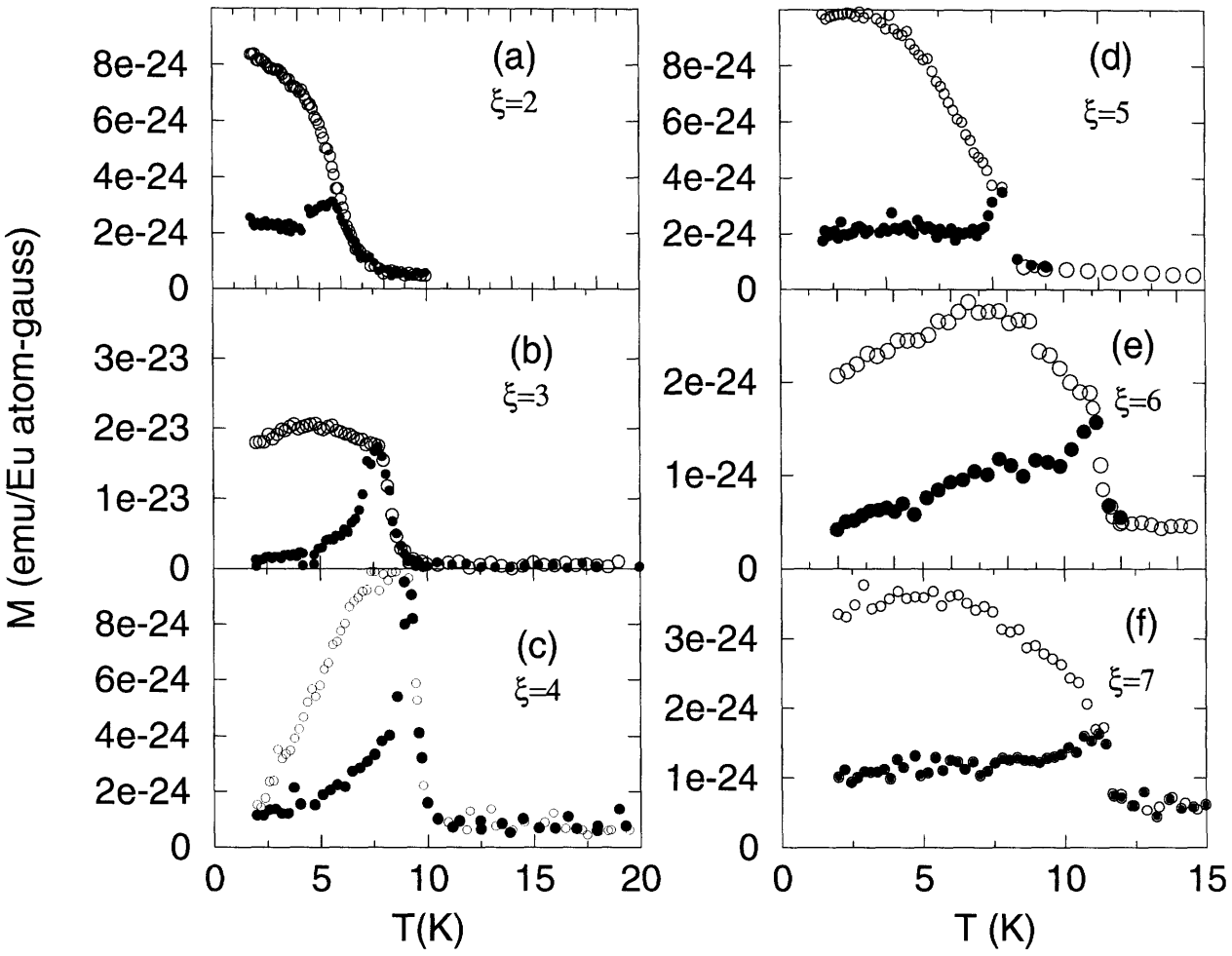

Figure 4-12: Normalized $M(T)$ measurements for an EuTe(2)/PbTe(6) SL (a), an EuTe(3)/PbTe(9) SL (b), an EuTe(4)/PbTe(12) SL (c), an EuTe(5)/PbTe(15) SL (d), an EuTe(6)/PbTe(18) SL (e), and an EuTe(7)/PbTe(21) SL (f), measured after FC (open circles) and ZFC (closed circles) cycles. The notation e-24 denotes 10^{-24}.

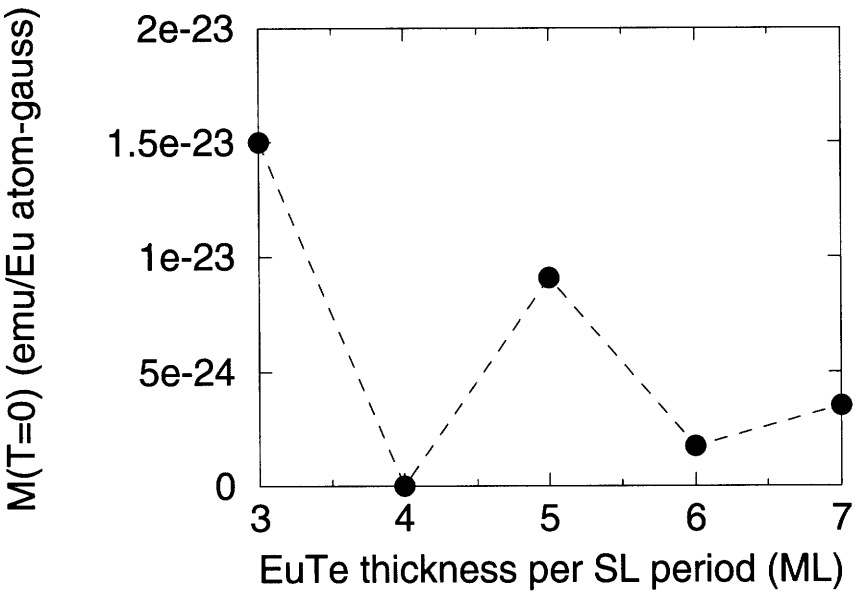

Figure 4-13: Asymptotic limits of $M(T \longrightarrow 0)$ for SLs with varying thicknesses of EuTe per SL period measured in the number of magnetic monolayers. The notation 1e-23 denotes $10\times^{-23}$.

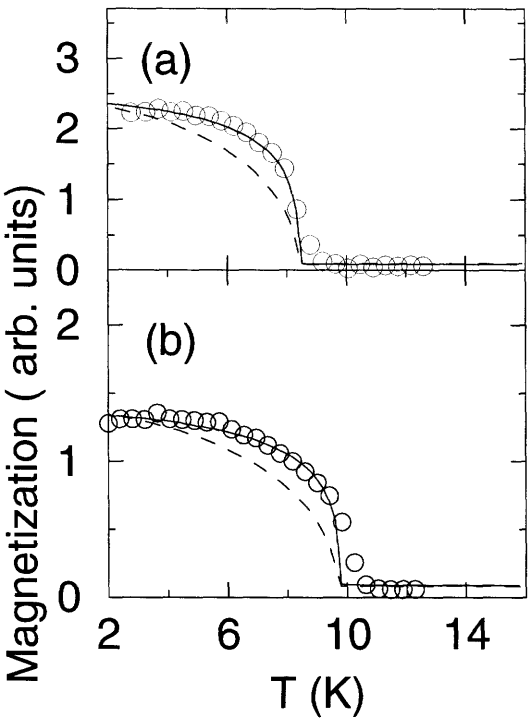

Figure 4-14: Mean-field fit to the field cooled $M(T)$ data of an EuTe(3)/PbTe(9) SL (a); and an EuTe(5)/PbTe(15) SL (b). The broken lines are Brillouin functions and the solid curves represent the mean-field model containing a biquadratic exchange term.

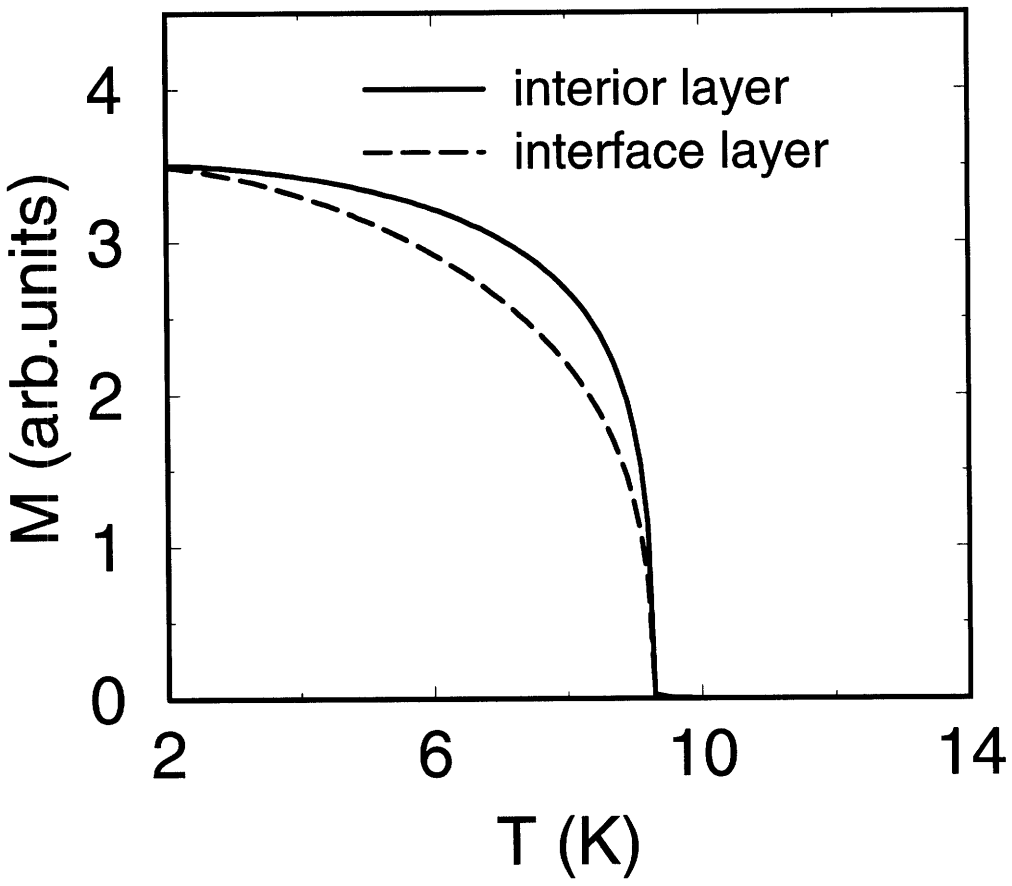

Figure 4-15: Temperature dependence of the interface and interior layer magnetizations in an EuTe(4)/PbTe(12) SL obtained by a mean-field calculation including biquadratic coupling.

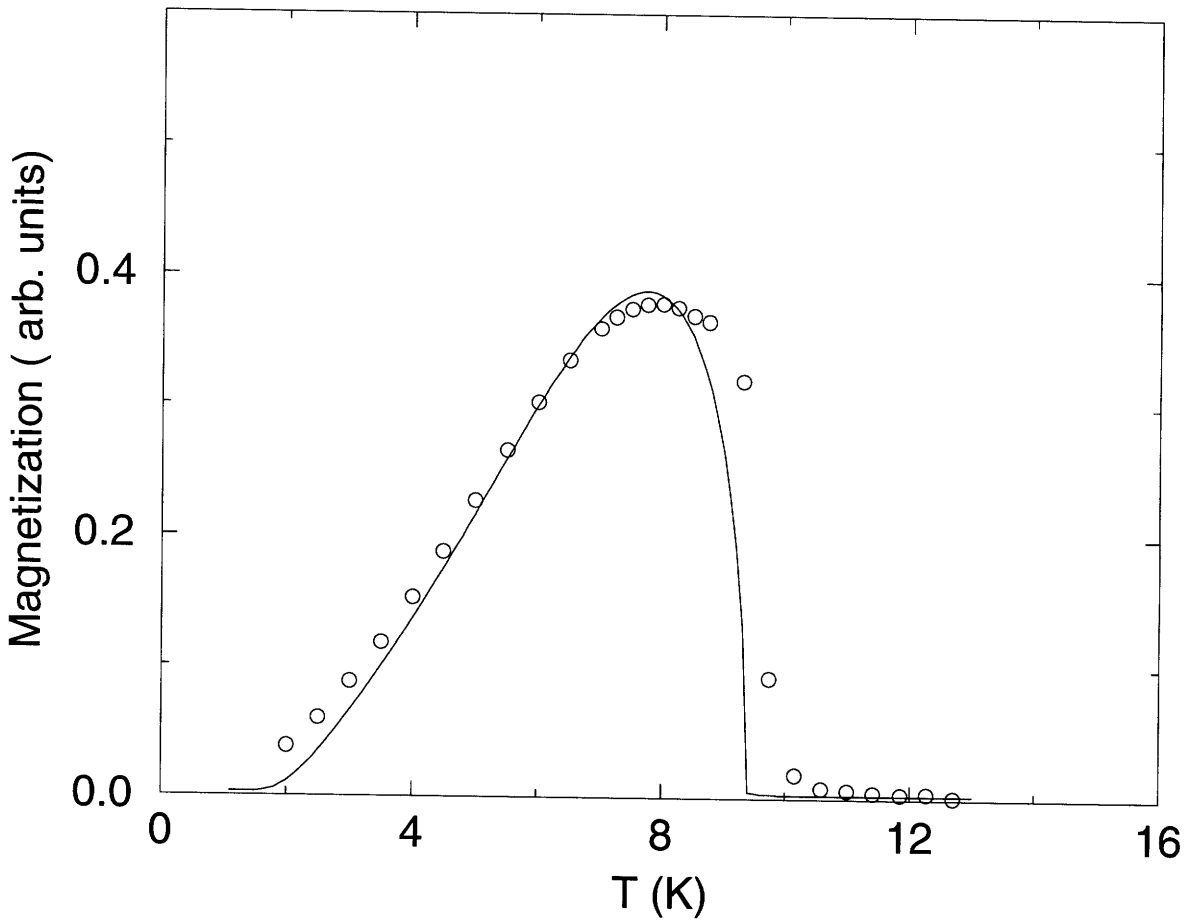

Figure 4-16: Mean-field fit to the $M(T)$ of an EuTe(4)/PbTe(12) SL.

Table 4.1: Magnetic susceptibilities for bulk BaF_2 and PbTe

	molar mass grams per mole	susceptibility emu/gram-gauss
BaF_2	175.3	-2.3×10^{-7}
PbTe	334.8	-3.1×10^{-7}

Table 4.2: Magnetic transition temperatures for SLs obtained from ZFC and FC $M(T)$ measurements

sample(ξ/η)	2/6	/3/9	4/12	5/15	6/18	7/21
T_c(K)	5.8	7.8	9.1	10.4	11.2	11.2

Chapter 5

High Field Magnetization

5.1 Introduction

In this chapter we present high field magnetization studies for four different SLs with ξ=2, 3, 4, and 5 (again referring to the SL notation EuTe(ξ)/PbTe(η)). The $M(H)$ data were taken for the magnetic field parallel to the SL plane up to 10 tesla at several temperature settings below the T_c of each SL sample. The phase diagram in the $H-T$ plane of bulk EuTe is shown in Fig. 5-1. In zero external field, the spins are in the AF phase. Since EuTe is an easy-plane antiferromagnet, as soon as a small external field is turned on, the spins will rotate, first to be perpendicular to the applied field. This process is usually called spin-flop transition (see Fig.5-2). The resulting spin configuration is called the canted AF phase. As the field continues to increase, the spins begin to orient along the magnetic field and eventually all the spins will be aligned in the field direction, so that the spins will be in the spin-aligned paramagnetic phase.

The transition from the canted AF phase to the spin-aligned paramagnetic phase in bulk EuTe takes place under relatively high field conditions. In the following section we present the data showing the canted AF to spin-aligned paramagnetic transition in EuTe/PbTe SLs. The linear region of the M vs. H curves was analyzed by a classical spin model at T= 0 K, and approximate phase diagrams in the $H-T$ plane are produced for the four SL samples with different ξ values. Further, the slope

of the M vs. H curves provide us with some information about the values of the exchange couplings J_1 and J_2. Normally one can extract the Curie-Weiss temperature θ from the $M(T)$ data to obtain the same information about J_1 and J_2, since in the paramagnetic phase, $M(T)=C/(T-\theta)$ where θ depends on a linear combination of J_1 and J_2. However, the fact that J_1 and J_2 are very small in EuTe, and the interference from the substrate signal is large compared with the contribution from the EuTe SL make measurements of $M(T)$ an impractical method for determining θ quantitatively. Specifically, we find that the value of θ changes from one set of data to another for the same SL. Thus the values of the Curie-Weiss temperature θ reported by J. Heremans and D.L. Partin [17] for their EuTe/PbTe SLs are likely to be only qualitative. Further, J. Heremans and D.L. Partin did not comment on the values of J_1 and J_2 implied by their Curie-Weiss temperatures, which seem to be very different from bulk values. For example, for their only superlattice that exhibits a magnetic phase transition, namely the EuTe(4)/PbTe(4) SL, the θ measured with H applied parallel to the SL plane is -4.46 K while the θ measured with H applied perpendicular to the SL plane is -6.37 K relative to the bulk value of $\theta=-4 \pm 1$ K.[15] To this end, the dependence of the slope of the M vs. H curve on J_1 and J_2 was explored as a method for obtaining a robust determination of J_1 and J_2.

5.2 Experimental Results

The high field $M(H)$ data were taken using a vibrating sample magnetometer (VSM) at the Francis Bitter Magnet Laboratory. A vivid description of the actual instrument can be found in Ref. [57]. Regretably the instrument has very low sensitivity (10^{-2} to 10^{-3} emu) for studying magnetic SLs. The H field is applied parallel to the (111) planes, and each SL that was measured contains approximately 50 micrograms of EuTe. Thus the magnetization signal is very small, and there is scatter in the measured $M(H)$ data due to the increased instrumental noise at high fields. Here in Figs.5-3, for the purpose of clarity, we only show $M(H)$ curves at three temperatures per SL, though we studied $M(H)$ at many more temperatures for each SL. All mag-

netization data are normalized to emu/gram, and the solid horizontal lines in Fig.5-3 represent the saturation magnetization for bulk EuTe (139 emu/gram). The mass of EuTe in the SL is obtained by multiplying the area of the SL by 5.4×10^{14} Eu/cm^2 and the number of (111) EuTe layers present in the SL sample. All $M(H)$ curves saturate at the value of the bulk saturation magnetization.

The transition from the canted-spin state to the paramagnetic state is a second-order phase transition accompanied by a discontinuity in the differential $M(H)$. However, because of noise in the $M(H)$ data, the derivative is not well defined. Instead, we chose to fit the $M(H)$ curve for $H>$ 0.5 tesla by a straight line, and we define the point where the $M(H)$ data start to deviate from the linear fit as the transition point from the canted-spin phase to the paramagnetic phase. In this manner, approximate boundaries for the four different SLs were obtained and the results are plotted in relation to the bulk EuTe phase diagram (see Ref.[58]) in the $H-T$ plane (see Fig.5-4). The phase boundaries in the H-T plane move to lower field and temperature values as ξ decreases from 5 to 2, consistent with the decreasing T_c values (see Table 5.1). The curves for $\xi\geq3$ are almost similar to that of bulk EuTe, whereas the curve for ξ=2 is rather different. The reason may be the following. The magnetization studies for the ξ=2 SL, both the low-field temperature-dependent $M(T)$ data in Chapter 4 and the high field $M(H)$ measurements presented here show some kind of phase transition as early as 5.8 K (mainly suggested by the ZFC and the FC $M(T)$ data). However, the elastic neutron scattering results on the ξ=2 SL sample show that type-II antiferromagnetic ordering doesn't emerge at T=4.2 K but rather appears at T= 1.8 K. However, the precise temperature between T=4.2 K and T= 1.8 K where the AF II order emerges is unkown to us from the neutron data. Figure 5-4 suggests a phase transition temperature above T=2 K for the ξ=2 SL. Thus, the last two points connected by the dotted line on the phase boundary shown in Fig.5-4 may be unreliable and may not represent the separation between a canted AF phase and a spin-aligned paramagnetic phase.

5.3 Data Analysis

In a zero temperature classical spin calculation, $M(H)$ for EuTe should follow a straight line (see Fig.5-5) for fields from zero to H_F, the magnetic field where $M(H)$ saturates at M_S. This model applies to systems for which the magnetic anisotropy can be neglected, and to cases of weak anisotropy of the easy-plane type, where $H>\sqrt{H_A H_E}$, in which H_A and H_E are, respectively, the in-plane anisotropy field and the exchange field. Bulk EuTe belongs to the latter category, with $H_A \sim 0$ gauss (within the (111) planes) and H_E=3.6 tesla.[14] EuTe in the SLs retains its bulk properties insofar as $M(H)$ is independent of field direction when H is applied parallel to the (111) planes (see Chapter 4). Also neutron diffraction studies show that the spins are lying in the (111) planes for $T<T_c$. In the $M(H)$ data shown in Fig.5-3, $M(H)$ curves are quite linear for $H>0.5$ tesla. Even the non-linear part in the low field limit perhaps has more to do with the uncompensated spins rather than with the in-plane anisotropy. Uncompensated spins form magnetic domains, under the influence of an external magnetic field and domain motion will result in a non-linear $M(H)$ behavior.

Since EuTe is a easy-plane type antiferromagnet, the spins will rotate to become $\perp H$ at very low values of H. Thus the AF phase occupies only a very small area in the $H-T$ diagram, and this area is essentially represented by a single line near H=0 in the $H-T$ plane. In the AF phase, the magnetizations of the neighboring (111) planes are equal and antiparallel to each other. For 0.5 tesla $<H<H_F$, EuTe is in the canted AF phase, where the magnetizations of the neighboring planes are equal in magnitude and make an equal but nonzero angle θ with H (Fig.5-5). The linear increase of $M(H)$ in this phase corresponds to the spins beginning to align along the field direction. After H exceeds H_F, the system enters the spin-aligned paramagnetic phase. In the zero temperature classical spin calculation,[59] the slope of $M(H)$ in the canted-spin phase can be calculated by considering the energy per atom for nearest-neighbor (n.n) and next nearest-neighbor (n.n.n) interactions,

$$E = \frac{(-6J_1S^2 - 6J_2S^2)\cos 2\theta - 6J_1S^2}{2} - 2HS\mu_B \cos\theta \qquad (5.1)$$

where J_1 and J_2 are, respectively, the exchange couplings for the n.n and n.n.n exchange interactions, μ_B is the Bohr magneton, S=7/2 for an Eu ion, and H is the external field. Minimizing the energy of Eq.5.1 with respect to the angle θ, we obtain

$$\cos\theta = \frac{-H\mu_B}{(6J_1 + 6J_2)S} \tag{5.2}$$

and the magnetic moment per atom in the field direction is then

$$M = S\mu_B \cos\theta = \frac{-{\mu_B}^2 H}{(6J_1 + 6J_2)} = (\frac{1}{6})\frac{-{\mu_B}^2 H}{(J_1 + J_2)}. \tag{5.3}$$

The coefficient of H in Eq.5.3 is the slope of the M vs. H curve. With J_1/k_B and J_2/k_B for bulk given as 0.04±0.01 K and −0.15±0.01 K, respectively,[15] and multiplying by the spin density 2.2×10^{21}/g, we find the slope of $M(H)$ to be 22 emu/tesla gram for bulk EuTe.

The slope $\partial M/\partial H$ obtained by the zero temperature classical spin calculation is on the same order of magnitude as the experimental values for both bulk EuTe and our SLs, for which values are given in Table 5.1. Also included in Table 5.1 are the values of transition temperature T_c for SLs determined by the field cooling and the zero field cooling magnetization measurements. The case of the ξ=∞ EuTe MLs in Table 5.1 refers to bulk EuTe, and the corresponding $\partial M/\partial H$ value is extracted from the data in Ref.[58]. It is not surprising that the experimental value of 15.5 emu/tesla-gram for bulk EuTe (which is measured at T=1.3 K) is smaller than our calculated value of 22 emu/tesla-gram which assumes T= 0 K and that the spins are classical vectors. For the EuTe/PbTe SLs the measured slopes of the $M(H)$ curves in the canted AF phase are temperature independent, but decrease as ξ increases (Table 5.1). This is consistent with our simple formulation, where we would expect the slope to decrease as ξ increases, due to the increase in the energy per Eu atom for larger ξ. Specifically, following above-described procedure in deriving the $M(H)$ relation for

bulk EuTe (see Eq.5.3), similar $M(H)$ relations for various SLs are obtained as

$$M = (\frac{1}{3})\frac{-{\mu_B}^2 H}{(J_1 + J_2)} \tag{5.4}$$

for the ξ=2 SL,

$$M = (\frac{5}{18})\frac{-{\mu_B}^2 H}{(J_1 + J_2)} \tag{5.5}$$

for the ξ=3 SL,

$$M = (\frac{1}{4})\frac{-{\mu_B}^2 H}{(J_1 + J_2)} \tag{5.6}$$

for the ξ=4 SL, and

$$M = (\frac{7}{30})\frac{-{\mu_B}^2 H}{(J_1 + J_2)} \tag{5.7}$$

for the ξ=5 SL.

5.4 Summary

The present study suggests there is a small effect (within the sensitivity of the vibrating sample magnetometer) on the strengths of the exchange couplings J_1 and J_2 when EuTe is reduced from the bulk down to 2 atomic monolayers in thickness. This result is reasonable considering that the lattice parameters of EuTe in SLs are very close to those of bulk EuTe based on x-ray investigations (see Section 2.5). The values of exchange couplings in going from bulk to the SLs should not change significantly because they are largely determined by the lattice constants. Unfortunately, the zero temperature classical spin model we have used for the $M(H)$ analysis is only an approximation, and this difficulty together with the low sensitivity of our VSM instrument prevented us from extracting meaningful individual J_1 and J_2 values from the $M(H)$ data. However, we feel that the high field magnetization study on EuTe/PbTe SLs is important because it provides us with a *reliable* indication of the sum of the J_1 and J_2 values, that otherwise would have been unknown to us. For example, one may be tempted to derive the strengths of J_1 and J_2 from the observed T_c values by a mean-field calculation. This method also lacks a solid basis, because

a 2D Heisenberg system, to which EuTe/PbTe SLs belong, is known to have T_c =0 K. A more elaborate model than the mean-field approach is thus required to extract the values of J_1 and J_2 from the measured transition temperatures. We will further discuss the magnetic model we chose for studying the EuTe/PbTe SLs in Section 7.7, where we present the results of Monte Carlo simulations.

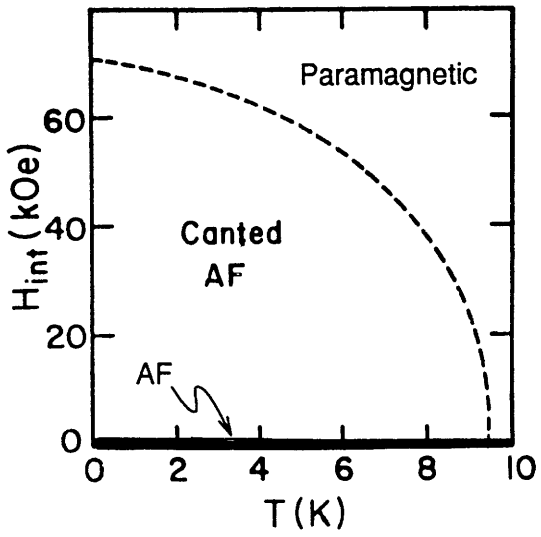

Figure 5-1: Phase diagram of EuTe in the $H - T$ plane. from Ph.D. thesis by R. P. Silberstein at M.I.T., 1978.

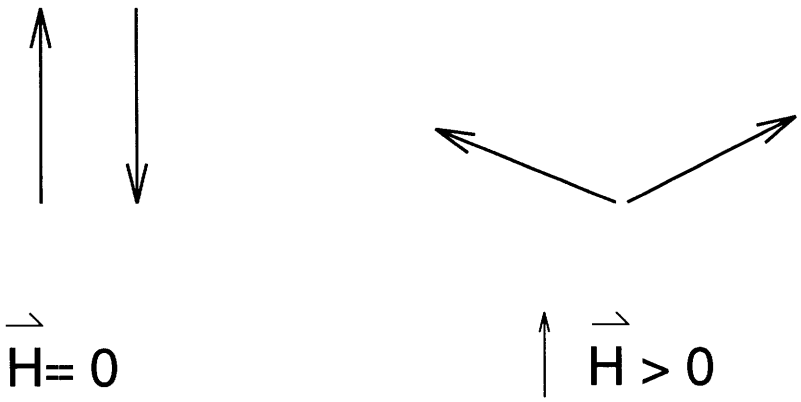

Figure 5-2: Spin-flop transition.

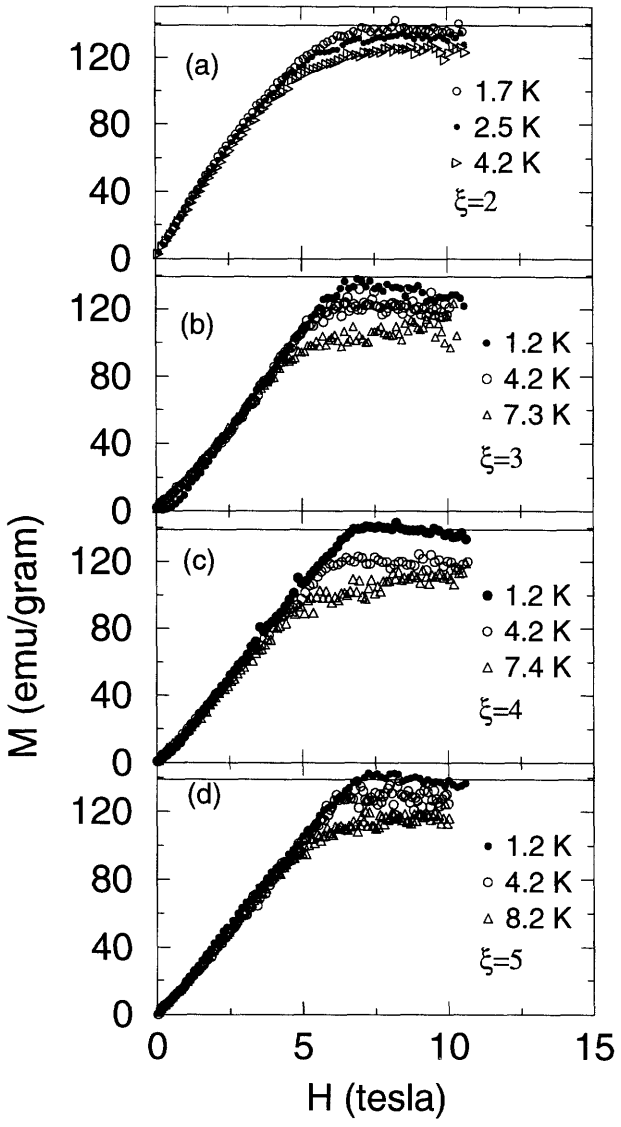

Figure 5-3: $M(H)$ curves for an EuTe(2)/PbTe(6) SL (a), an EuTe(3)/PbTe(9) SL (b), an EuTe(4)/PbTe(12) SL (c), and an EuTe(5)/PbTe(15) SL (d).

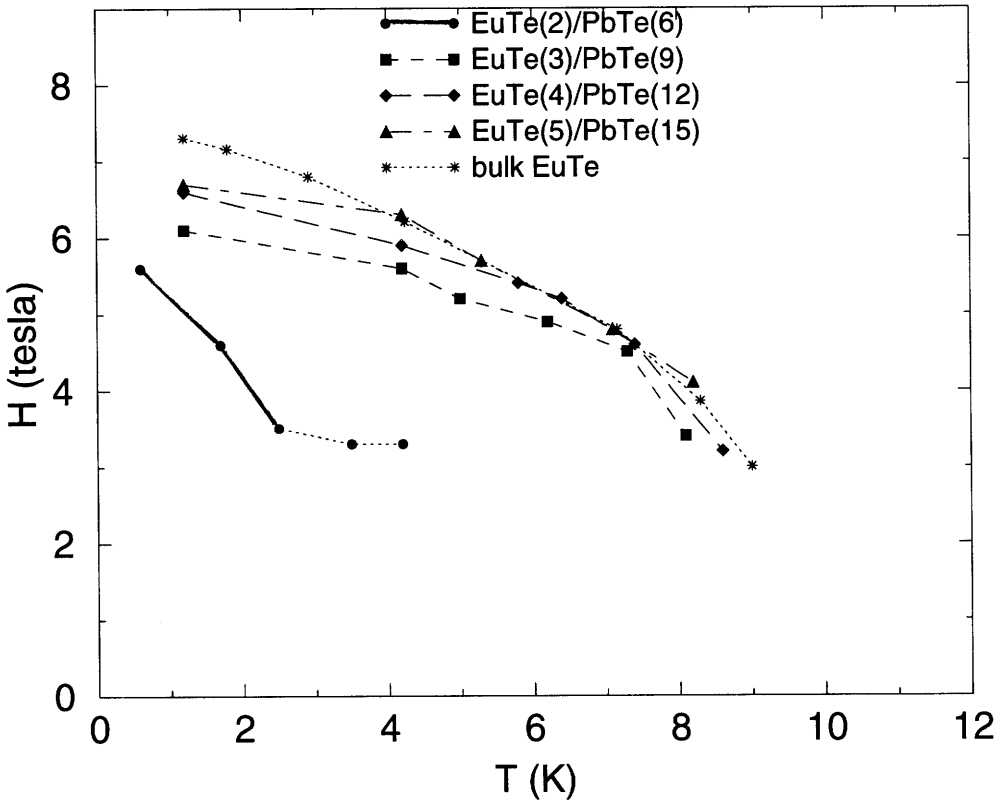

Figure 5-4: Canted AF (left side) to paramagnetic (right side) boundaries for EuTe/PbTe SLs and bulk EuTe. Values of T_c are given in Table 5.1.

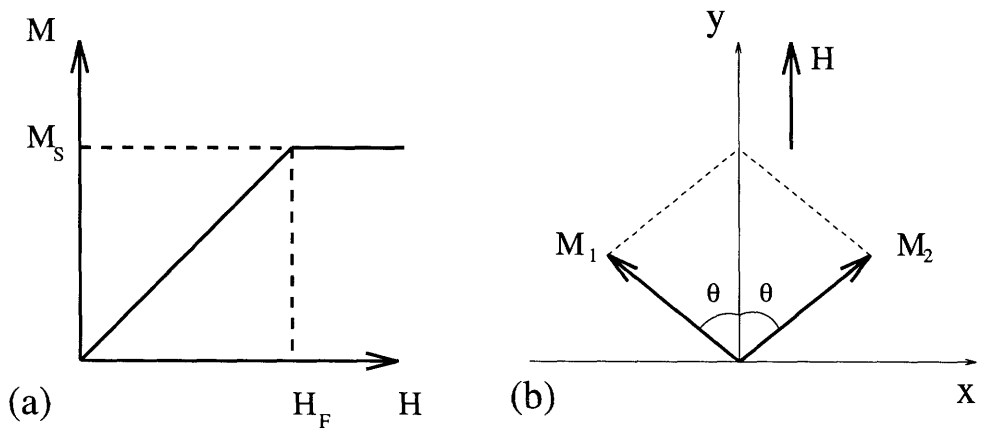

Figure 5-5: $M(H)$ curve of antiferromagnets where H_F is the field at the saturation value of the magnetization M_s (a). Directions of sublattice (adjacent (111) planes) magnetizations M_1 and M_2 with respect to H make an angle of θ with respect to the positive y direction (b).

Table 5.1: Experimental slopes of $M(H)$ for EuTe(ξ)/PbTe(η) SLs for various values of ξ

# of EuTe monolayers ξ	2	3	4	5	∞
T_c (K)	5.8	7.8	9.1	10.4	9.8
$\partial M/\partial H$ (emu/tesla gram)	24.0	21.5	20.4	20.4	15.5

Chapter 6

Zero Field Susceptibility

6.1 Introduction

Magnetic susceptibility reflects how the magnetization of a SL sample changes as we change the applied external field at fixed temperature. Zero field susceptibility (χ) refers to the changes in the sample's magnetization (M) as we change the applied external field (a small oscillating field h) under the condition that the external static field (H) is zero. Mathematically, the zero field susceptibility can be represented as $\chi = \left.\frac{\partial M}{\partial H}\right)_{H=0}$. The magnetic response from the samples is probed by sweeping the samples with a weak AC magnetic field, which is $\sim$4 gauss in our experiments for the SLs. The fluctuation-dissipation theorem shows that it is possible to probe the equilibrium fluctuations by applying a weak external field which couples to the spins in the system, but yet is too weak to affect the system. From these measurements we also can obtain the following information including the spin arrangement, magnetic ordering temperature, and correlation length as a function of temperature.

The zero field susceptibility is especially interesting in the magnetic studies of EuTe/PbTe SLs for the following reasons. In Chapter 3 we have shown from neutron diffraction experiments that the spins in EuTe/PbTe SLs below T_c arrange themselves ferromagnetically within the (111) planes and the spins in adjacent planes are aligned antiparallel to each other (type-II antiferromagnet). The static magnetization data show no detectable magnetic anisotropy within the (111) plane. Further, both

neutron diffraction and magnetization studies show that there is only one (111) magnetic domain in EuTe/PbTe SLs, and the magnetization of this domain is parallel to the SL plane, in contrast to bulk samples which have four equivalent orientations for their easy magnetization directions, and therefore exhibit multiple magnetic domains. Therefore, by carrying out susceptibility measurements both parallel and perpendicular to the SL plane, we are able to observe the process by which randomly pointed spins in the paramagnetic phase arrange themselves into a type-II antiferromagnetically ordered system. We emphasize here that such selection and control of the directions of the susceptibility measurements with respect to the spin alignment direction is rarely possible in bulk magnetic systems, as multi-magnetic domains inevitably form. Thus, EuTe/PbTe SLs offer a unique opportunity to observe the spin dynamics during the magnetic phase transition process.

6.2 Experimental Setup

For susceptiblility measurements we used an AC susceptometer made by Quantum Design (MPMS5). Details on the instrumentation are given in the Operation Manual,[60] and the essential features of an AC susceptometer are the same as those of a DC magnetometer given in Section 4.2, except that the AC susceptometer has a copper drive coil generating an oscillating magnetic field around the sample. The copper drive coil is situated between the superconducting pickup coil and the sample. We will in this section discuss the sample orientation and measurement conditions.

The SL samples are mounted in two different orientations for susceptibility measurements (see Fig.6-1). In the first configuration, the SL plane is parallel to the AC probing field h, as illustrated in the Fig.6-1(a). We denote the susceptibility obtained in this orientation as the in-plane susceptibility χ_{in}. In the second configuration the SL plane is perpendicular to the AC probing field h, as shown in the Fig.6-1(b). We denote the susceptibility measured in this orientation as the out-of-plane susceptibility χ_{out}.

The susceptibilities χ_{in} and χ_{out} are measured as a function of temperature from

15 K in the paramagnetic region to temperatures well below the transition temperatures (T_c) for all SL samples. The external field is kept at approximately zero (i.e., less than 2 gauss) during the susceptibility measurements. The effect of this small external remanent field is investigated by purposely applying an external field of 4 gauss during a susceptibility measurement and comparing the results at 4 gauss to the measurements taken in a nominal zero external field (i.e., 2 gauss). We find that the two sets of data overlap completely, thus eliminating the concern of small remanent field ($\sim$ 2 gauss) corrections to our susceptibility measurements (see Fig. 6-2). We will discuss the structure of the data shown in Fig. 6-2 in later sections. Finally, since we are measuring the samples with a very small AC field, we can safely ignore the diamagnetic contributions from the BaF_2 substrate and the PbTe buffer layer and nonmagnetic component of the SLs.

6.3 Frequency Dependence and Linearity

The frequency of the AC field used throughout our susceptibility studies is 20 Hz. We find that χ(f=20 Hz) = χ(f=0 Hz), so that we are actually measuring the static susceptibilities of our samples. To show this, we have measured χ_{in} for one of the SLs using different frequencies ranging from 0.1 Hz to 1 kHz (the upper limit of the susceptometer) and we found no detectable differences either in the amplitude or in the temperature dependence (see Fig.6-3). We chose to use 20 Hz for all susceptibility measurements because of the trade off between time in data acquisition and noise in the data quality. At a lower frequency we will get a better signal to noise ratio; however, it also takes a longer time to collect the data.

We can also vary the strength of the AC probing field h anywhere between 0 and 4 gauss. We would like to use the maximum amplitude of the probing field because of the very small amount of EuTe present in each SL sample. A typical size of the susceptibility at its peak value is about 5×10^{-6} emu with h= 4 gauss. To ensure that the susceptibilities obtained with h=4 gauss are still in the linear regime, we have measured χ_{in} for different h values and we have found that the results are

completely linear for h up to 4 gauss, as shown in Fig.6-4, where the $\chi_{in}(T)$ vs T data in Fig. 6-4(a) are normalized by the magnitude of the field in Fig. 6-4(b), for an EuTe(3)/PbTe(9) SL.

Thus, the experimental susceptibilities presented later in this Chapter are obtained in zero external static magnetic field, but with a 20 Hz AC field and with an AC probing field h=4 gauss.

6.4 Temperature Dependence of Susceptibility

We have performed susceptibility measurements for EuTe/PbTe SLs with ξ =1 to 7 as a function of temperature. The susceptibilities of SLs with $\xi \geq 2$ exhibit a rich temperature dependence. The number of Eu atoms per SL sample is determined by magnetization data in the paramagnetic regime, so that we can normalize the susceptibility data to the units of cm^3 per Eu atom and make quantitative comparisons among different SL samples. As we shall soon see, although there is continuous evolution in certain aspects of the susceptibility data as the superlattice period increases from SL EuTe(1)/PbTe(3) to SL EuTe(7)/PbTe(21), in many ways each SL sample has its own unique characteristic susceptibility, depending on the number ξ of EuTe layers. We shall start our discussion with the EuTe(1)/PbTe(3) SL and describe the data for each SL separately, in a sequential order from the SL with the smallest SL period to the SL with the largest SL period.

6.4.1 EuTe(1)/PbTe(3) SL

Nominally, the EuTe(1)/PbTe(3) SL has only a single monolayer of EuTe in each SL period. Unlike other SL samples, EuTe(1)/PbTe(3) has only nearest-neighbor ferromagnetic exchange coupling J_1, and the next-order term involves coupling to the next-nearest in-plane neighbor. The EuTe(1)/PbTe(3) SL would be an excellent system for studying the critical behavior for the 2D Heisenberg model if the ferromagnetic coupling J_1 were a little bit stronger. Presently we have the capability to measure χ down to 1.7 K, and the bulk ferromagnetic exchange coupling J_1 is ap-

proximately 0.04±0.01 K.[15] Mulitplying J_1 by 6 (the number of nearest neighbors) comes to 0.24 Kelvin which is still too low to be reached by our instrument. Figure.6-5(a) shows a plot of χ_{in} vs. T, and a straight-line like behavior is seen when the same data set are plotted as $\chi_{in}T^2$ vs. T (see Fig.6-5(b)). Thus, in the temperature range we have studied (1.7 K$<T<$ 20 K), the temperature-dependent susceptibility for the EuTe(1)/PbTe(3) SL exhibits Curie behavior, indicating that down to $T\sim$ 1.7 K, the monolayer EuTe/PbTe SL is in the paramagnetic phase.

For this sample χ_{out} is identical to χ_{in}, as they should be when the sample is in the paramagnetic state. So far no neutron diffraction experiments have been performed on a SL sample with ξ=1. On the basis of the magnetization and susceptibility data that we have taken, we conclude that the interesting temperature range for neutron scattering experiments would be below 1.8 K, which is the lowest temperature we have so far attempted in neutron scattering experiments for other SLs. An extrapolation on Fig.6-5(b) suggests a transition temperature of $\sim$ 1 K.

6.4.2 SL EuTe(2)/PbTe(6)

Starting with the EuTe(2)/PbTe(6) SL as ξ increases, the antiferromagnetic next-nearest-neighbor exchange coupling sets in. Specifically, for this SL there are three next-nearest Eu neighbors per Eu atom contributing to the J_2 exchange interactions in an EuTe(2)/PbTe(6) SL, exactly half as many as for an Eu atom in bulk EuTe. In Fig.6-6(a) χ_{in}(closed circles) and χ_{out}(open circles) are plotted against temperature. The results show that as T is decreased from 10 K, χ_{in} and χ_{out} separate from each other at T=8 K. As T decreases below 8 K, χ_{in} increases approximately four fold and reaches its maximum at T= 5 K, while χ_{out} increases only slightly and exhibits little temperature dependence. Clearly χ_{in} has a rather broad maximum and doesn't seem to imply a divergence. Thus we think that the maximum in χ_{in} doesn't correspond to an ordinary phase transition, e.g., from a paramagnetic to an antiferromagnetic phase. This conclusion is in agreement with neutron diffraction results, which suggest that antiferromagnetic ordering is not established until T= 1.8 K. Further, the broad maximum in χ_{in} at T= 5 K approximately coincides with the convergence temperature

5.8 K between ZFC and FC of the magnetization measurements. Thus, we think T=5 K most likely relates to the onset of substantial short-range order. As T is lowered further, χ_{in} and χ_{out} rejoin each other at T= 2 K, a phenomenon that is not seen in the other SLs to be discussed later.

In Fig. 6-6(b) we have plotted χT^2 vs. T for the same EuTe(2)/PbTe(6) SL. In this plot we have also included the in-plane paramagnetic susceptibility obtained by dividing the magnetization by the H field. The solid line represents the linear regression to the paramagnetic susceptibility. Notice that the fit intersects with $\chi_{out}(T)$ at T=8 K, exactly the temperature where χ_{in} and χ_{out} separate. This shows that as T is lowered, the Curie-Weiss behavior persists until reaching the temperature at which the susceptibilities become anisotropic.

6.4.3 SL EuTe(3)/PbTe(9)

The temperature dependence of χ_{in} and χ_{out} for an EuTe(3)/PbTe(9) SL is shown in Fig. 6-7(a). As T is reduced from the high temperature side, χ_{in} and χ_{out} coincide until a temperature of 9.1 K is reached, where χ_{in} and χ_{out} separate. Over the entire temperature range, χ_{out} exhibits a mild temperature dependence as T is further lowered. On the other hand, χ_{in} increases by a factor of 15 as T is lowered, and χ_{in} peaks at T = 7.9 K. The sharp peak in χ_{in} resembles the divergence of the susceptibility of a ferromagnet at the critical temperature. Thus we have identified the temperature at which χ_{in} reaches a maximum as the critical temperature (T_c).

In Fig. 6-7(b), χT^2 vs. T is plotted for χ_{in} and χ_{out}, with the addition of $\chi_{in}(T)$ data in the paramagnetic regime up to 60 K. This plot shows how the susceptibility data are normalized, and also indicates to us that as T is lowered until T=9.1 K, both χ_{in} and χ_{out} are Curie-Weiss like. Unlike the susceptibility behavior for the EuTe(2)/PbTe(6) SL, $\chi_{in}(T)$ and $\chi_{out}(T)$ for the EuTe(3)/PbTe(9) SL remain different at all temperatures below T_c.

6.4.4 SL EuTe(4)/PbTe(12)

The temperature dependence of χ_{in} and χ_{out} for an EuTe(4)/PbTe(12) SL is shown in Fig. 6-8(a), with χT^2 vs. T plotted in Fig. 6-8(b). The general temperature dependences of χ_{in} and χ_{out} for EuTe(4)/PbTe(12) SL are similar to those of the EuTe(3)/PbTe(9) SL. However, several differences are also observed. Firstly, the χ_{in} maximum is only 6.5 times the value of χ where χ_{in} and χ_{out} separate (T=10.3 K), compared to the factor of 15 increase for that of the EuTe(3)/PbTe(9) SL. Secondly, the $\chi_{in}(T)$ is less symmetric for the EuTe(4)/PbTe(12) SL than for the EuTe(3)/PbTe(9) SL, and the Full Width at Half Maximum (FWHM) linewidth for the ξ=4 SL is 0.7 K, while that for the EuTe(3)/PbTe(9) SL is 1.1 K. Finally, the T_c defined as the temperature at which the maximum χ_{in} occurs has moved up to 9.2 K.

6.4.5 SL EuTe(5)/PbTe(15)

The temperature dependence of $\chi_{in}(T)$ and $\chi_{out}(T)$ for an EuTe(5)/PbTe(15) SL is shown in Fig. 6-9(a), with χT^2 vs. T plotted in Fig. 6-9(b). As with the previous two samples, the $\chi_{in}(T)$ below T_c approaches a constant value, larger than the value of χ_{in} immediately above T_c. The maximum in χ_{in} continues to decrease with increasing ξ, and is smaller than that of an EuTe(4)/PbTe(12) SL. However, unlike the EuTe(2)/PbTe(6) SL, which has about the same magnitude for the maximum of $\chi_{in}(T)$ as that for the EuTe(5)/PbTe(15) SL, the maximum in χ_{in} for ξ=5 is rather sharp. The sharpness of the $\chi_{in}(T)$ peak can't be quantified in terms of the FWHM linewidth, because of the asymmetry between χ_{in} above and below T_c and because of the small peak value of $\chi_{in}(T)$.

The T_c for the EuTe(5)/PbTe(15) SL is found to be 10.45 K, the temperature at which χ_{in} reaches its maximum. The temperature below which the susceptibility becomes anisotropic is 11.3 K, and above that temperature both χ_{in} and χ_{out} exhibit Curie-Weiss behavior, as shown in Fig. 6-9(b).

6.4.6 SL EuTe(6)/PbTe(18)

As for the previous three SLs, χ_{in} and χ_{out} for an EuTe(6)/PbTe(18) SL overlap and have a Curie-Weiss like temperature dependence above T = 11.8 K, below which the susceptibility starts to become anisotropic (see Fig. 6-10(a-b)). The $\chi_{in}(T)$ curve peaks at T =11.0 K with an even smaller value for the maximum susceptibility compared to that of an EuTe(5)/PbTe(15) SL. Further, both χ_{in} and χ_{out} for the EuTe(6)/PbTe(18) SL have distinct features that are different from the temperature dependence of the other SLs described above (see Fig. 6-10(a)). The $\chi_{out}(T)$ decreases precipitously starting from T = 7.5 K and reaches close to zero at T= 5.1 K, a drop of 1×10^{-24} cm^3 per Eu atom in the magnitude of the susceptibility. In the same temperature interval, $\chi_{in}(T)$ also shows a dip of 33% in value, or 6×10^{-25} cm^3 per Eu atom in the magnitude of the susceptibility, approximately half as much as the total decrease in the χ_{out}. The corresponding shift observed in χ_{in} implies that our measurement of χ_{out} is likely to be reliable.

Although the χ_{out} data for this SL is reproducible, the EuTe(6)/PbTe(18) SL is the only SL that exhibits this peculiar behavior. This feature is certainly interesting and equally perplexing. We haven't yet found an explanation for this effect. We focus our attention toward explaining other features that are more universal and common to all SLs.

6.4.7 SL EuTe(7)/PbTe(21)

Figure 6-11(a-b) shows the temperature dependence of $\chi_{in}(T)$ and $\chi_{out}(T)$ for an EuTe(7)/PbTe(21) SL. The temperature dependences of both $\chi_{in}(T)$ and $\chi_{out}(T)$ are similar to those of EuTe(3)/PbTe(9) and EuTe(5)/PbTe(15) SLs. The T_c for the EuTe(7)/PbTe(21) SL has increased to 11.45 K, and the onset of the susceptibility anisotropy is at T= 12.1 K. These temperatures are summarized in Table 6.1 for all the SL samples (ξ=1,...,7).

6.5 Discussion

In section 6.4 we have described the temperature-dependent susceptibility data for seven different SLs. Specifically, we have shown $\chi_{in}(T)$ and $\chi_{out}(T)$ data for each SL. In this section, we will give a qualitative explanation of the important features observed in the experimental zero field susceptibility data.

6.5.1 Anisotropy in the Susceptibility

The most prominent feature common to the SLs with $\xi \geq 3$ is the anisotropic behavior between χ_{in} and χ_{out} at low temperatures. SLs with $\xi \geq 3$ form a special class because they exhibit the paramagnetic to antiferromagnetic phase transition in the temperature region $T >$ 1.8 K, as verified by neutron diffraction experiments.[38] The anisotropic susceptibility behavior that we observe is likely due to dipole-dipole interactions. The exchange couplings J_1 and J_2 favor spins residing on the same (111) plane to form ferromagnetically-ordered domains, while the spins on the adjacent (111) planes align in antiparallel directions. However, the exchange couplings don't fix any unique direction for the ferromagnetic order, whereas the dipole-dipole interaction selects the (111) plane for the ferromagnetic order, i.e., if spins lie in the (111) planes they would have a lower dipole-dipole interaction energy compared to the case where the spins stand perpendicular to the (111) planes. Within the (111) planes, the dipole-dipole interaction doesn't favor any specific direction, in good agreement with the static magnetization studies which indicate no magnetic anisotropy within the (111) planes.[61]

The anisotropic behavior in the susceptibility shows up both above and below T_c. We identify the maximum in $\chi_{in}(T)$ as the transition temperature T_c because it resembles the divergence in the susceptibility. The temperature window above T_c where the susceptibility is anisotropic, is well defined. The lower bound for this window is the T_c itself, and the upper bound is the temperature denoted by T_s where $\chi_{in}(T)$ first separates from $\chi_{out}(T)$. In Fig. 6-12 we plot T_s - T_c versus the SL period thicknesses. The results of Fig.6-12 show that the temperature window T_s - T_c shrinks

as the SL period thickness increases and eventually as $\xi \longrightarrow \infty$, T_s-$T_c \longrightarrow 0$ the bulk sample limit. In bulk layered 2D antiferromagnets, the anisotropy in the susceptibility is commonly observed in a small (much smaller than what we have seen in the SLs) region above T_c,[7] and this anisotropy is due to the substantial short-range order that is present above T_c. In our case, the presence of the T_s-T_c temperature window may be interpreted to imply that the long-range order is induced by the dipole interactions. When the temperature for our SLs reaches T_s the spins start to go into the (111) planes as a result of dipole interactions. However, the magnetic long-range order does not form until a lower temperature T_c is reached. In contrast, in bulk EuTe, the long-range order and the spins going into the (111) planes all take place at the same transition temperature.

The anisotropy in the susceptibility below T_c can be understood in terms of $\chi_{\parallel}(T)$ and $\chi_{\perp}(T)$. Below T_c the spins lie in the (111) planes and exhibit ferromagnetic ordering, while spins on the adjacent (111) planes are aligned antiparallel.[38] Further, within the (111) planes there is no detectable magnetic anisotropy.[61] Therefore, assuming that the magnetic domains within the (111) planes are randomly oriented, then the measured χ_{in} should be approximately $\frac{1}{2}(\chi_{\parallel} + \chi_{\perp})$, where $\chi_{\parallel}$ and $\chi_{\perp}$ denote the parallel and perpendicular components of the susceptibility. The χ_{out} is larger than $\chi_{\perp}$ by an amount due to the dipole-dipole interaction energy. At T=0 K, $\chi_{\parallel}$= 0 and $\chi_{\perp} \sim 1/\mu$, where μ is the exchange energy per Eu atom.[62] In Fig. 6-13 the extrapolated $\chi_{in}(T = 0)$ and $\chi_{out}(T = 0)$ limits for each SL sample are plotted versus ξ the EuTe thickness per SL period. The decreasing trend for $\chi_{in}(T = 0)$ as the EuTe thickness increases agrees with the approximation given in the Ref.[62]. However, upon comparison with the bulk $\chi_{\perp}(T)$ value, the data suggest that $\chi_{in}(T)$ approaches the $\chi_{\perp}(T)$ value instead of $\frac{1}{2}$ $\chi_{\perp}$ as T goes to 0 K. On the other hand, we conclude that χ_{out} lies consistently below χ_{in} because of the extra dipole-dipole interaction energy.

6.5.2 Divergent χ_{in} and T_c

The second important feature common to the SLs with $\xi \geq 3$ is the appearance of sharp peaks in the χ_{in} measurements. These sharp peaks in the χ_{in} data, regardless of whether ξ is even or odd, are consequences of uncompensated spins in the SLs. It is easy to understand that the SL samples with ξ =odd will have many uncompensated spins. However, it is also possible for SLs with nominal ξ= even to have uncompensated spins because of SL imperfections, such as monolayer steps at the EuTe and PbTe interfaces. Further, the maximum value of χ_{in} decreases as the EuTe thickness per SL period increases. This trend, shown graphically in Fig.6-14, is expected to converge to the bulk EuTe antiferromagnet limit, where there is no peak at all in $\chi_{in}(T)$. However, the relationship between the maximum χ_{in} and ξ most likely is not linear, and for this reason we cannot, obtain the correct bulk χ_{in} maximum value by extrapolating the plot of χ_{in} maximum vs. $1/\xi$ to $1/\xi \longrightarrow 0$.

We have identified the temperature at which the maximum of χ_{in} occurs as the transition temperature $T_{c,\chi}$. In Table 6.1 the values of $T_{c,\chi}$ so determined for each SL for $\xi \geq 3$ are tabulated. There is a consistent trend of increasing $T_{c,\chi}$ as the EuTe thickness per SL period increases. In addition, the $T_{c,\chi}$ values obtained by the susceptibility data agree well with the $T_{c,M}$ values previously obtained from ZFC and FC magnetization measurements (see second row of Table 6.1). In Fig.6-15 the dependence of T_c on the EuTe layer thickness ξ is plotted. Clearly some SLs have T_c values greater than that of bulk EuTe, indicating changes in the J_1 and J_2 magnetic coupling values taking place in our SLs. In Chapter 7 we discuss likely changes in the J_1 and J_2 values on the basis of Monte Carlo simulations.

6.6 Summary

We have measured the zero field susceptibility for SLs with ξ=1 to ξ=7 in two different orientations, parallel to the SL plane (χ_{in}) and perpendicular to the SL plane (χ_{out}). The data for the EuTe(1)/PbTe(3) SL shows no phase transition at all in the $T > 1.8$ K temperature region, in agreement with the static magnetization results presented in

Chapter 4. The EuTe(2)/PbTe(6) SL shows an anisotropic susceptibility from T= 8 K to T = 1.8 K with a very broad peak in χ_{in}, suggesting substantial short-range order in that temperature window, but no real long-range order, consistent with neutron scattering measurements. SLs with $\xi \geq 3$, however have anisotropic susceptibilities accompanied by sharp peaks in the χ_{in} data. The narrow peaks of χ_{in} resemble the divergent susceptibility of a ferromagnet at the transition temperature. We have attributed the peaks observed in χ_{in} to the uncompensated ferromagnetically ordered spins in the SLs, also identifying the positions of those peaks with the magnetic transition temperatures. The strong anisotropy in the susceptibility data strikes us as the most important feature in these experimental results, because the exchange couplings are isotropic in bulk EuTe and the localized spins in EuTe have zero orbital angular momentum. Thus we are led to believe that the dipole-dipole interaction is the leading cause for the anisotropic behavior in the susceptibility. Furthermore, the dipole-dipole interaction is also believed to be the factor that stabilizes the magnetic long-range order at $T > 0$ K in the EuTe/PbTe SLs, a system of 2D Heisenberg magnets, which otherwise would not have long-range order until $T = 0$ K is reached. In the next chapter we use Monte Carlo simulations to quantitatively address issues such as the sharp peaks in χ_{in} and the anisotropic behavior in the susceptibility.

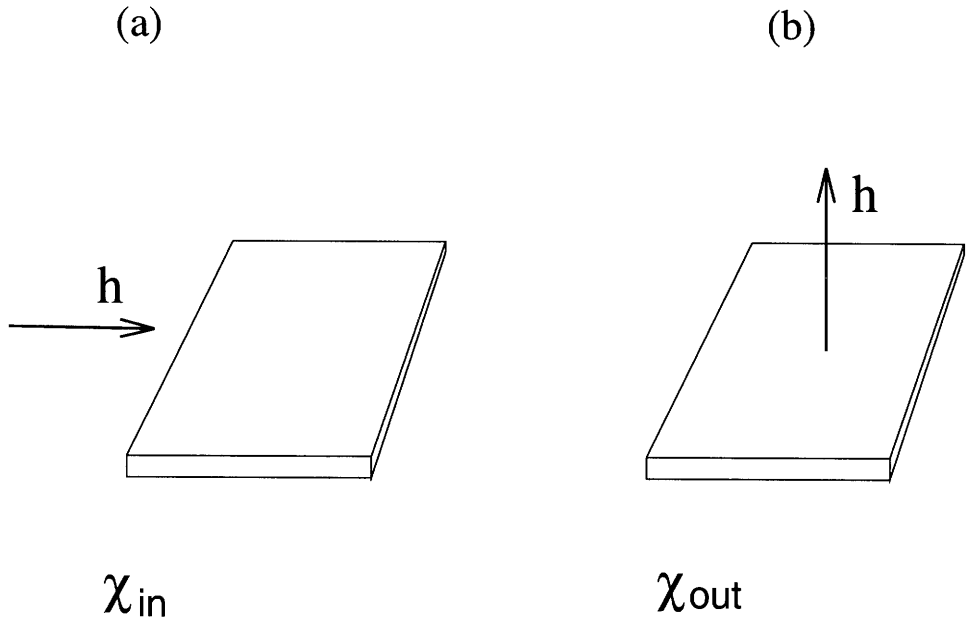

Figure 6-1: The two principal orientations of the sample with respect to the AC probing field for the χ_{in} (a), and χ_{out} (b) susceptibility measurements.

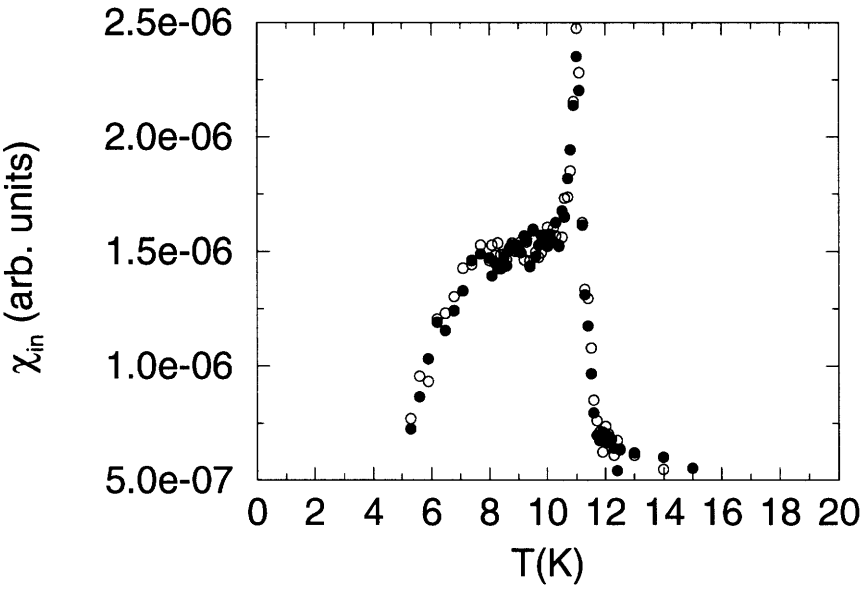

Figure 6-2: χ_{in} for an EuTe(6)/PbTe(18) SL measured with a 20 Hz AC magnetic field of h=4 gauss and a static external magnetic field of H=4 gauss (closed circles); χ_{in} for the same sample but measured with a 20 Hz AC field of h=4 gauss and zero nominal static external field (open circles). The nominal zero field is estimated to correspond to a $H \simeq 2$ gauss. The notation e-06 denotes 10^{-6}.

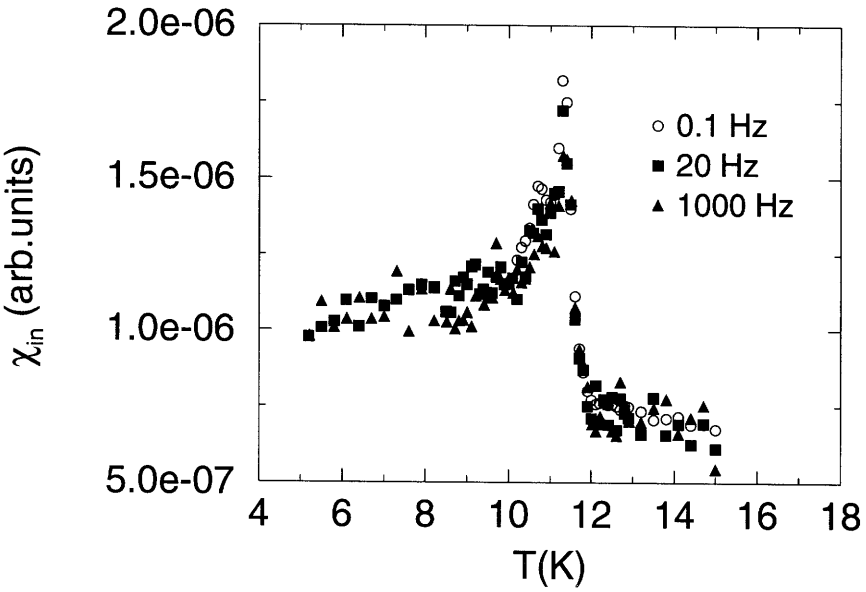

Figure 6-3: Temperature dependence of the χ_{in} for an EuTe(7)/PbTe(21) SL sample measured with h= 4 gauss and zero external field at 0.1 Hz, 20 Hz and 1000 Hz. The notation e-06 denotes 10^{-6}.

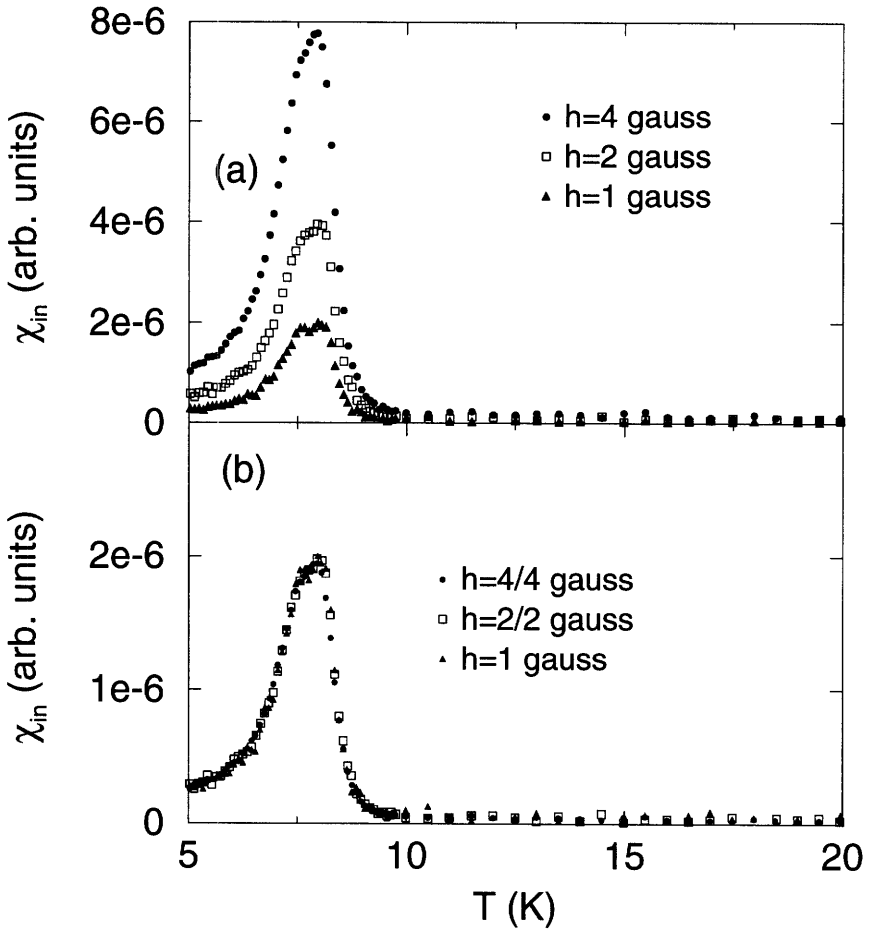

Figure 6-4: Temperature dependence of χ_{in} for an EuTe(3)/PbTe(9) SL measured at three different AC fields) (a); the same data as in (a) but the data χ_{in} are normalized to the size of the AC field h= 1 gauss for the same EuTe(3)/PbTe(9) SL (b). The notation e-06 denotes 10^{-6}.

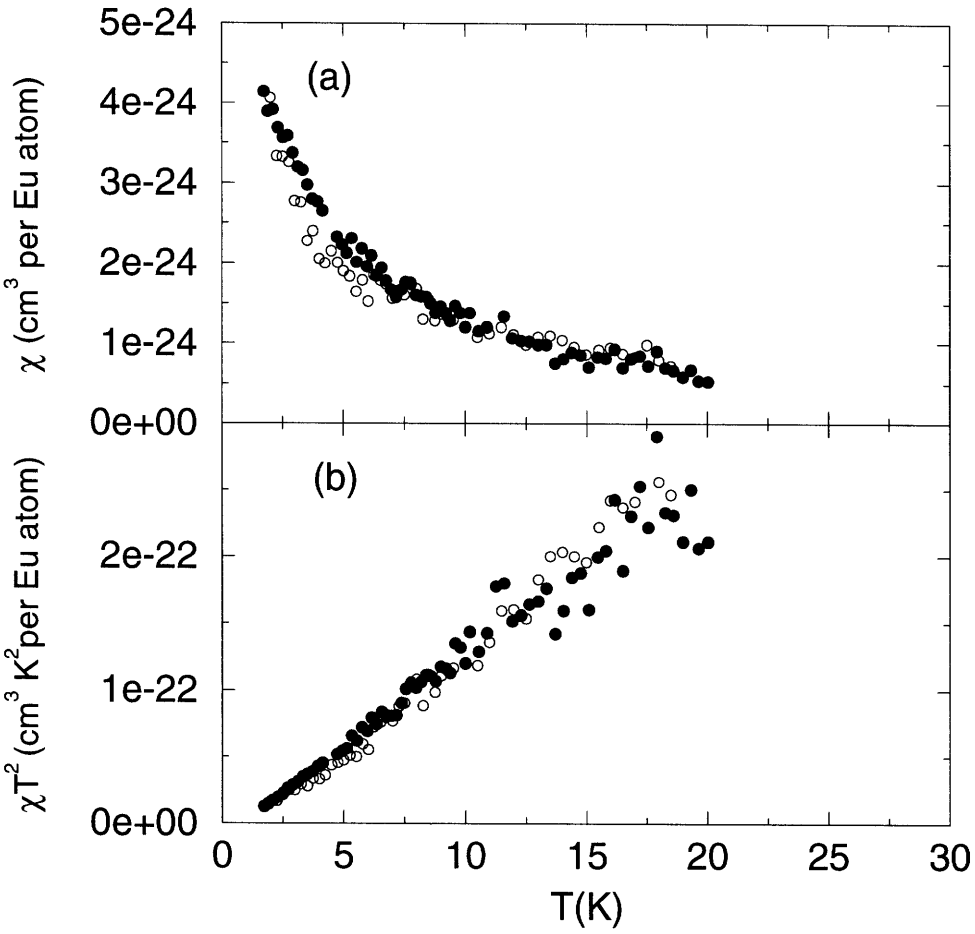

Figure 6-5: Normalized χ_{in} vs.T (closed circles) and χ_{out} vs. T (open circles) (a), and $\chi_{in}T^2$ vs. T (closed circles) and $\chi_{out}T^2$ vs. T (open circles) (b) for an EuTe(1)/PbTe(3) SL measured at a probing field of h=4 gauss and f=20 Hz. The notation e-06 denotes 10^{-6}.

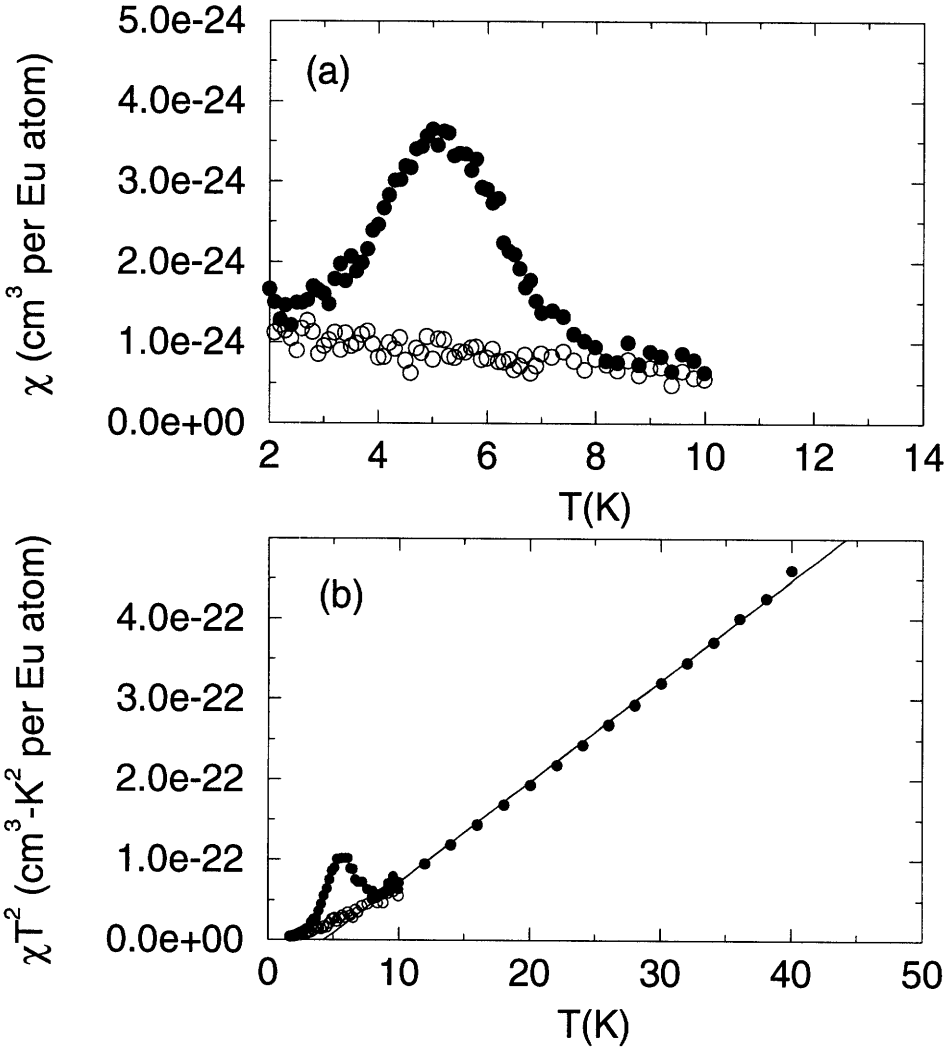

Figure 6-6: Normalized χ_{in} vs. T (closed circles) and χ_{out} vs. T (open circles) for an EuTe(2)/PbTe(6) SL; the same set of data plotted as χT^2 vs. T including data for χ_{in} in the paramagnetic phase up to 40 K(b). The notation e-24 denotes 10^{-24}.

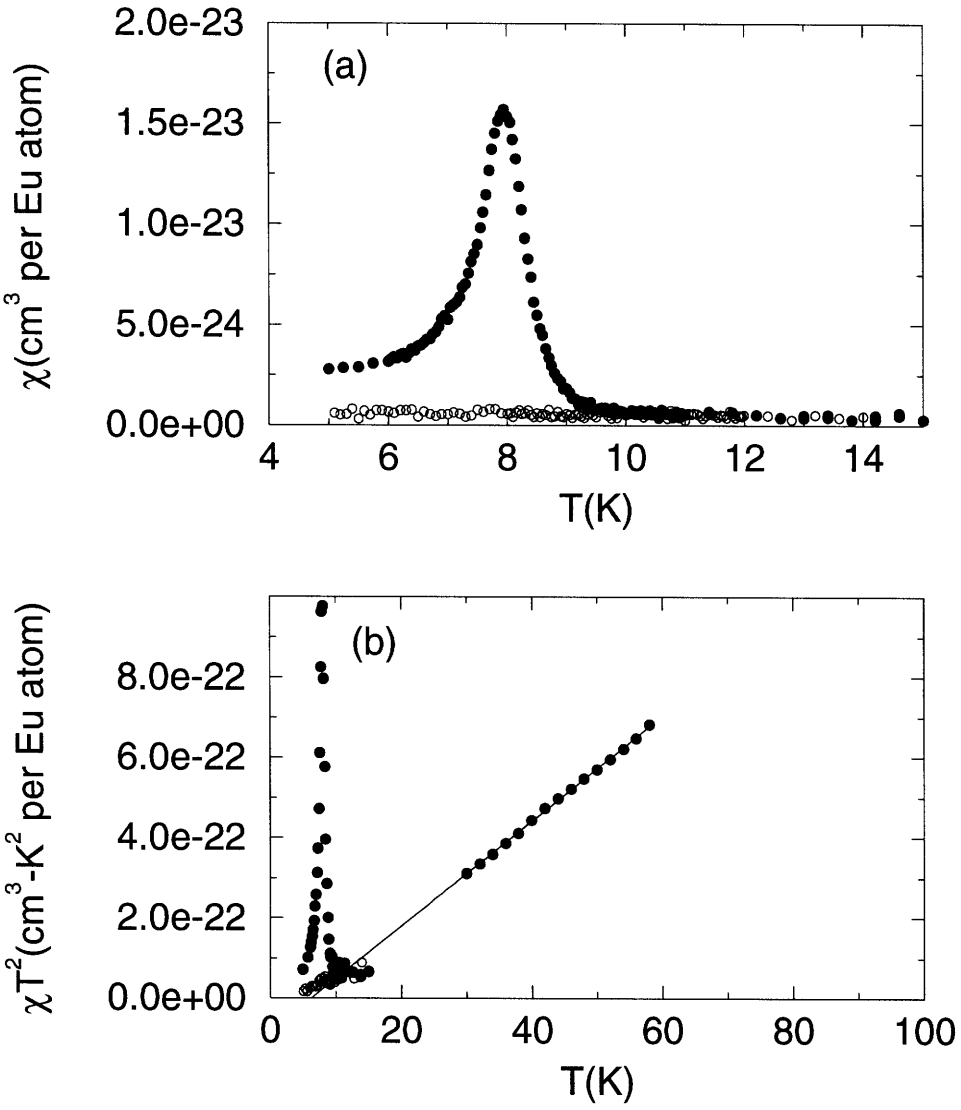

Figure 6-7: Normalized χ_{in} vs. T (closed circles) and χ_{out} vs. T (open circles) for an EuTe(3)/PbTe(9) SL (a); the same set of data as in (a) plotted as χT^2 vs. T with data for χ_{in} up to 60 K in the paramagnetic phase included (b). The solid line in (b) represents the Curie-Weiss paramagnetic susceptibility. The notation e-24 denotes 10^{-24}.

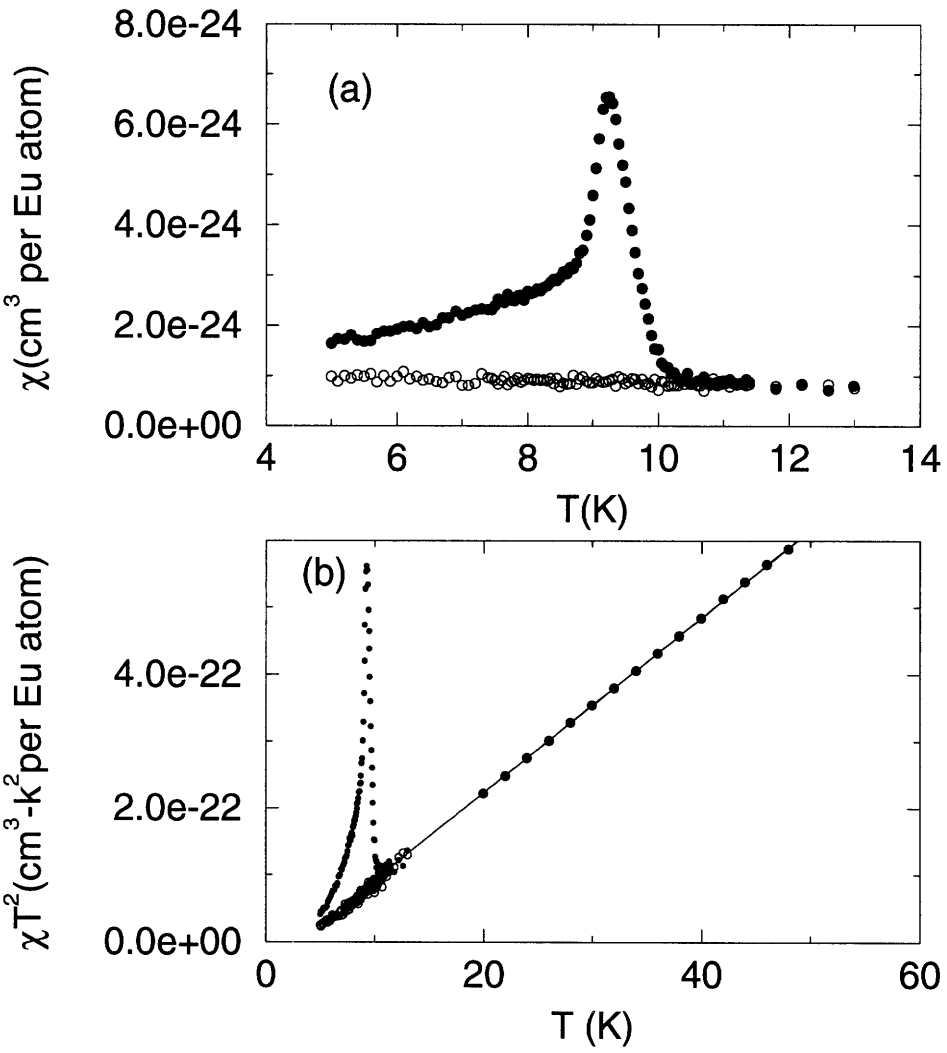

Figure 6-8: (a) Normalized χ_{in} vs. T (closed circles) and χ_{out} vs. T (open circles) for an EuTe(4)/PbTe(12) SL; (b) same set of data as in (a) plotted as χT^2 vs. T with the data for χ_{in} in the paramagnetic phase up to 50 K included in (b). The notation e-24 represents 10^{-24}.

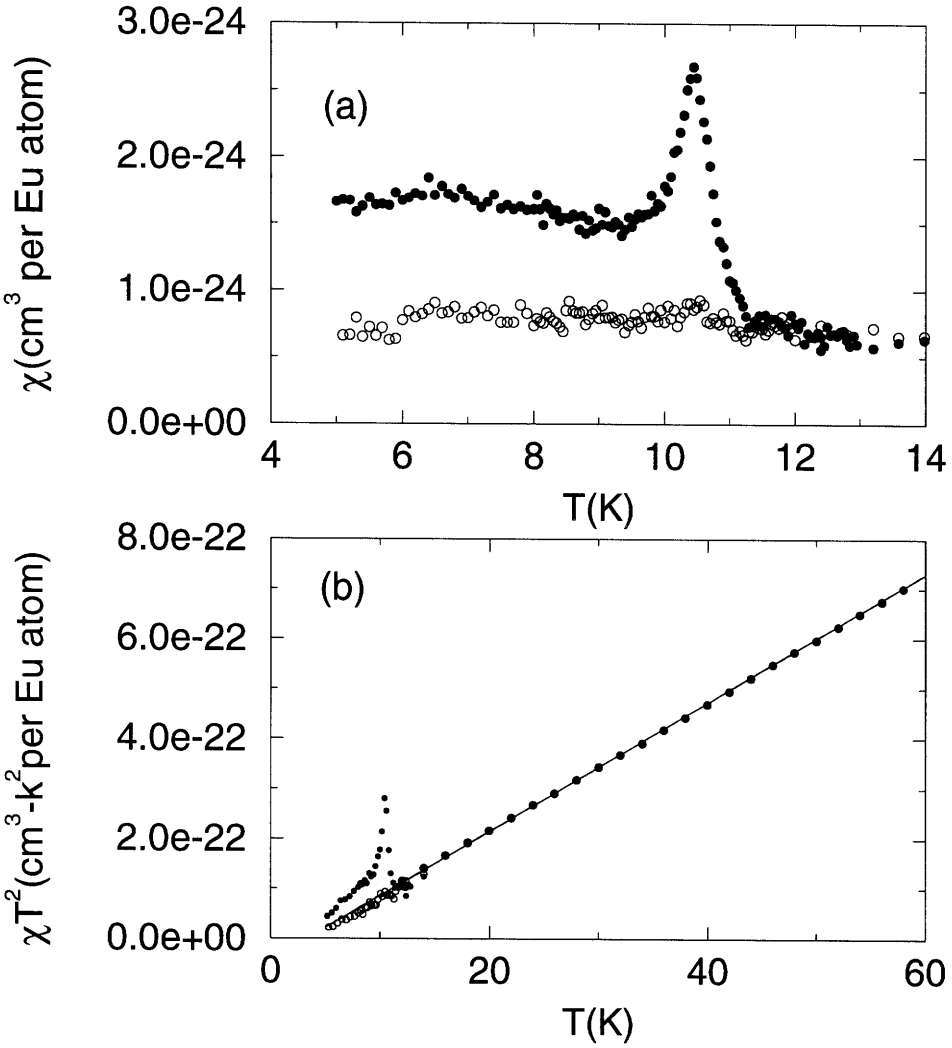

Figure 6-9: (a) Normalized χ_{in} vs. T (closed circles) and χ_{out} vs. T (open circles) for an EuTe(5)/PbTe(15) SL; (b) the same set of data as in (a) is plotted as χT^2 vs. T with the data for $\chi_{in}(T)$ in the paramagnetic phase below 60 K included in (b). The notation e-24 represents 10^{-24}.

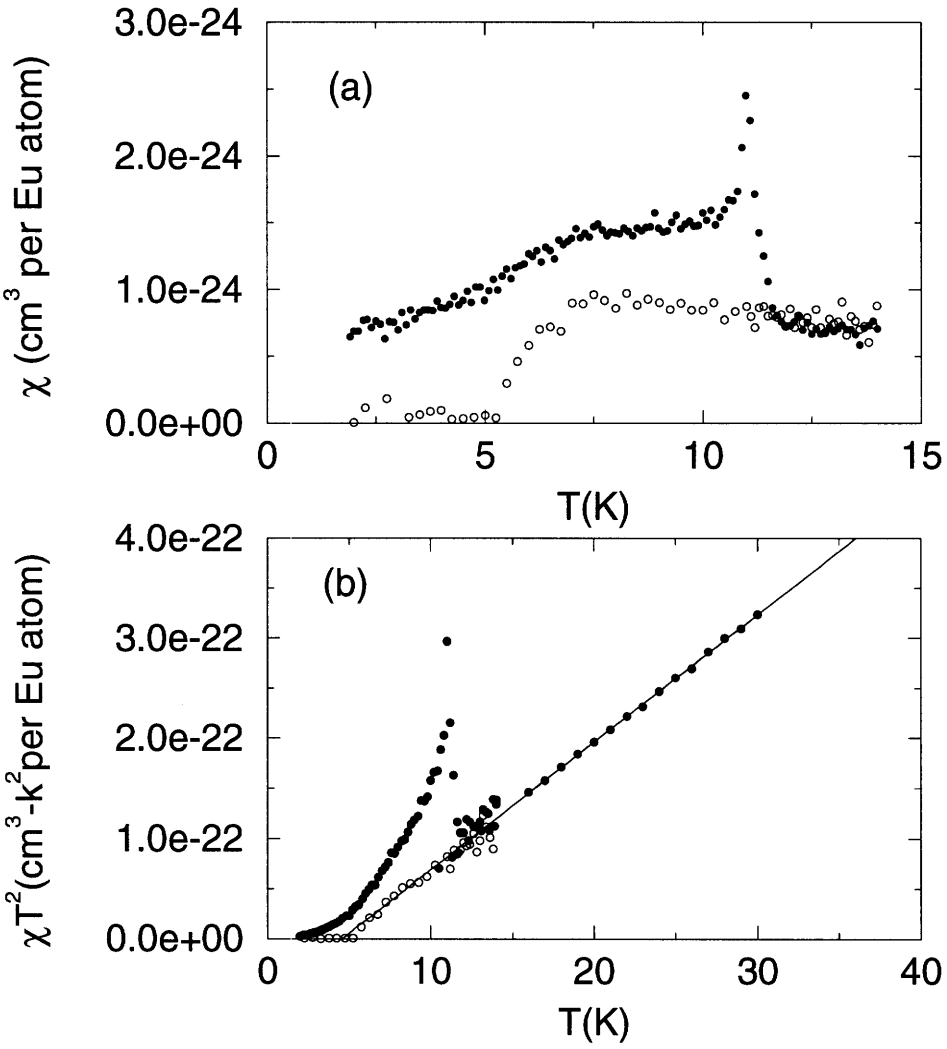

Figure 6-10: (a) Normalized plot of χ_{in} vs. T (closed circles) and χ_{out} vs. T (open circles) for an EuTe(6)/PbTe(18) SL; (b) the same set of data as in (a) plotted as χT^2 vs. T, with the data for $\chi_{in}(T)$ in the paramagnetic phase up to 30 K included in (b). The notation e-24 represents 10^{-24}.

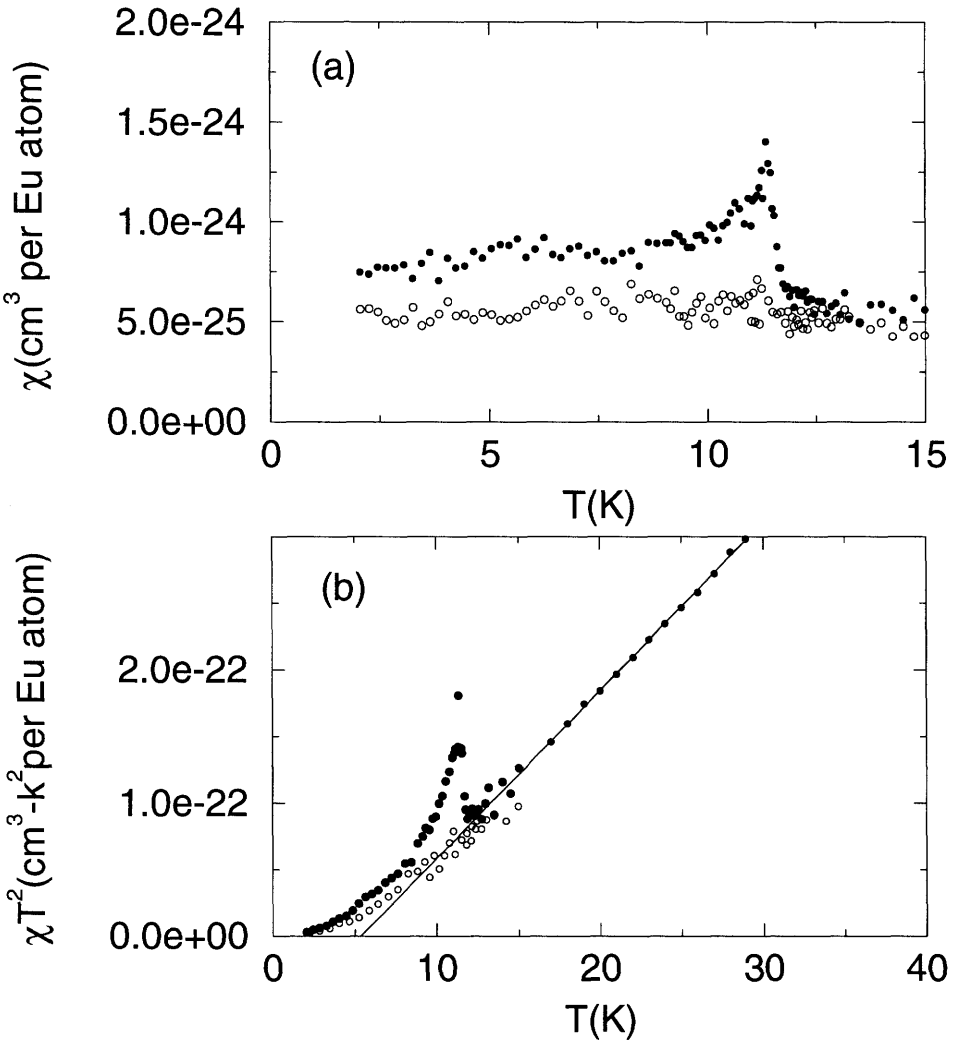

Figure 6-11: (a) Normalized plot of χ_{in} vs. T (closed circles) and χ_{out} vs. T (open circles) for an EuTe(7)/PbTe(21) SL; (b) the same set of data as in (a) plotted as χT^2 vs. T, with the data for χ_{in} in the paramagnetic phase below 30 K included in (b). The notation e-24 represents 10^{-24}.

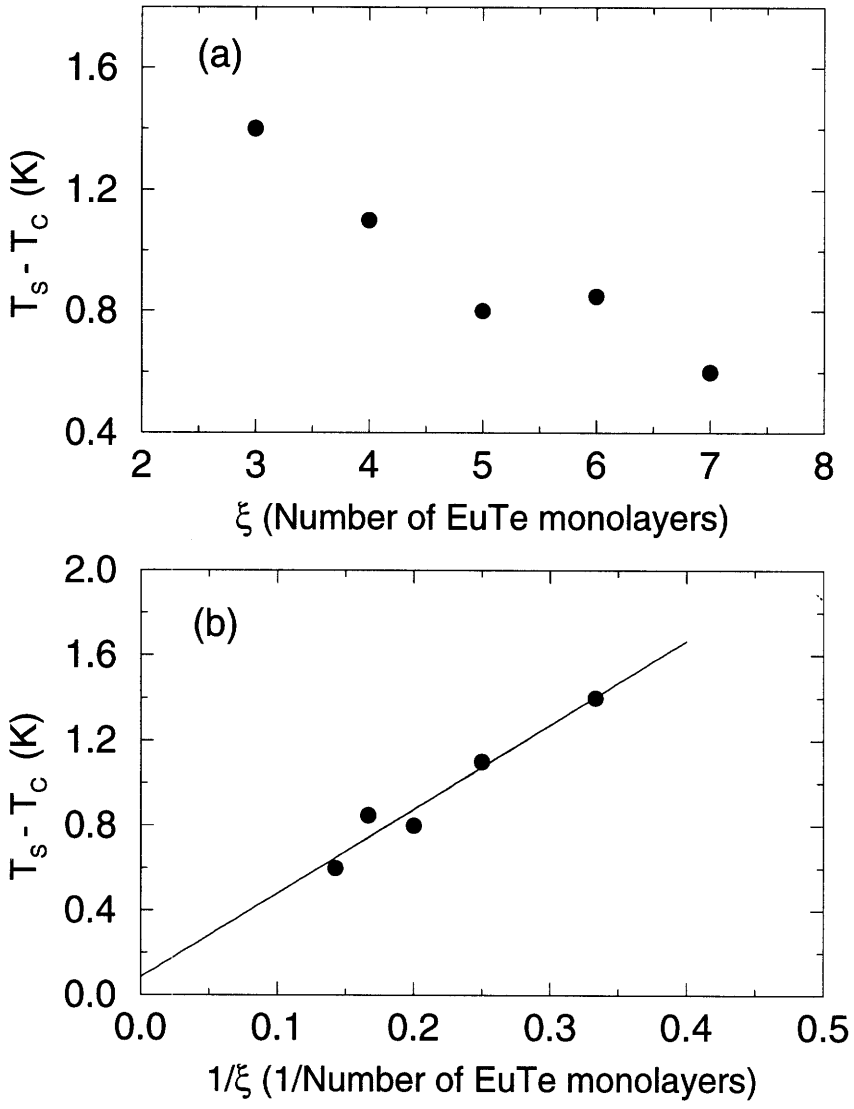

Figure 6-12: The temperature window above T_c defined by T_s - T_c where T_s is the temperature below which anisotropy in the susceptibility is first observed (a); the same set of T_s - T_c data plotted vs. $1/\xi$ (b).

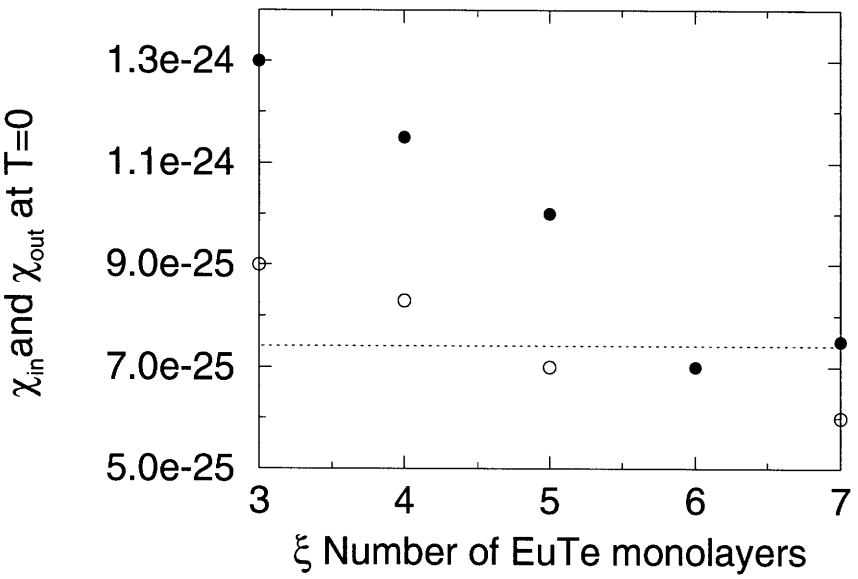

Figure 6-13: Values of χ_{in} (closed circles) and χ_{out} (open) circles extrapolated to $T = 0$ K versus ξ, the EuTe thickness per SL period. The dotted line represents the value of the perpendicular component $\chi_{\perp}$ of the susceptibility at $T = 0$ K for a bulk EuTe sample. The χ_{out} value for the EuTe(6)/PbTe(18) is zero at 0 K which is not shown here because it would increase the range of the vertical scale.

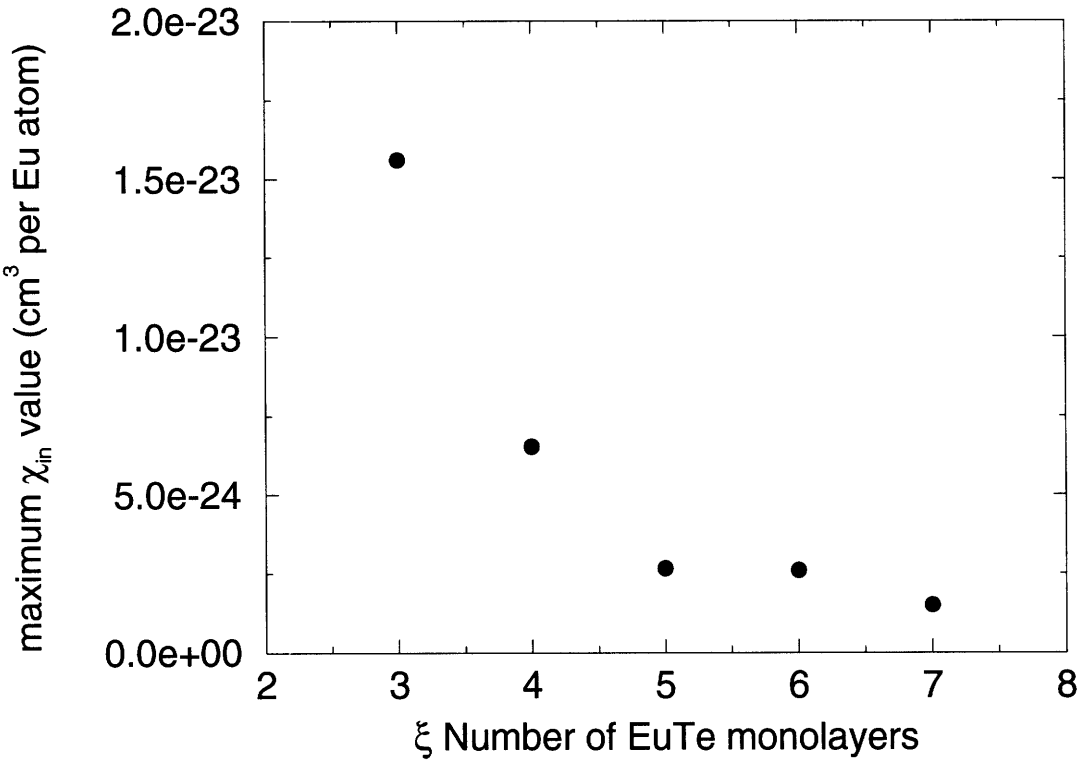

Figure 6-14: The maximum value of χ_{in} vs. the EuTe layer thickness ξ.

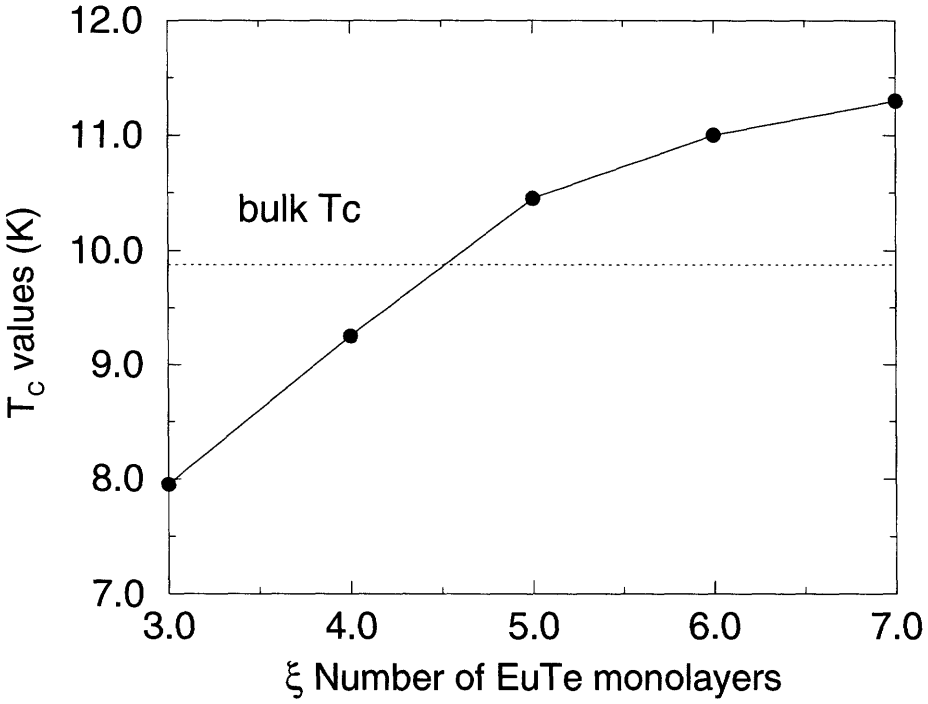

Figure 6-15: The transition temperature T_c vs. the EuTe layer thickness ξ.

Table 6.1: Magnetic transition temperatures T_c for SLs obtained from the peak position of χ_{in} (first row $T_{c,\chi}$), compared to the $T_{c,M}$ values previously determined from ZFC and FC measurements of $M(T)$ (second row). T_s values, the temperatures below which anisotropy in the susceptibility is first observed are given in the third row.

sample(ξ/η)	/3/9	4/12	5/15	6/18	7/21	bulk EuTe
$T_{c,\chi}$(K)	7.9	9.2	10.45	11.0	11.45	9.8
$T_{c,M}$(K)	7.8	9.1	10.4	11.2	11.2	9.8
T_s(K)	9.1	10.3	11.3	11.8	12.1	-

Chapter 7

Monte Carlo Simulation

7.1 Introduction

Anisotropy in the susceptibility and the divergent behavior in χ_{in} observed in SLs with $\xi \geq 3$ (referring to the SL notation EuTe(ξ)/PbTe(η)) are two primary features that we address more quantitatively in this Chapter. More importantly, the anisotropic susceptibility data presented in Chapter 6 led us to suspect that weak dipolar forces play an important role in the emergence of antiferromagnetic long-range order in EuTe/PbTe SLs. However, direct analytical approaches for calculating the susceptibility do not readily apply because of the finite thickness of SLs. To this end, we have turned our focus to Monte Carlo simulations with the hope of describing quantitatively the susceptibility behavior of EuTe/PbTe SLs via simulation techniques.

To illustrate the complexity of the computation for the susceptibility, let us examine the partition function Z for SLs:

$$Z = \sum_{\mu} e^{-\beta \mathcal{H}} \tag{7.1}$$

where μ denotes all microstates, β is the inverse thermal energy $k_B T$, and $\mathcal{H}$ is the magnetic Hamiltonian expressed as

$$\mathcal{H} = -J_1 \sum_{nn} \vec{S}_i \cdot \vec{S}_j - J_2 \sum_{nnn} \vec{S}_i \cdot \vec{S}_j \tag{7.2}$$

where nn and nnn denote the nearest and next-nearest-neighbor spin pairs, and J_1, J_2 are the corresponding exchange couplings. The spins S_i and S_j are restricted to a few consecutive (111) planes as in a SL structure. Clearly, there is no simple way to treat the partition function analytically, and numerical approaches were therefore tried.

In this chapter we present the results of Monte Carlo simulations tailored to the EuTe/PbTe SL structure, using three different 2D magnetic models. They are: (1) the Ising model, (2) the Clock model with 6-fold symmetry, and (3) the Heisenberg model with dipolar couplings. Our goals are to quantitatively explain: (1) the divergent behavior in χ_{in}, (2) the anisotropy between χ_{in} and χ_{out}, and (3) the mechanism that stabilizes the long-range antiferromagnetic order in the EuTe/PbTe SLs. The Ising model addresses the first goal, while the Heisenberg model with dipolar couplings meets the second and third goals. Finally, the Clock model with 6-fold symmetry complements the Ising model and the Heisenberg model with dipolar couplings by addressing two specific computational technicalities, as discussed below.

The Monte Carlo simulations we have run are classical Monte Carlo simulations. That is, we treat the spin operators as classical vectors. M. E. Fisher has given an argument that in the limit $S \longrightarrow \infty$, the quantum spin operator is same as the corresponding classical vector.[63] The S value for EuTe is 7/2, which is a large spin value, such that a classical Monte Carlo simulation would be expected to work quite well. Also in our calculations, we have assumed that the inter-period magnetic coupling is dominated by the dipole-dipole interaction, and is effectively zero from an estimation using the formalism developed in Ref. [8]. We have followed the standard practice for carrying out Monte Carlo studies, including descriptions of the parameters of the calculation, descriptions of the computer program, estimates of statistical error, and comparisons with previous relevant Monte Carlo investigations.

7.2 Monte Carlo Method

Our approaches follows the conceptual foundations of Monte Carlo simulations described in the monograph by A. D. Sokal,[64] and here we briefly summarize the key concepts embedded in a Monte Carlo simulation.[64]

Broadly speaking, Monte Carlo simulations have two major applications, numerical integration (i.e., static Monte Carlo simulation) and ensemble averages of certain distributions (i.e., dynamic Monte Carlo simulation). In statistical physics we are interested in the latter application. The idea of a dynamic Monte Carlo method is to create a stochastic process within configuration space Ω (in our case it is the set of all spin configurations) having the Boltzmann distribution as its equilibrium distribution. The stochastic process is generated by computer and is always taken to be a Markov process. A Markov process is a sequence of random variables X_0 X_1 X_2 ... such that successive transitions from X_t to X_{t+1} are statistically independent. To generate configurations from the Boltzmann distribution (π), it suffices to introduce a transition probability matrix $P{=}p_{xy}{=}p(x \longrightarrow y)$ satisfying:

(1) Irreducibility: if x and y belong to the configuration space Ω, with $n \geq 0$, then $p_{xy}^{(n)}{>}0$, where n denotes the number of Monte Carlo steps.

(2) Stationarity of the distribution π: if y belongs to Ω, then if follows that $\sum_x \pi_x p_{xy} = \pi_y$.

7.3 Metropolis Algorithm

The computer programs for the Ising model and the Clock model with 6-fold symmetry are based on the Metropolis algorithm.[65] The Metropolis algorithm satisfies the two criteria prescribed in Section 7.2. To describe the Metropolis algorithm in detail, we use the Ising model as an example. For Ising simulations, we start out in the high temperature region with $T{>}T_c$, with a random configuration for the spins S (the so called hot start), i.e., some S are $+1$ and some are -1 (we have used spin 1 for all simulations, but when the final results are normalized to spin 7/2 before they

are plotted) and total sum of all S is approximately zero ($M=\sum_i^N S_i \simeq 0$, where N is the total number of spins on the lattice). According to the Metropolis algorithm, each Monte Carlo step consists of the following substeps:

a. Choose a spin S_i.

b. Flip it to $-S_i$.

c. Calculate the energy change ΔE according to the Hamiltonian.

d. If ΔE is negative, the spin assumes the new orientation (after flipping). If ΔE is positive, then calculate $e^{-\Delta E/k_B T}$.

e. Generate a random number (RN) between 0 and 1, and compare it to $e^{-\Delta E/k_B T}$.

If $e^{-\Delta E/k_B T} > RN$, the spin assumes the new orientation (after flipping).

If, however, $e^{-\Delta E/k_B T} < RN$, the spin keeps the original orientation (before flipping).

f. The magnetization is found from $M=\sum_i^N S_i$, where N is the total number of spins on the lattice.

g. Normalize the calculated magnetization ($M=\sum_i^N S_i$) to units of emu per Eu atom-gauss by multiplying the sum by $(2\mu_B)S(S+1)/Nk_B$, where S=3.5, μ_B is the Bohr magneton, and k_B is the Boltzmann constant.

After completing this Monte Carlo step, the next spin is considered until all spins on the lattice are sampled. This completes a single Monte Carlo scan. In the actual calculation, the lattice is scanned n times at each temperature, i.e., n Monte Carlo steps are completed for each spin. Out of the n total scans, the first n_{eq} (denoting the number of equilibriation scans) Monte Carlo scans are used to bring the system to an equilibrium state. Only the last n_{samp} (denoting the number of sampling scans) scans are used for calculating the thermal averages of the desired observables, where $n= n_{eq} + n_{samp}$. For example, the thermal average of the magnetization at a fixed temperature is obtained by computing $< M >= \frac{\sum_l^{n_{samp}} (\sum_i^N S_i)}{n_{samp}}$.

The Metropolis algorithm works for the Ising model because with a sufficiently large n_{eq}, the ensemble consisting of the last n_{samp} spin configurations will approximately have the Boltzmann distribution. Thus in the large n ($n= n_{eq} + n_{samp}$) limit

for the Monte Carlo scans, the Metropolis algorithm gives the exact result. However, we will have to find out how large a number of n will be sufficient for our purpose empirically.

7.4 Monte Carlo and Error Analysis

In this part of the Monte Carlo chapter, we address two issues: firstly, the number of Monte Carlo steps needed to reach the equilibrium state, and secondly, the number of steps needed to obtain various thermodynamic variables (e.g., the average magnetization $< M >$, or the susceptibility χ) and the errors associated with these values.

Generally, we empirically determine the number of Monte Carlo steps needed for equilibriation by plotting selected observables as a function of the number of Monte Carlo steps and noting at a certain stage that the initial transient behaviors appear to end. For the Ising model and the Clock model with 6-fold symmetry using the Metropolis algorithm, we found that several hundred Monte Carlo steps are sufficient to bring our system to an equilibrium state for a lattice size $L \leq 30$. Sometimes, we have also used 2000 Monte Carlo steps for lattices with $L=60$.

In order to know how many Monte Carlo scans are enough, we need to know the errors associated with the scans. We define the error bar as plus/minus ($\pm$) one standard deviation, which is the square root of the variance. The variances for the magnetization and energy are slightly complicated because successive states generated by the computer are correlated, so that the $[var(< M >)] > [< M^2 > - < M >^2]$. Specifically, the variance of the average magnetization is:

$$var(< M >) = \frac{1}{n_{samp}} 2\tau_{int} C(0), \tag{7.3}$$

where the autocorrelation function $C(t)$ is defined as

$$C(t) = < M_s M_{s+t} > - < M >^2 \tag{7.4}$$

and the integrated autocorrelation time (here time is not the physical time, but instead it is a measure of the number of Monte Carlo scans) τ_{int} is

$$\tau_{int} = \frac{1}{2} + \sum_{t=1}^{\infty} \frac{C(t)}{C(0)}. \tag{7.5}$$

The subscripts s and $s+t$ for M refer to the magnetization values calculated at Monte Carlo scan s and Monte Carlo scan $s+t$, respectively. Thus from the formula for $C(t)$, we obtain the correlation between the magnetizations of different Monte Carlo scans.

The error bars for observables like the susceptibility and the specific heat are even more complicated. For example, the susceptibility is proportional to the fluctuations in the magnetization. Thus computation of the error bars for the susceptibility is equivalent to computing the variance of the errors of the magnetization. The standard deviation formula for χ is given in Ref [66] as:

$$standard\ deviation(\chi) = 2\chi\sqrt{\frac{\tau_2}{n_{samp}}} \tag{7.6}$$

where τ_2 is a measure of autocorrelation time and is defined as

$$\tau_2 = 0.5 + \sum \rho^2(t) \tag{7.7}$$

and the autocorrelation function $\rho(t)$ is given by

$$\rho(s) = \frac{< M_s M_{s+t} > - < M >^2}{< M^2 > - < M >^2}. \tag{7.8}$$

We have incorporated the error analysis described above into simulation of both the magnetization and the susceptibility calculations for the EuTe/PbTe SLs.

7.5 Program Validation

To carry out the simulation in this chapter, I started learning the Monte Carlo technique from the beginner's level.[67] However, it was not long before we had the first Monte Carlo program for a monolayer Ising ferromagnet working. Specifically, I modified a code written in ANSI C for hydrogen adsorption onto a palladium surface to a new program for an Ising ferromagnet on a square lattice. The original code was written by Boris Pevzner for MIT course 3.320. Later the program was modified further to a triangular lattice and with a variable number of layers (ranging from 1 to 7) of abc stacking, like that of the (111) planes for a fcc crystal. To demonstrate that our Ising program works correctly, we have compared the value of the transition temperature T_c obtained from our program to the analytical value for T_c. Figure 7-1 shows a plot of the magnetization vs. temperature for a monolayer Ising ferromagnet on a triangular lattice. The T_c determined from this plot is 3.6 K, in good agreement with the T_c= 3.6409579 K determined analytically for a 2D triangular lattice.[68]

The first major extension of the initial computer program came when we changed it from an Ising model to a Heisenberg model, following the recipe provided in Ref.[69] for a Heisenberg magnet, and based on the Metropolis algorithm.[65] The Heisenberg model is a continuous model in which the spins can point in any direction over a 4π solid angle, whereas the Ising model is a discrete uniaxial model, which allows spins only to point either up or down. Thus, in Monte Carlo simulations for the Heisenberg model, we can only compute the modulus of the magnetization because we don't know how the spins are pointing. Specifically, the modulus of the magnetization, denoted by M_{rms}, is found according to $M_{rms}=\sqrt{M_x^2 + M_y^2 + M_z^2}$, where M_x, M_y, and M_z are the three orthogonal components of $\vec{M}$. In Fig. 7-2 we compare the rms magnetization vs. temperature to the first Monte Carlo simulation for a 2D Heisenberg ferromagnet, and we found they have similar behaviors.[70] Although the exercise of extending our Ising Monte Carlo program to a Heisenberg Monte Carlo program without dipolar forces doesn't produce any meaningful results for SLs, later we reaped benefits from this modification in the Monte Carlo calculations for a Clock

model with 6-fold symmetry.

7.6 Ising Model

Although EuTe is a Heisenberg antiferromagnet, we nevertheless chose to perform an Ising Monte Carlo simulation for two reasons. Firstly, it is known that a 2D Ising spin system has a phase transition at a finite temperature, coinciding with our experimental susceptibility observations. This is to say, a 2D Ising Monte Carlo simulation with a finite number of EuTe MLs will yield more interesting information than a 2D Heisenberg Monte Carlo simulation, which is known, a priori, should not exhibit a phase transition at nonzero temperature.[5] Secondly, because EuTe has a type II antiferromagnetic spin structure, we would expect rather different susceptibility behaviors between SLs with an odd number of EuTe MLs and SLs with an even number of EuTe MLs. A 2D Ising simulation is sufficient to illustrate this difference.

There are limitations in using Ising Monte Carlo simulations for EuTe/PbTe SLs that we should point out at the outset. In choosing to follow the Ising model approach, we have implicitly assumed that the spins lie along a certain direction in the (111) planes. This is not true in SLs for $T > T_c$ where the spins can point in any direction in 3-dimensional space. Further, for $T < T_c$, although the spins are in the (111) planes, they can point along any direction within those planes. Therefore, within the framework of the Ising model, we will not obtain any information regarding χ_{out}, and, by default, we take χ_{out} to be zero. Furthermore, the calculated susceptibility, within the Ising model is only the $\chi_{\parallel}$ component of χ_{in}. We recall that in Chapter 6 we have postulated that $\chi_{in} = \frac{1}{2}\chi_{\parallel} + \frac{1}{2}\chi_{\perp}$ based on the assumption that the magnetic domains are randomly oriented. To remind us of the limitations of the Ising model, we will always label the simulated susceptibility as $\chi_{\parallel}$ in this section.

7.6.1 Input Parameters

We have used the convention of setting the nearest-neighbor exchange coupling J_1 =1 in the units of k_B-K, and we rescale the next-nearest-neighbor coupling to be J_2 =

-3.75, so that the ratio of J_2/J_1 agrees with that of bulk EuTe. We have constructed triangular lattices with *abc* stacking order just like the successive (111) planes of a fcc crystal. In the Ising Monte Carlo simulation each site i of the lattice is occupied by a spin S_i, where S_i is a one-dimensional vector with $\pm$ 1 values. Later when we present the results of the simulation, we have rescaled the values of J_1, J_2, and S to those of EuTe. The energy is given by Eq.(7.2), and periodic boundary conditions are used. A lattice size L of either 30 or 60 is adopted for the simulations. We didn't investigate the finite size scaling behavior here because it has been thoroughly studied before for the Ising Model.[71] Most of the simulations were performed on a Sun Sparc workstation.

7.6.2 $M_{rms}(T)$

Although we are interested in the temperature dependences of the SL susceptibilities $\chi_{\|}(T)$, we must first calculate $M(T)$. The $M(T)$ results are important in their own right because we can use them to infer the spin structures in the simulated SL systems. In Fig. 7-3 Monte Carlo results for $M_{rms}(T)$ versus temperature are plotted for three SLs with ξ=odd. $M_{rms}(T)$ is chosen as the variable to describe the magnetization rather than $M(T)$ because near the transition temperature T_c, $M(T)$ fluctuates between plus and minus frequently, whereas $M_{rms}(T)$ varies monotonically. As T decreases below T_c, the rapid rise in $M_{rms}(T)$ shown in Fig.7-3 signals the onset of long-range magnetic ordering. As T goes to zero, the $M_{rms}(T)/M_{total}$ ratios in Fig. 7-3 (M_{total} is saturation magnetization in the low temperature limit given by M_{total}=$NgS\mu_B$ where N is the total number of spins) approach the $\frac{1}{3}$, $\frac{1}{5}$, and $\frac{1}{7}$ limits for SLs with ξ=3, 5, and 7, respectively. This implies that the magnetic order established in the simulated SLs is of the type II antiferromagnetic kind, i.e., ferromagnetically ordered (111) planes with spins on adjacent planes aligned antiparallel.

In Fig. 7-4 results for $M_{rms}(T)/M_{total}$ versus temperature are shown for two SLs with ξ=even. The $M_{rms}(T)$ limits as $T \longrightarrow 0$ K for both SLs are zero, suggesting antiferromagnetic order. The T_c is where $M_{rms}(T)$ abruptly changes its slope. The high T limits of $M_{rms}(T)/M_{total}$ approach $1/\sqrt{N}$ due to random fluctuations, where

N is the total number of spins. For the SL with ξ=4, N is 30×30×4=3600, and we would expect $M_{rms}(T)$ to go to 0.16 as T increases. Similarly for the ξ=6 SL, N is 30×30×6=5400, and we would expect $M_{rms}(T)$ to go to 0.13 as T increases. However, in the temperature window between T=0 K and T=T_c, $M_{rms}(T)/M_{total}$ for ξ=even SLs is predicted to increase monotonically as T increases. This behavior is unlike the experimental $M(T)$ observations for the ξ=4 and ξ=6 SLs, which show first an increase and then a decrease in magnetization as T approaches T_c from below (see Chapter 4). This discrepancy may be due to a number of factors, which are addressed in this Chapter. One explanation for the discrepancy may be in part due to the experimental data being taken in a small external field while the simulated $M_{rms}(T)$ are calculated in zero field. The discrepancy may also be in part due to EuTe being an easy plane not an Ising antiferromagnet. We can correct for the field dependence of the magnetization by applying the relation $M_{rms}(T, H = small) = M_{rms}(T, H = 0) + \chi_{\|}(T, H = 0)H$, but first we have to know $\chi_{\|}(T)$, which is the topic of the next section.

7.6.3 $\chi_{\|}(T)$

$\chi_{\|}(T)$ is obtained formally by calculating $< M^2(T) > - < M(T) >^2$. In our presentation of the $\chi_{\|}(T)$ results, again we will divide the presentation into results for ξ=odd and for ξ=even. Figure 7-5 shows $\chi_{\|}(T)$ versus temperature for three ξ=odd SLs with ξ=3, 5, and 7. Each of the three SLs has one layer of uncompensated spins, thus leading to a $\chi_{\|}(T)$ which shows a sharp peak, like the divergent susceptibility of a ferromagnet. The peak temperature is identified with T_c. The divergent behavior of the $\chi_{\|}(T)$ as $T \longrightarrow T_c$ agrees well with the experimental data of the corresponding three SLs with ξ=odd. Further, the uncompensated spins decreases as a percentage of the total number of spins as ξ increases. Consequently, the maximum value of $\chi_{\|}(T)$ decreases as ξ increases, also in agreement with the experimental data. In Fig.7-6 simulated results for $\chi_{\|}(T)T^2$ vs. T are shown to illustrate that for temperatures above the divergence of $\chi_{\|}(T)$, the susceptibility $\chi_{\|}(T)$ has a Curie-Weiss temperature-dependence. Unlike the experimental data of $\chi_{in}(T)$, the simulated $\chi_{\|}(T)$ approaches

zero as T goes to zero, while the experimental $\chi_{in}(T)$ approaches a constant value for these SLs. This is consistent with our postulation that $\chi_{in}(T)$ includes both $\chi_{\|}(T)$ and $\chi_{\perp}(T)$, and that $\chi_{\perp}(T)$ has a nonzero value at T=0 K (see Fig.6-13).

Fig.7-7 shows the simulated $\chi_{\|}(T)$ versus T for two SLs with ξ=4 and ξ=6. Notice the absence of sharp peaks in $\chi_{\|}(T)$ among these two ξ=even SLs, in contrast to those SLs shown in Fig. 7-5 for ξ=odd. The $\chi_{\|}(T)$ behavior for ξ=even SLs is thus very similar to that of an antiferromagnet. Although there are no sharp peaks in the $\chi_{\|}(T)$, the derivative $\frac{\partial\chi_{\|}(T)}{\partial T}$ does have a singularity. The transition temperature is thus identified as the temperature where $\chi_{\|}(T)$ has an infinite slope.[48] The results for $\chi_{\|}(T)T^2$ vs. T are plotted in Fig. 7-8 for the ξ=4 and ξ=6 even SLs. The linear region of $\chi_{\|}(T)T^2$ represents paramagnetic Curie-Weiss behavior, consistent with our expectation.

So far the simulated $\chi_{\|}(T)$ results based on the Ising model are consistent with the divergent $\chi_{\|}(T)$ behavior observed in ξ=odd SLs and with attributing this effect to uncompensated spins. At the same time, the $\chi_{\|}(T)$ simulations for ξ=even SLs are like that of an antiferrromagnet without any divergence, in agreement with our expectation. However, for ξ=even SLs, the experimental $\chi_{in}(T)$ data also show divergent-like peaks. To reconcile this difference in behavior, we note that the real ξ=even SLs are very likely not as perfect as the SLs we have constructed in the computer simulation. For example, in a real SL with ξ=4 there are regions where ξ=5 and ξ=3 as well as regions where ξ=4, the nominal magnetic layer thickness. In fact, the x-ray diffraction data for the ξ=4 sample shows that, on average, the EuTe thickness is 4.86 monolayers, with defects limited to monolayer steps at the EuTe-PbTe interfaces. In order to mimic this defect in our simulation, we have calculated $\chi_{\|}(T)$ for a SL of 4.86 EuTe monolayers, by introducing a fifth fractional monolayer on top of 4 perfect layers. The fifth layer is covered randomly with 86% of the sites by spins and the remaining 14% of the sites by vacancies. The overall lattice size is also increased to 60×60. Notice that the fractional monolayer basically consists of uncompensated spins. The $\chi_{\|}(T)$ for this simulation indeed shows a peak (see Fig. 7-9). From that we conclude that the peaks seen in the EuTe(4)/PbTe(12) and in the

EuTe(6)/PbTe(18) SLs may be due to structural imperfections, such as the fractional monolayer defect introduced in the simulations.

7.6.4 $M_{rms}(T)$ revisited

In this section we extend the discussions on the $M_{rms}(T, H = 0)$ simulation given in Section 7.6.2 by considering $M_{rms}(T, H = 4gauss)$ in a finite measurement field using the relation:

$$M_{rms}(T, H = 4gauss) = M_{rms}(T, H = 0) + \chi_{\|}(T, H = 0) \times 4. \qquad (7.9)$$

The results for $M_{rms}(T)$ in a finite field of 4 gauss are shown in Fig. 7-10 for both ξ=4 and ξ=6 SLs. Whereas the results in Fig.7-10 are improved compared to the zero field $M_{rms}(T, H = 0)$ of Section 7.6.2, however, the present calculated results still can't quantitatively fit the experimental observation of $M(T)$ (see Chapter 4). Therefore, we conclude that the Ising model is inadequate to describe the temperature dependence of the magnetization quantitatively for EuTe/PbTe SLs.

7.7 Heisenberg Model with Dipolar Coupling

Although the Ising model has provided us with an explanation for the divergent $\chi_{in}(T)$ behavior, the model, however, is unable to tell us anything regarding $\chi_{out}(T)$, and more importantly, the anisotropy between $\chi_{in}(T)$ and $\chi_{out}(T)$. To address the last two issues, we turn to a completely different model, the Heisenberg model with dipolar forces. Before we present the simulations of this model, we will give a brief motivation as to why we think this model is appropriate.

So far in our magnetic studies of EuTe/PbTe SLs, we have learned that the exchange couplings in EuTe are isotropic. The magnetic moment of Eu^{2+} comes exclusively from the 7 electrons in the half filled 4f shell, and thus by Hund's rule the orbital angular momentum L =0. Further, the static magnetization studies of in-plane ((111) plane) magnetization for SLs show no detectable anisotropy, in agreement

with the Antiferromagnetic Resonance (AFMR) result obtained from bulk EuTe, an easy plane antiferromagnet. In short, all the data we have indicate that EuTe/PbTe SLs are ideal Heisenberg SLs. However, Mermin and Wagner have shown that a 2D Heisenberg system cannot have a phase transition at finite temperatures $T > 0$ K.[5] Yet we have seen unambiguous phase transitions in SLs with $\xi \geq 3$, accompanied by strong anisotropic behavior in the susceptibility. To explain these contradictions, we hypothesized that it would be important to include the presence of dipolar coupling, albeit weak, but of a long range character, to provide an anisotropy between $\chi_{in}(T)$ and $\chi_{out}(T)$. Our hypothesis that dipolar forces might stablize the long-range order in EuTe/PbTe SLs is motivated by earlier work by S. V. Maleev,[8] in which he has demonstrated theoretically that the dipolar coupling can stabilize long-range order in a 2D Heisenberg system.[8] We believe that the Heisenberg model with dipolar coupling given by

$$\mathcal{H} = -J_1 \sum_{nn} \vec{S}_i \cdot \vec{S}_j - J_2 \sum_{nnn} \vec{S}_i \cdot \vec{S}_j + g \sum_i \sum_j \frac{\vec{S}_i \cdot \vec{S}_j - 3(\vec{S}_i \cdot \hat{r_{ij}})(\vec{S}_j \cdot \hat{r_{ij}})}{|\vec{r_{ij}}|^3} \qquad (7.10)$$

where $g = (2\mu_B S)^2/a^3$ is the dipole-dipole coupling constant, a is the lattice constant, μ_B is the Bohr magneton, and S=7/2, is perhaps the most accurate model for characterizing EuTe/PbTe SLs. Since we have not found any experimental system that realizes the theoretical description given by S. V. Maleev,[8] if our hypothesis is correct, that will make the EuTe/PbTe SLs the first experimental realization of long-range order in a 2D Heisenberg system stabilized by dipole-dipole interactions.

The Monte Carlo simulation including the dipole-dipole interaction term is more involved compared to that for the Ising model. Dr. Lorenzo Bergomi was largely responsible for developing and implementing the computer program for this model. Here we will highlight some important aspects of his findings.

7.7.1 Heat-bath Method

Firstly, the computer algorithm used for the Heisenberg model with dipolar coupling is the heat-bath method.[72] Unlike the Metropolis algorithm, every update on the spin

is accepted. However, the new spin orientation is not generated randomly. Instead, the new spin orientation is generated from a distribution of the form $e^{-\vec{h_i}\cdot\vec{S_i}/k_BT}$, where

$$h_i^\alpha = -J_1 \sum_{nn} S_j^\alpha - J_2 \sum_{nnn} S_j^\alpha + g \sum_{j,\beta} \frac{S_j^\beta}{|r_{ij}|^3}(\delta_{\alpha\beta} - 3\frac{r_{ij}^\alpha r_{ij}^\beta}{|r_{ij}|^2}). \tag{7.11}$$

Since the Heisenberg model is a continuous model, each spin S_i of unit length needs two angles to specify its orientation, the polar angle θ and the azimuthal angle ϕ. In practice, the angle ϕ is obtained by generating a random number from an uniform distribution in the interval 0 to 2π, while the polar angle θ, which is in the range 0 to π, is obtained in two steps. The first step gives a random number u between e^{-h} and e^{h}. In the second step, the random number u is set equal to $e^{-\beta h cos\theta}$ thereby introducing an angular dependence of θ. The heat-bath algorithm is more efficient compared with the Metropolis algorithm in terms of computer time, because there is no "if" statement in the heat-bath method.

7.7.2 Input Parameters

The exchange couplings are again rescaled such that J_1= 1 and J_2=−3.75. The ratio of J_2/J_1 is chosen to reflect the bulk J_2/J_1 ratio for EuTe and the different signs for J_1 and J_2 indicate that one exchange coupling is ferromagnetic and the other is antiferromagnetic. In addition to the parameters J_1 and J_2, a third input parameter g (where $g = (2\mu_B S)^2/a^3$), characterizing the dipole-dipole coupling strength, taken to be 0.64 in relation to J_1 is rescaled to 1 (see Eq.7.10). Note that g has comparable strength when compared to the exchange couplings J_1 and J_2 in EuTe. We can discount the concern that bulk J_1 and J_2 values may contain contributions from the dipolar forces already for the following two reasons. Firstly, the magnetic ordering in bulk EuTe is stabilized by the exchange J_1 and J_2 couplings alone without dipolar interactions. Secondly, the values of J_1 and J_2 that are used here were obtained from the Curie-Weiss temperature θ and the transition temperature for bulk EuTe. Together, the above-mentioned reasons explain why there are large uncertainties attached to the J_1 and J_2 values (J_1/k_B=0.04±0.01 K and J_2/k_B=-0.15±0.01 K) and

little dipolar contributions in the reported bulk J_1 and J_2 values.

In our simulations, only the dipolar interactions within a (111) plane are accounted for, whereas the dipolar interactions out of the (111) plane are considered as zero. This assumption is based on the estimation of dipolar energy per Eu atom using the formalism developed by S.V. Maleev, which suggests an exponential decay of the dipolar interaction strength as a function of the number of atomic planes.[8] Specifically, within a (111) plane, the dipolar energy per Eu atom is approximately -0.8 K.[73] The negative sign indicates that the dipoles within the same (111) plane tend to align themselves in a ferromagnetic order. The dipolar energy per Eu atom due to the spins on the next (111) plane is approximately 0.007 K. The positive energy here implies that the spins on the adjacent (111) planes tend to be aligned in opposite directions. Clearly, the out-of-plane dipolar interaction is much weaker compared to the in-plane dipolar interaction. Thus we have ignored the out-of-plane dipolar interactions in our simulations. Furthermore, the dipole interactions between Eu spins separated by PbTe is effectively zero.

The lattice size is chosen to include $13\times13\times3$ spins, and most simulations were performed for an EuTe(3)/PbTe(9) SL. The choice of lattice size and the focus on only one SL are both consequences of the limited available Cray time for this calculation. However, simulations on one SL are sufficient since we seek to explain the cause of long-range order and the anisotropic susceptibility behavior which are common features of all SLs with $\xi\geq3$. Furthermore, two simulation runs with a $23\times23\times3$ spin lattice didn't show any difference in either the $\chi_{in}(T)$ or $\chi_{out}(T)$ behavior when compared to those of the $13\times13\times3$ spin lattice.

7.7.3 Results on $\chi_{in}(T)$ and $\chi_{out}(T)$

In the initial runs of the Monte Carlo simulations using a Heisenberg model with dipolar forces, we have calculated χ_{xx}, χ_{yy} and χ_{zz} with $\vec{x}$ and $\vec{y}$ taken as two orthogonal vectors in the (111) planes, and $\vec{z}$ taken perpendicular to the (111) planes. χ_{xx} is obtained by the formula $\chi_{xx}=\frac{(2\mu_B)^2}{Nk_BT}(< M_x^2 > - < M_x >^2)$ where M_x is the x-component of the total magnetization. Similar formulae are used for calculating

χ_{yy} and χ_{zz}. From these three susceptibility components, we can construct χ_{in} as $\chi_{in}=\frac{1}{2}(\chi_{xx}+\chi_{yy})$, while χ_{zz} yields χ_{out}.

Figure 7-11(a-b) shows χ_{in} (i.e., $\frac{1}{2}(\chi_{xx}+\chi_{yy})$) and χ_{out} vs. T. There are two encouraging features in this simulation result: (1) χ_{out} is very similar to the experimental χ_{out} which increases monotonically but with a very slight temperature dependence. Further the simulated $\chi_{out}(T=0)$ limit is within 80% of the experimental $\chi_{out}(T=0)$ value and is very sensitive to the dipolar coupling constant g we have used. (2) There is a spontaneous separation between $\chi_{in}(T)$ and $\chi_{out}(T)$ as T is reduced below $\sim T$ =8.8 K, although it is difficult to determine T_c accurately from this plot because of the large fluctuations in the calculated χ_{in} at low temperatures. We have also calculated the specific heat from the same run (see Fig. 7-12). The specific heat data shows T_c=5.5 K, well below the temperature where χ_{in} and χ_{out} separate from one another.

To emphasize the similarity between the simulated susceptibility and the actual experimental data, we have plotted $\chi_{in}(T)$ and $\chi_{in}(T)$ from the simulation and from the experimental measurements side by side in Fig. 7-13, in the temperature region immediately above T_c.

As seen in Fig.7-11, χ_{xx} and χ_{yy} are extremely unstable at $T<T_c$. The cause of this unstability is intrinsic to the finite size of the Monte Carlo simulation using a continuous spin model. In other words, because the spins pointing in different directions within the (111) planes have the same energy for $T<T_c$, the simulated spins will rotate continously within the planes without costing any additional energy. The continuous random rotations of spins make both χ_{xx} and χ_{yy} unstable. To bypass this difficulty with the Monte Carlo simulation, we chose to calculate χ_{rms} instead, which is defined as $\frac{(2\mu_B)^2}{Nk_BT}< M_{rms}^2 > - < M_{rms} >^2$ where M_{rms} is the same root-mean-squared magnetization previously defined when using the Ising model simulation. Thus we have used χ_{rms} in the Monte Carlo simulation for the Heisenberg model as an approximation to χ_{in} for $T<T_c$. The results of χ_{rms} vs. T are shown in Fig. 7-14, where it is seen that $\chi_{rms}(T)$ has a divergent peak at $T=T_c$=5.5 K, just as was found in the specific heat simulation, and in agreement with the experimental χ_{in}.

However, unlike the experimental data, the simulated $\chi_{rms}(T)$ approaches zero as $T \longrightarrow 0$ K. In fact, one can show that χ_{rms} coincides with $\chi_{\|}$ at low temperatures. However, whether χ_{rms} will continue to overlap with $\chi_{\|}$ as T increases up to the transition temperature is not clear to us. We would like to obtain a more complete approximation to χ_{in} which includes both $\chi_{\perp}$ and $\chi_{\|}$, and to this end, we turn to the Clock model with 6-fold symmetry.

7.8 Clock Model

The Clock model is an extension of the Ising model, where the spin degrees of freedom are still discrete. However, the spins in the Clock model can point along more than two opposite directions as in the Ising case. The additional degrees of freedom available to the spins enable us to calculate the $\chi_{\perp}$ which is not obtainable from the Ising model. Furthermore, we have chosen the Clock model with 6-fold symmetry, rather than other symmetries, because the crystal symmetry of the (111) planes of EuTe are triangular lattices with 6-fold planar symmetry. As in the case of the Ising model, in the 6-Clock model we assume that the spins lie in the (111) planes. This assumption will again prevent us from obtaining information on χ_{out}. However, there is a hope that we might obtain $\chi_{\perp}$ from this model, which is not obtainable from either the Ising or Heisenberg models with dipolar forces.

In the 6-Clock model, each spin has 6 degrees of freedom. The six allowed directions are uniformly spaced from 0 to 2π, such that two adjacent directions are 60° apart. Like the Ising simulation, we also used the Metropolis algorithm for the Clock model. At each Monte Carlo step, the spin can be randomly moved clockwise or counter clockwise by 60° or remain in the same direction. Because there are six directions, there is a possibility that we can calculate $\chi_{\perp}$ from this model. However, the $\chi_{\perp}$ obtained here is only an approximation for $\chi_{\perp}$ in EuTe because the experimental data indicate that EuTe has zero in-plane ((111) plane) anisotropy.

The specific method for calculating the in-plane $\chi_{\perp}$ and $\chi_{\|}$ (since the magnetic domains can point along any direction within the (111) planes, $\chi_{in}=\frac{1}{2}(\chi_{\perp} + \chi_{\|})$)

is outlined below. At each temperature, the spins are first allowed to equilibriate. During the sampling process, at the end of each Monte Carlo scan, two orthogonal components of the total magnetization (M_x and M_y) are calculated. After all the Monte Carlo sampling scans are completed, the average M_x is computed using the relation $< M_x >= \frac{\sum_i^{nsamp} M_x^i}{n_{samp}}$, and the average M_y is similarly computed. By use of the tangent relation $tan\theta = < M_y > / < M_x >$, the average angle θ of the magnetization with respect to the x-axis is computed. In the last step, we decompose all the M_x and M_y data generated from different Monte Carlo scans into two orthogonal directions, one which is along the average θ direction ($M_{\|}$ component of the total magnetization), the other which is perpendicular to the average θ direction ($M_{\perp}$ component of the total magnetization). Figure 7-15 illustrates the geometry of $M_{\perp}$ and $M_{\|}$ in relation to the average θ, M_x, and M_y. Finally, use the definition of χ to obtain $\chi_{\perp}$ as $< M_{\perp}^2 > - < M_{\perp} >^2$, and $\chi_{\|}$ as $< M_{\|}^2 > - < M_{\|} >^2$.

7.8.1 Input Parameters

The input parameters for the Clock model with 6-fold symmetry are identical to those used in the Ising model Monte Carlo simulation. All simulations are performed for an EuTe(3)/PbTe(9) SL.

7.8.2 $\chi_{\perp}(T)$ and $\chi_{\|}(T)$

As we have mentioned in Section 7.7.3 for the Heisenberg model with dipolar forces for $T < T_c$, the magnetization direction rotates freely within the (111) planes, thus preventing us from calculating $\chi_{\perp}$. Here in the Clock model with 6-fold symmetry, by monitoring the magnetization direction as a function of Monte Carlo scans, we found that the rotation between Monte Carlo steps is very mild at low temperatures, and the rotation angle θ increases as T increases. Figure 7-16 shows the magnetization direction vs. the number of Monte Carlo scans at five different temperatures. Extreme rotations are only observed in the highest temperature plot (i.e., T=3.8 K).

Incidentally, the T_c for the EuTe(3)/PbTe(9) SL using the Clock model with 6-

fold symmetry is only 3.5 K, as identified by the peak in the specific heat calculation (see Fig. 7-17). The first peak in Fig. 7-17 is identified with the paramagnetic to the 6-clock ordered phase (i.e., spins are pointing in the six allowed directions), and the second bump is identified with the transition from the 6-clock ordered phase to the Ising ordered phase (i.e., spins are pointing along one of the six allowed directions). The 6-clock model T_c is substantially lower than T_c obtained with the Ising model which gives a T_c of 8.2 K. However, the point here is that up to T_c, it seems that there is a possibility we can calculate $\chi_\perp$ using the Clock model.

The results for $\chi_\perp$ are extremely noisy and less encouraging (see Fig. 7-18). After numerous trials, experimenting with different lattice sizes and Monte Carlo scans, we could not make any improvement in calculating $\chi_\perp$. To that end, we concluded that although the fluctuations are small in Fig.7-16, they are dominated by Monte Carlo metastability (i.e., random rotations of the magnetization direction) rather than the thermal fluctuations which we seek to sample.

The whole exercise of carrying out a Monte Carlo simulation using the Clock model did provide us with two new insights that were unexpected. Firstly, when we were trying to find $\chi_\perp$, we simultaneously evaluated $\chi_\parallel(T)$ and $\chi_{rms}(T)$ as well. Figure 7-19 compares the results of a Monte Carlo calculation for $\chi_\parallel(T)$ with the $\chi_{rms}(T)$, and the overlap between $\chi_\parallel$ and χ_{rms} at $T<T_c$ confirms that χ_{rms} obtained in the simulations of the Heisenberg model is only the parallel component of the χ_{in} susceptibility. Secondly, the T_c (3.5 K) found through the Clock model for an EuTe(3)/PbTe(9) SL is lower than that of the Heisenberg model with dipolar forces (5.5 K), and much lower than the experimental T_c value of 7.9 K, although both models have the same input parameters of J_1 and J_2. The comparisons of T_c for the various models indirectly suggests that the Heisenberg model with dipolar forces is the best description of EuTe/PbTe SLs.

7.9 Comment on J_1 and J_2

From our temperaure-dependent magnetization and susceptibility data, the magnetic phase transition temperatures (T_c) for our SLs are accurately determined (see Table 6.1). As expected, the values of T_c increase with the EuTe layer thickness in a single SL period. However, for $\xi \geq 5$ SLs, the T_c values exceed that of bulk EuTe. This may be an indication that the exchange couplings J_1 and J_2 in our SLs have changed from their bulk EuTe counterparts. Figure 7-20 shows the results on the exchange couplings as a function of the lattice constants obtained by W. Zinn.[52] In our SLs, the lattice constant for EuTe is slightly different from the bulk EuTe lattice constant (6.59 Å) because of the lattice mismatch between EuTe and PbTe. Specifically, from the high resolution x-ray diffraction data (see Chapter 2), G. Springholz and C. Pichler have found that the in-plane ((111) plane) EuTe lattice constant has decreased to 6.49 Å and the out-of-plane lattice constant has decreased to 6.51 Å , relative to 6.59 Å for bulk EuTe. Qualitatively speaking, from Fig.7-20, the above-mentioned changes in the lattice constants will cause both the in-plane J_1 and the out-of-plane J_1 to increase, with the in-plane J_1 increasing more than the out-of-plane J_1. We recall that in a fcc crystal, each atom has six nearest-neighbors within the (111) plane and six nearest-neighbors on the adjacent (111) planes. At the same time, we expect the absolute value of J_2 to decrease a little. From Monte Carlo simulations using the Ising model, we found that having the in-plane J_1 increase more than the out-of-plane J_1 is essential for the magnetic ordering in our SLs, because had it been the other way around, there would be frustration created in EuTe spins, and thereby reducing the transition temperature to almost 0 K. Although there are not enough experimental points in Fig.7-20 for us to read off the values of J_1 and J_2 for our SLs, we have estimated by Monte Carlo simulations that a ratio of 1.2 for the in-plane J_1 to the out-of-plane J_1 can account for the increase in the T_c values observed in our SLs, having the SL in-plane and out-of-plane J_1 and J_2 values within the uncertainties reported for the bulk J_1 and J_2 values (the uncertainties for J_1 and J_2 are 0.04 ± 0.01 k_B and -0.15 ± 0.01 k_B, respectively). Finally, we note that the results in Fig. 7-20

are only approximately applicable to the SL case for two reasons. Firstly, for a given change in the lattice constant, the values of J_1 and J_2 for SLs may vary differently from those presribed in Fig.7-20 because Fig.7-20 reflects both changes in the lattice constant and changes in the anions, i.e., from Te^{2-} to O^{2-}. Secondly, the SLs no longer have the cubic symmetry which will result in different polarizations for the outer most electrons compared to those of bulk EuTe, thus affecting the exchange energies J_1 and J_2.

7.10 Summary

In this chapter we have investigated the causes of two key features in the SLs' susceptibility data for the EuTe/PbTe SLs using Monte Carlo simulations. To repeat, the basic assumption made in all the simulations is that the EuTe layers in different SL periods are not significantly magnetically coupled to each other, and thus simulations based on a single SL period are sufficient for describing the entire SL. The key results obtained from the simulations are three fold. Firstly, the results from the Ising model show that the divergent behavior observed in χ_{in} is due to uncompensated spins in ξ=odd SLs. As for perfect ξ=even SLs, it is expected that there should not be any divergence in χ_{in}. However, experimental peaks are observed in χ_{in} for ξ=even SLs, and these peaks are perhaps due to SL imperfections, such as fractional EuTe layers at the EuTe-PbTe interfaces. Secondly, the Heisenberg model with dipolar forces illustrates nicely that the anisotropy in χ_{in} and χ_{out} is induced by dipole-dipole interactions. Further, the good numerical agreement between the experimental $\chi_{out}(T = 0)$ limit and the simulated $\chi_{out}(T = 0)$ limit which is very sensitive to the input parameter g, shows that the very long-range order seen in these SLs at nonzero temperature is most likely stabilized by dipolar forces rather than anisotropic exchange couplings. Finally, calculation of the $\chi_{\perp}$ component of χ_{in} remains elusive. Although the Clock model with 6-fold symmetry showed some promise for calculating $\chi_{\perp}$, no useful results have yet been obtained with this model. Nevertheless, we learned empirically from our attempts to calculate $\chi_{\perp}$ that χ_{rms} is equal to $\chi_{\parallel}$ and that the long-range

order stabilized by the in-plane 6-fold anisotropy has a T_c value too low compared to that of the experimental observations.

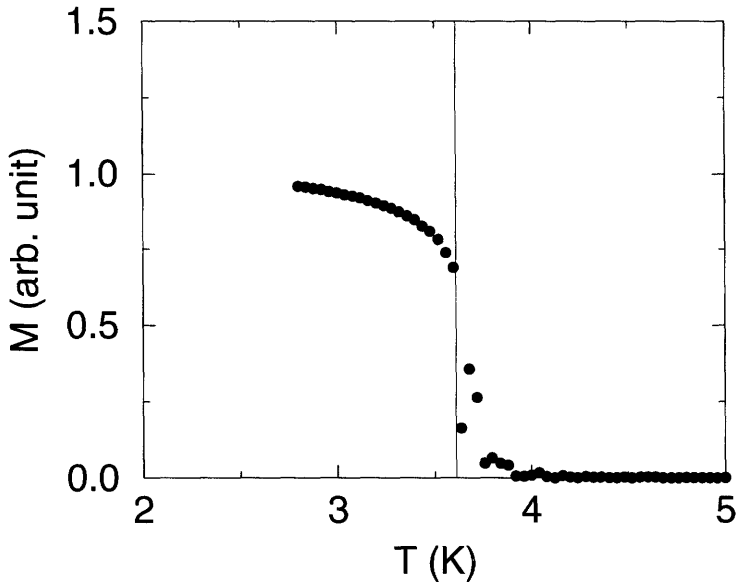

Figure 7-1: M vs. T for a 2D ferromagnet on a triangular lattice size of 100×100, with n=6000 Monte Carlo scans. The vertical line marks the temperature where the transition temperature T_c (=3.6 K) is determined from this simulation.

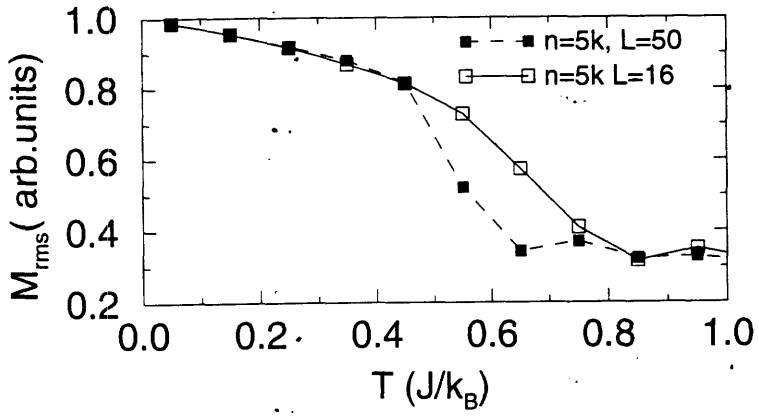

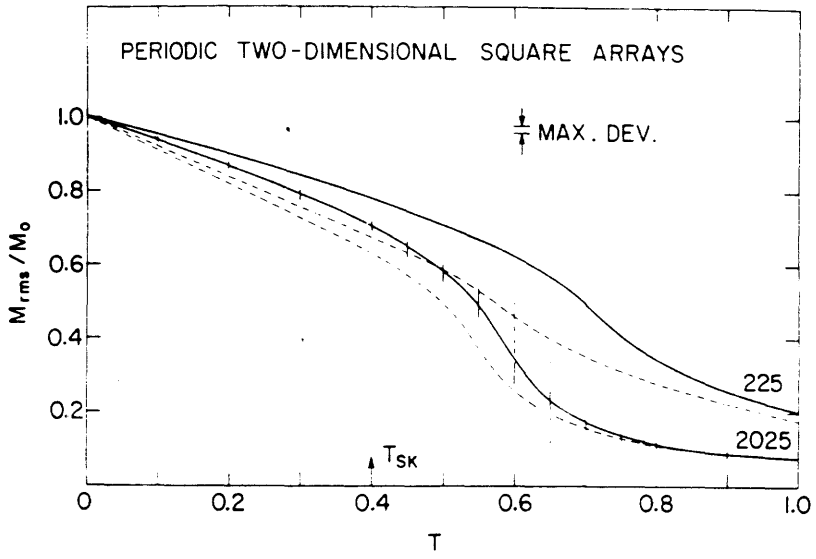

Figure 7-2: Root-mean-square magnetization versus temperature from Monte Carlo calculations for two lattice sizes of a two-dimensional square arrays of spins with periodic boundary conditions. The lattice sizes for our simulations are (upper panel) 50×50 and 16×16. Similar results were reported earlier by Watson et. al. in Ref.69 using periodic boundary conditions with lattice sizes of 225 spins and 2025 spins (lower panel). The dashed lines indicate the M_{rms} behavior for isolated two-dimensional arrays, i.e., without periodic boundary conditions.

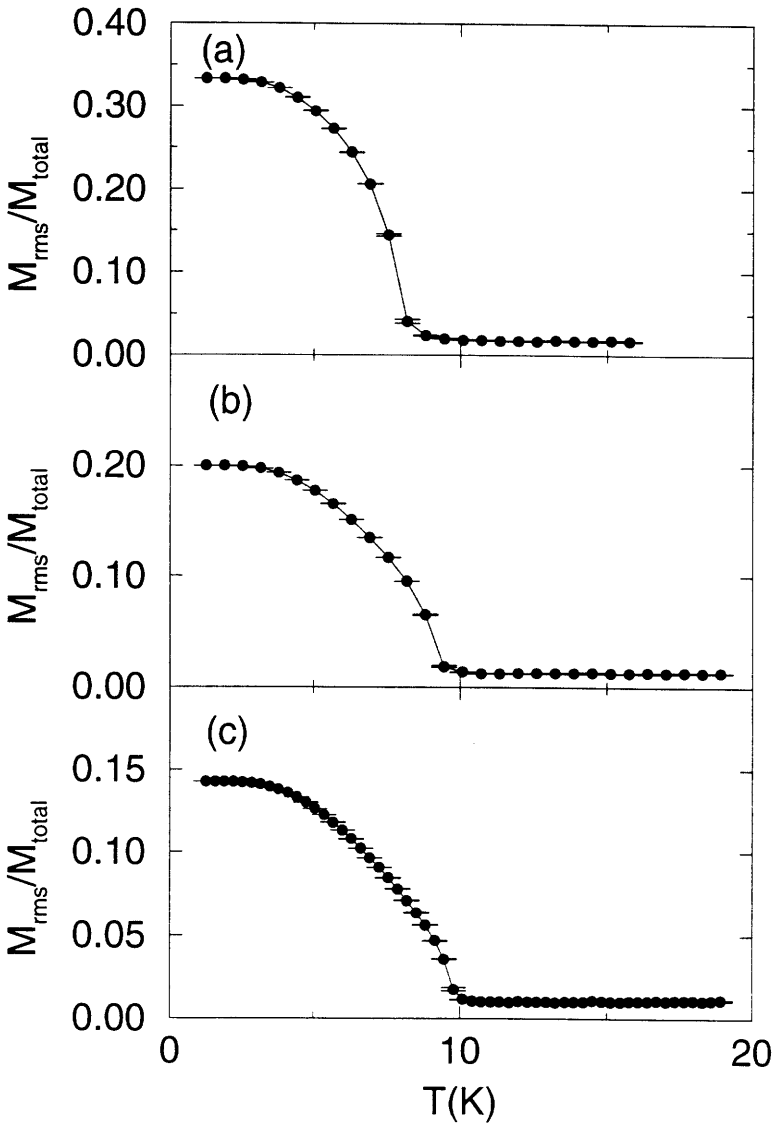

Figure 7-3: Normalized M_{rms} vs. T for an EuTe(3)/PbTe(9) SL of dimensions 30x30x3 (a), an EuTe(5)/PbTe(15) SL of dimensions 30x30x5 (b), and an EuTe(7)/PbTe(21) SL of dimensions 30x30x7 (c). For all simulations, at each temperature, 500 Monte Carlo scans were used for equilibriation and 2000 Monte Carlo scans were used for sampling. In these plots, $M_{rms}(T)$ is normalized to M_{total} (see text). Notice that with the above conditions, the computed error bars are so small that they are hardly readable from the graph.

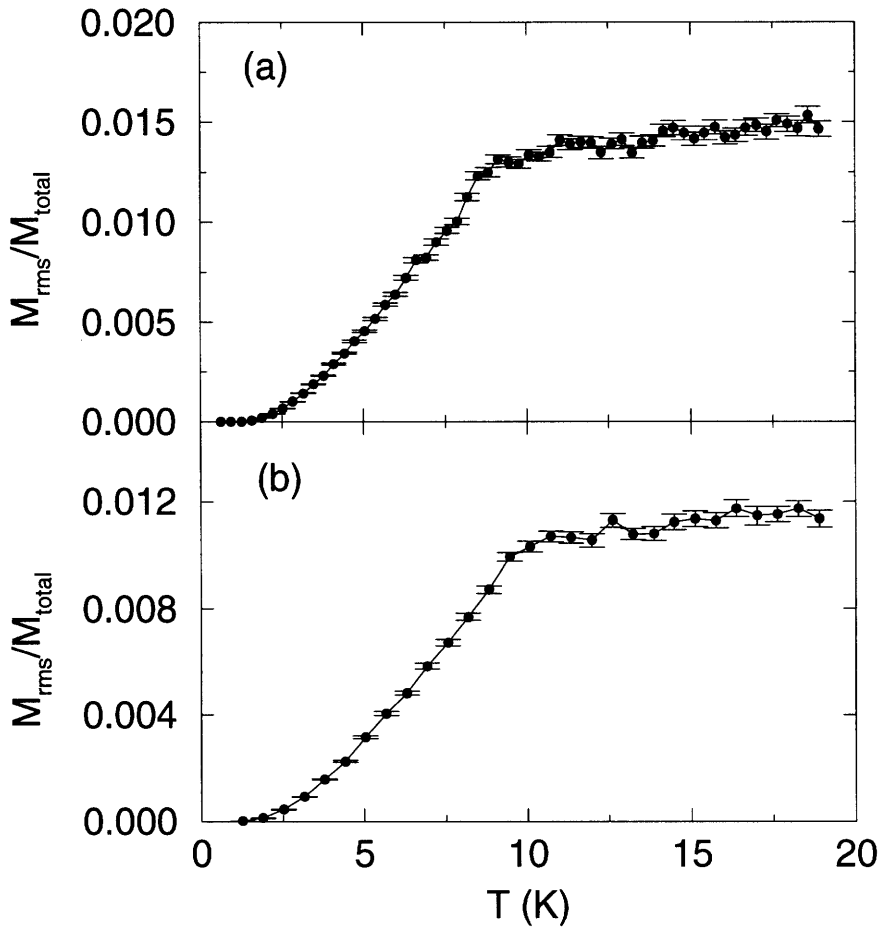

Figure 7-4: M_{rms}/M_{total} vs. T for an EuTe(4)/PbTe(12) SL of dimensions 30x30x4 (a), and an EuTe(6)/PbTe(18) SL of dimensions 30x30x6 (b). All simulations took 500 Monte Carlo scans for equilibriation and 2000 Monte Carlo scans for sampling at each temperature.

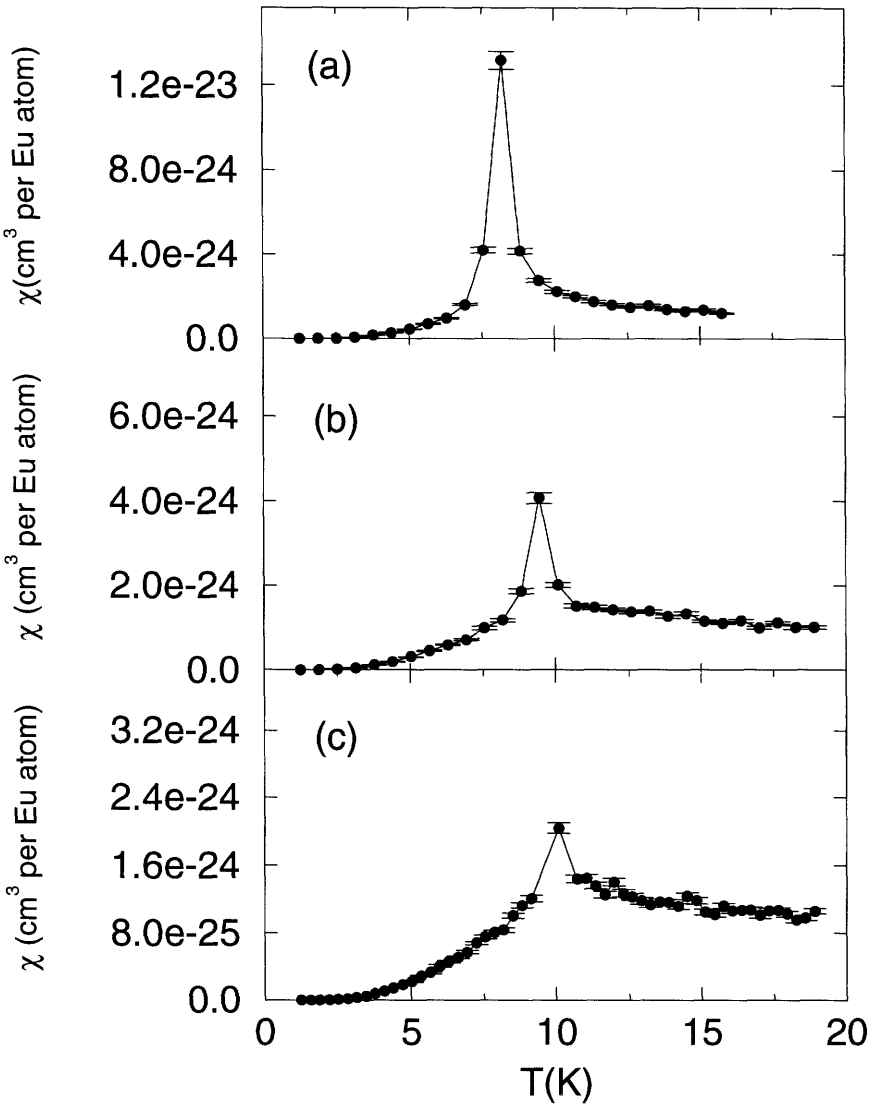

Figure 7-5: $\chi_{\|}(T)$ vs. T for an EuTe(3)/PbTe(9) SL of dimensions 30x30x3 (a), an EuTe(5)/PbTe(15) SL of dimensions 30x30x5 (b), and an EuTe(7)/PbTe(21) SL of dimensions 30x30x7 (c). All simulations took 500 Monte Carlo scans for equilibriation and 2000 Monte Carlo scans for sampling at each temperature. The notation 1.2e-23 denotes 1.2×10^{-23}.

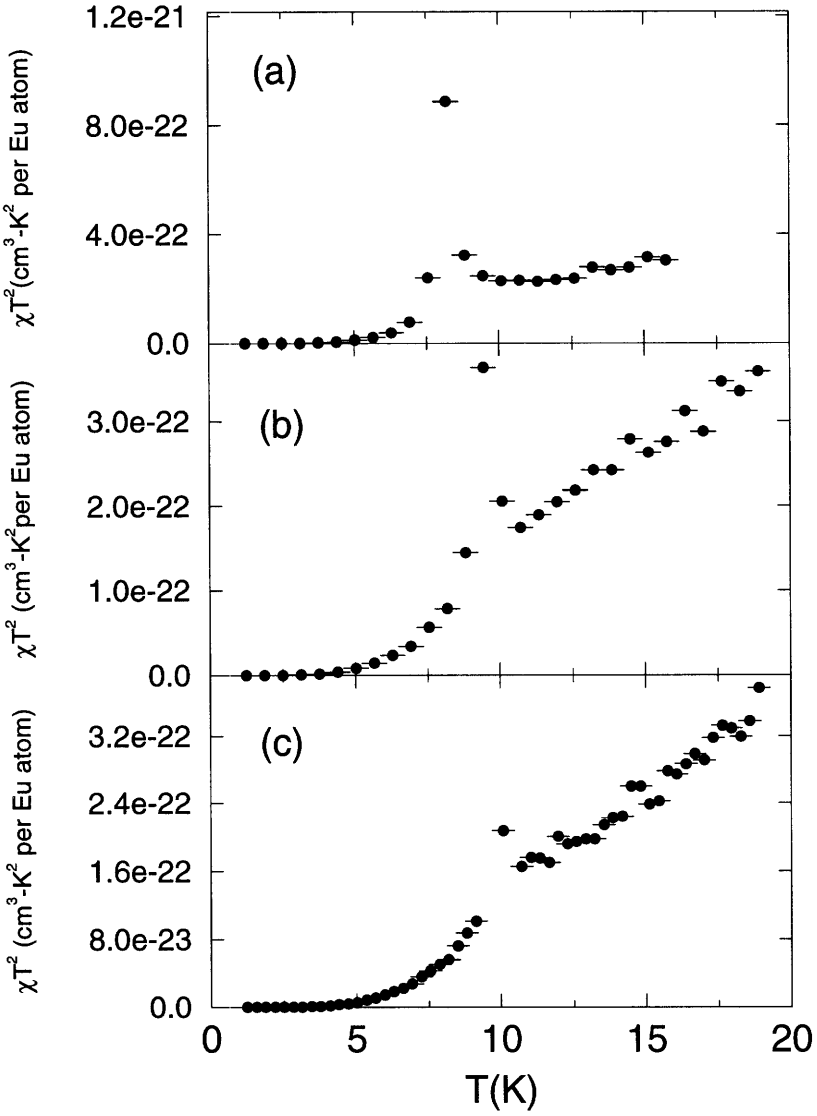

Figure 7-6: $\chi_{\|}(T)T^2$ vs. T for an EuTe(3)/PbTe(9) SL of dimensions 30x30x3 (a), an EuTe(5)/PbTe(15) SL of dimensions 30x30x5 (b), and an EuTe(7)/PbTe(21) SL of dimensions 30x30x7 (c). The straight-line like behavior for T greater than the temperature of the divergence of $\chi_{\|}(T)$ suggests Curie-Weiss paramagnetic behavior. Again, the notation 1.2e-21 denotes 1.2×10^{-21}.

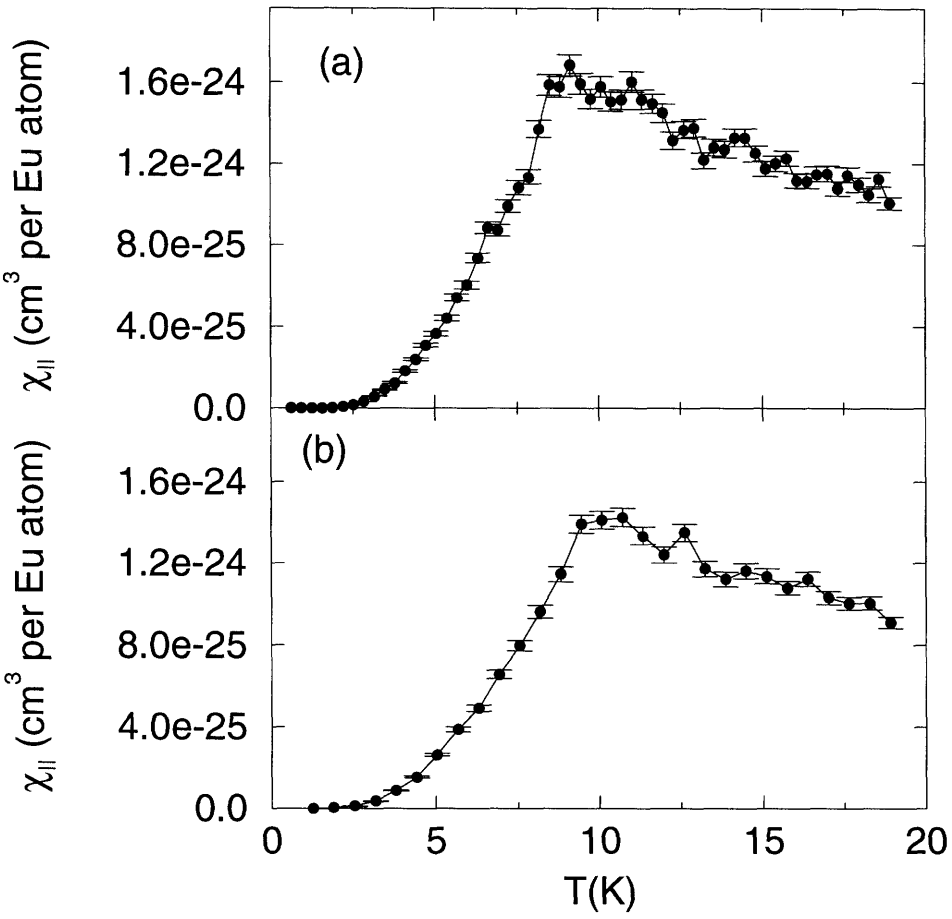

Figure 7-7: $\chi_{\|}(T)$ vs. T for an EuTe(4)/PbTe(12) SL of dimensions 30x30x4 (a), an EuTe(6)/PbTe(18) SL of dimensions 30x30x6 (b). Each of these two simulations uses 500 Monte Carlo scans for equilibriation, and 2000 Monte Carlo scans for sampling at each temperature. The notation 1.6e-24 represents 1.6×10^{-24}.

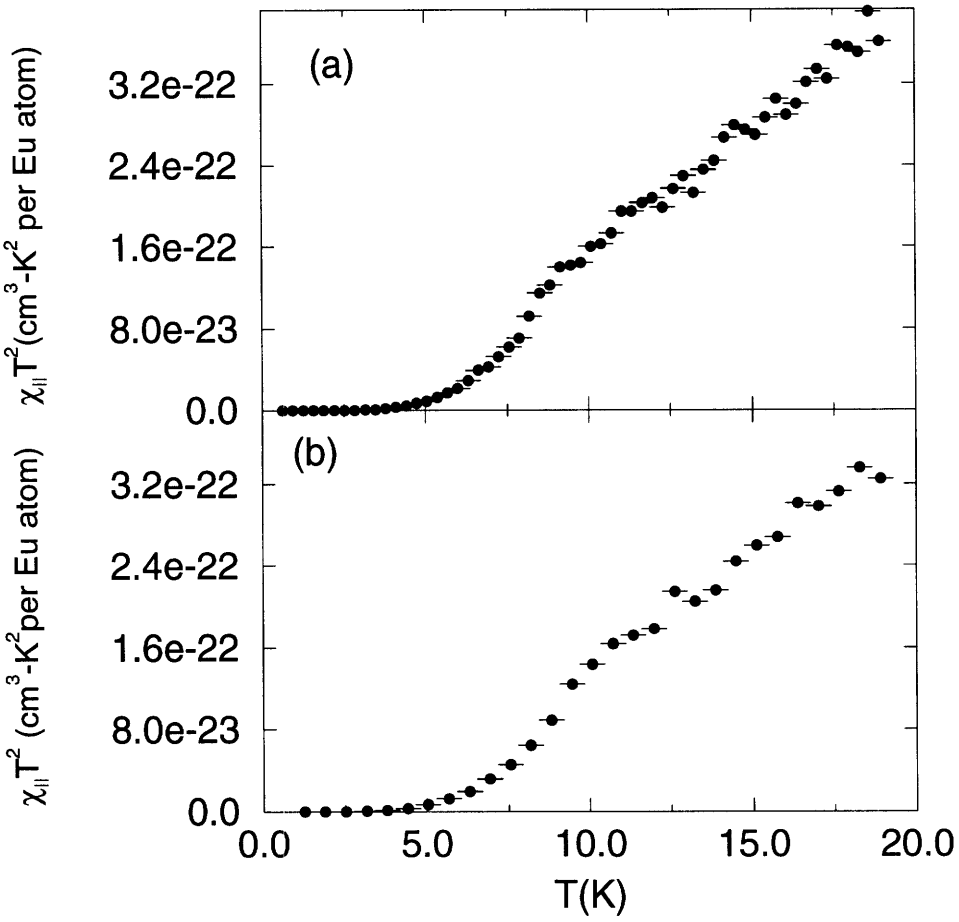

Figure 7-8: $\chi_{\|}(T)T^2$ vs. T for an EuTe(4)/PbTe(12) SL of dimensions 30x30x4 (a), and an EuTe(6)/PbTe(18) SL of dimensions 30x30x6 (b), in accordance with Fig.7-7. The notation 3.2e-22 denotes 3.2×10^{-22}.

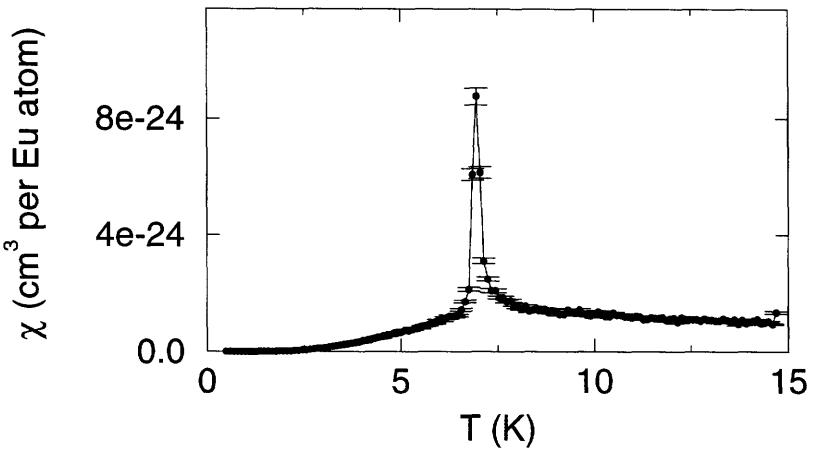

Figure 7-9: $\chi_{\|}(T)$ vs. T for an EuTe(4.86)/PbTe(12) SL of dimensions 60x60x4.86 (see text). The notation 8e-24 denotes 8×10^{-24}.

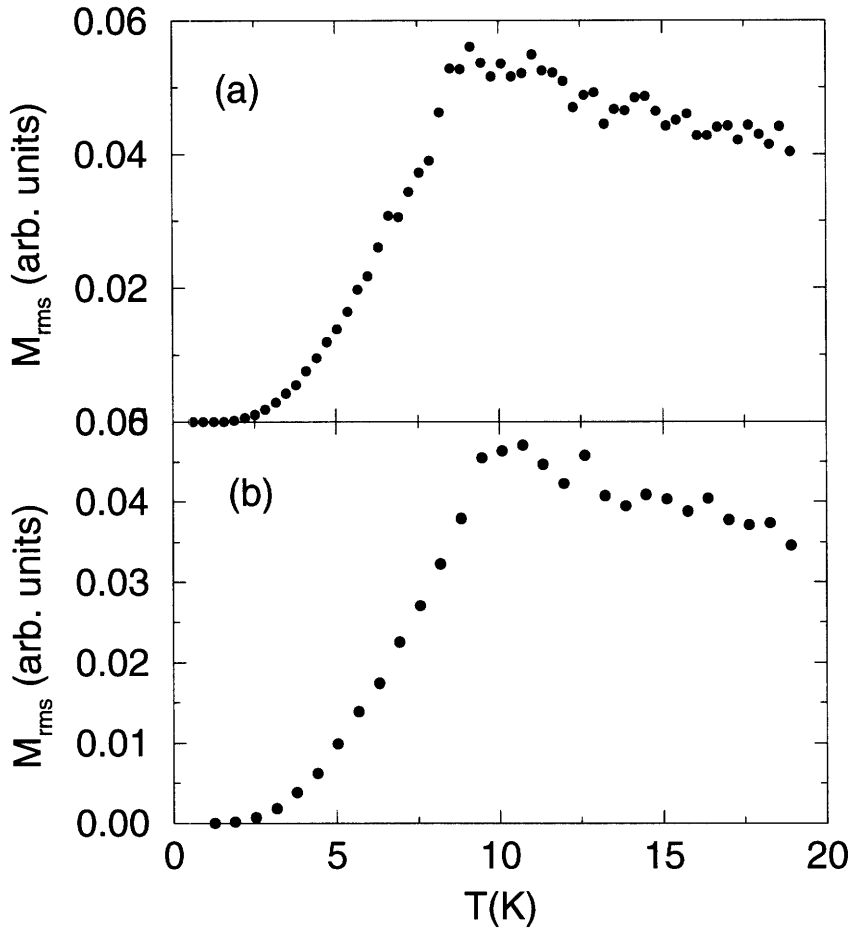

Figure 7-10: Calculated $M_{rms}(T)$ vs. T using a Monte Carlo Ising simulation for an EuTe(4)/PbTe(12) SL of dimensions 30x30x4 (a), and an EuTe(6)/PbTe(18) SL of dimensions 30x30x6 (b) in a 4 gauss external field (see text).

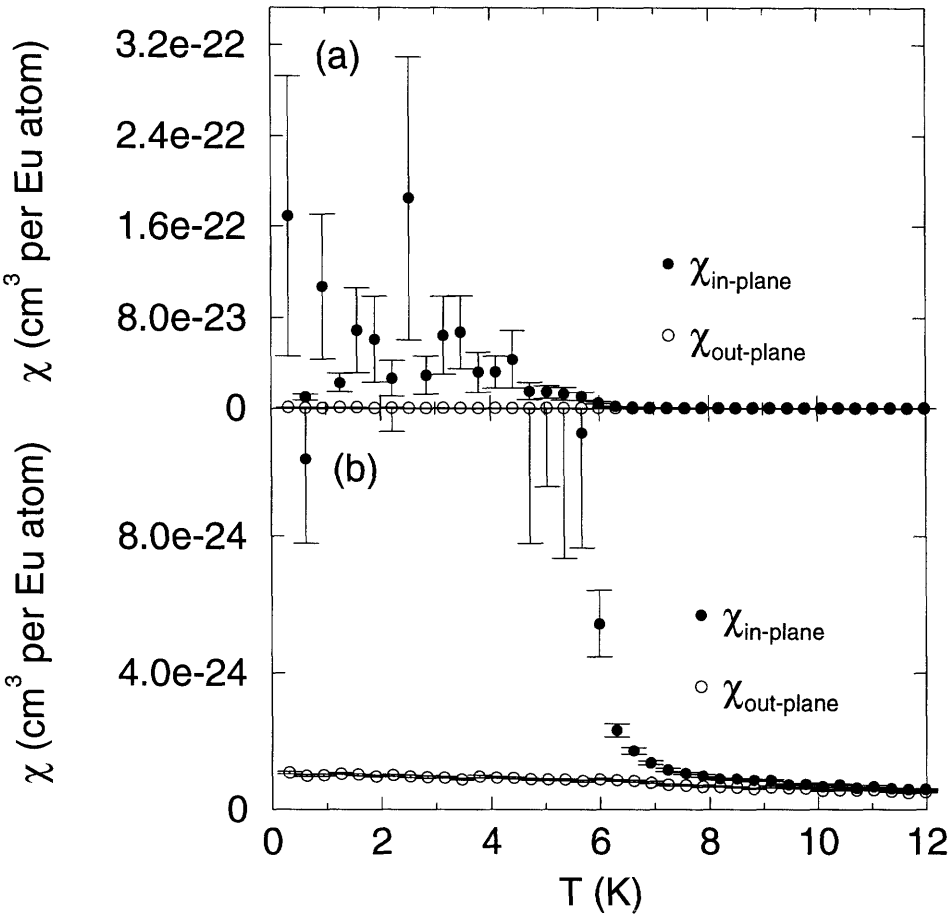

Figure 7-11: χ_{in} (closed circles) and χ_{out} (open circles) vs. T for an EuTe(3)/PbTe(9) SL (a). Large error bars in χ_{in} reflect the instability of the χ_{in} calculations at low tempertures. A zoomed-in plot of χ_{in} (closed circles) and χ_{out} (open circles) vs. T for the same EuTe(3)/PbTe(9) SL (b). These results are obtained from a lattice of $13\times13\times3$ spins using a Heisenberg model with dipolar forces. At each temperature, 2000 Monte Carlo steps are used for equilibriation and 2000 Monte Carlo steps for sampling. The notation 3.2e-22 denotes 3.2×10^{-22}.

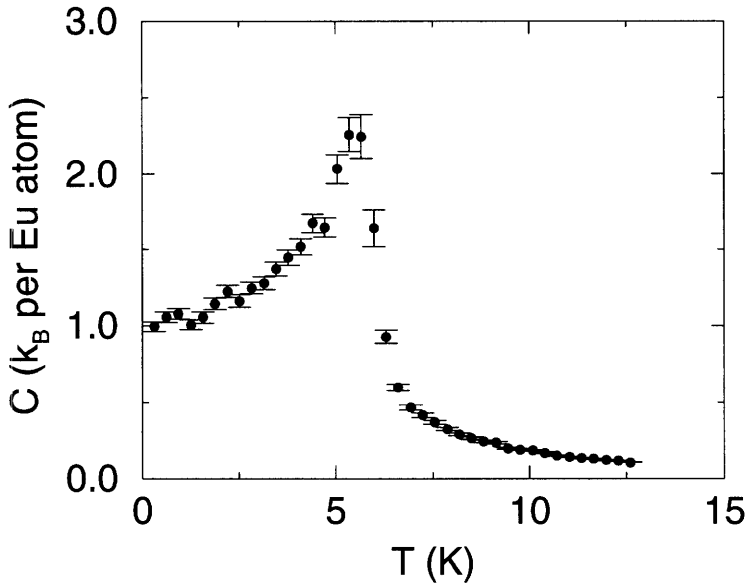

Figure 7-12: Simulated specific heat C vs. T for the same Heisenberg model calculation for the EuTe(3)/PbTe(9) SL as is shown in Fig. 7-11. The temperature at which C diverges can be identified as the transition temperature T_c.

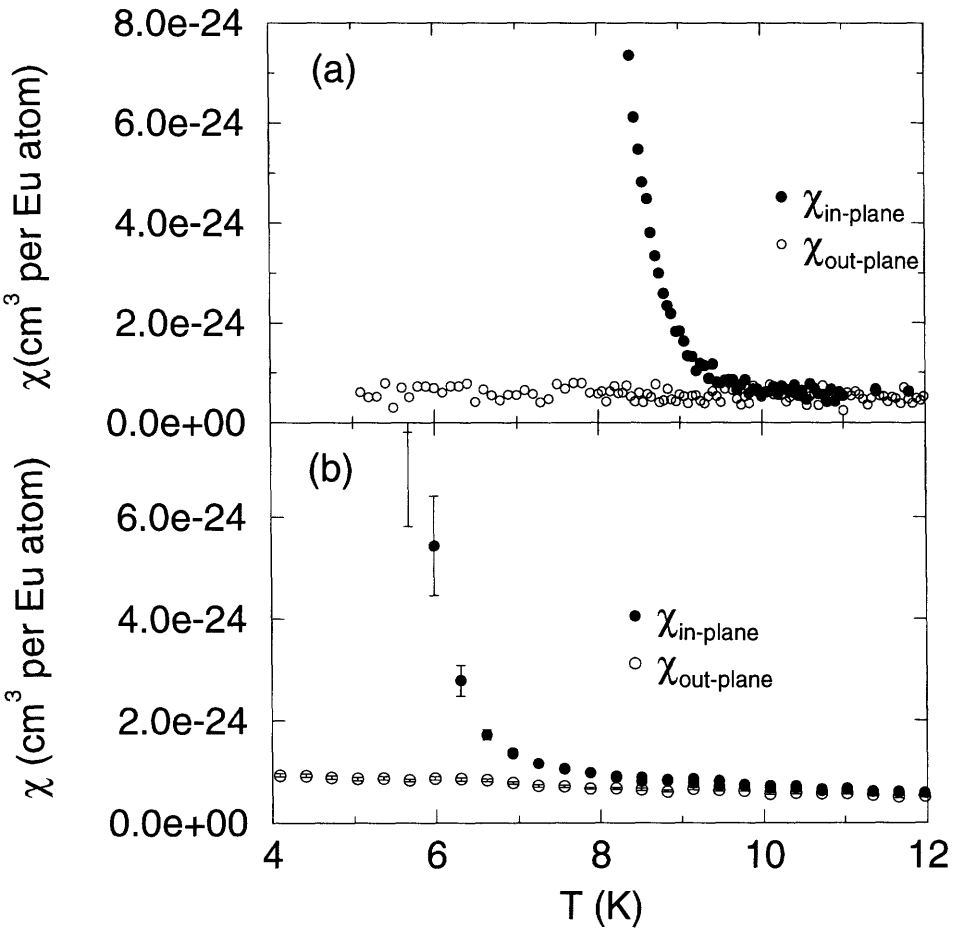

Figure 7-13: Experimental χ_{in} (closed circles) and χ_{out} (open circles) vs. T for an EuTe(3)/PbTe(9) SL (a), compared with the simulated χ_{in} (closed circles) and χ_{out} (open circles) vs. T for an EuTe(3)/PbTe(9) SL (b) in the temperature region $T>T_c$. The notation 8.0e-24 denotes 8.0×10^{-24}.

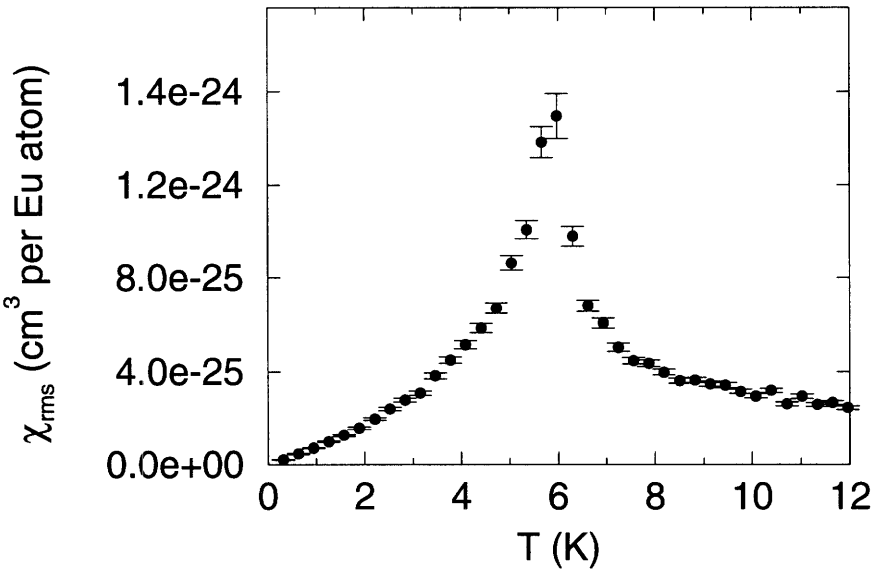

Figure 7-14: Simulated χ_{rms} vs. T for an EuTe(3)/PbTe(9) SL based on a Heisenberg model. Notice that χ_{rms} peaks at about the same temperature as the specific heat C diverges (see Fig.7-12). The χ_{rms} simulation is obtained from a lattice of $13\times13\times3$ spins using the Heisenberg model with dipolar forces. At each temperture, 2000 Monte Carlo steps for equilibration, and 2000 Monte Carlo steps are used for sampling. The notation 1.4e-24denotes 1.4×10^{-24}.

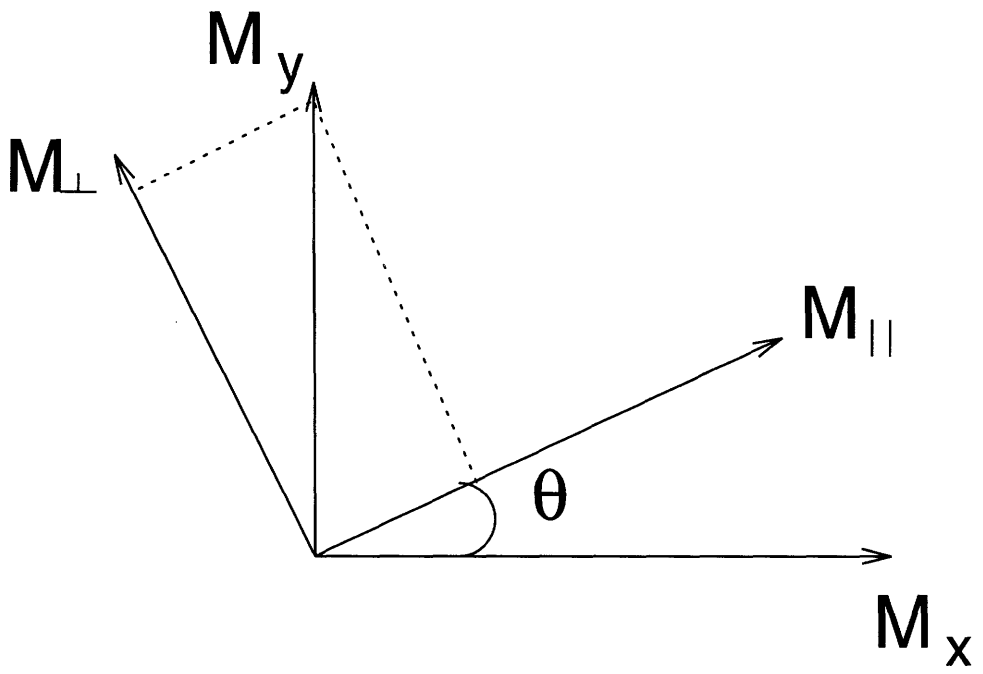

Figure 7-15: Geometry of the $M_\perp$ and $M_\parallel$ components of the magnetization in relation to M_x, and M_y, and the average angle θ.

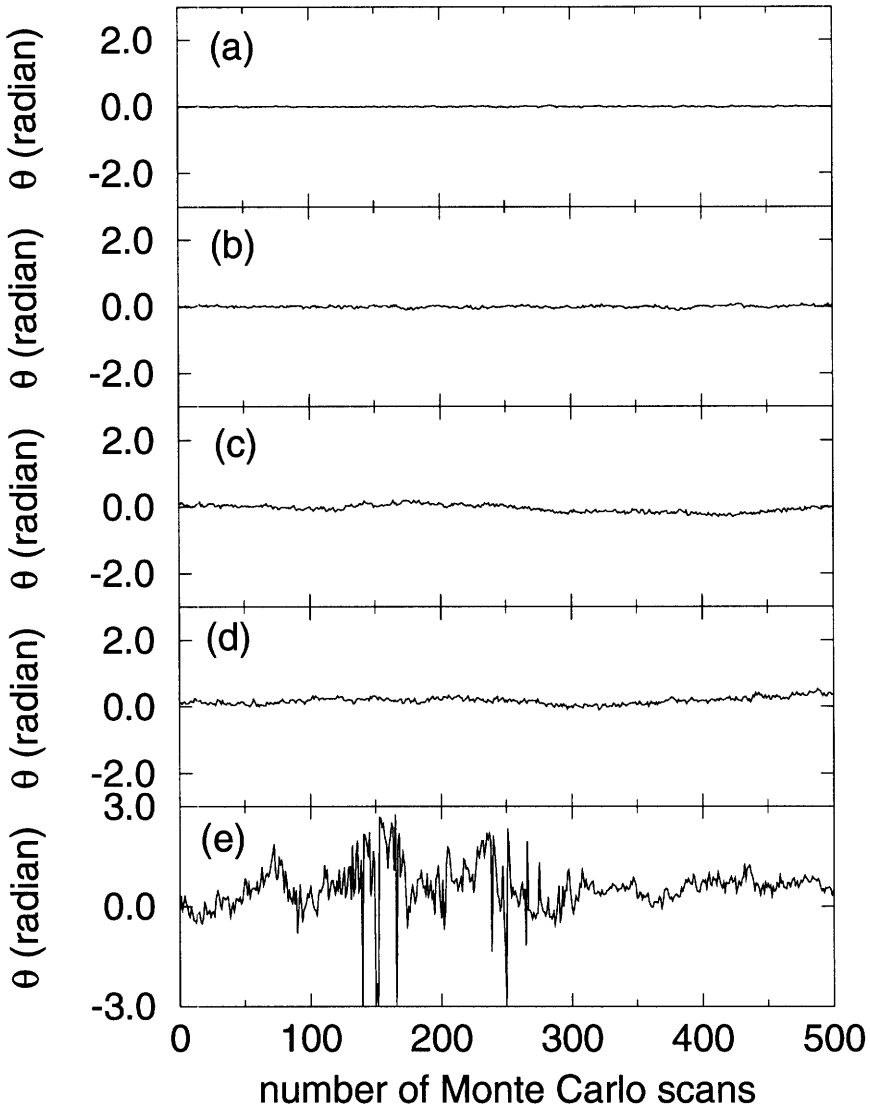

Figure 7-16: Magnetization direction vs. the number of Monte Carlo scans for an EuTe(3)/PbTe(9) SL at 1.3 K (a), 1.9 K (b), 2.5 K (c), 3.2 K (d), and 3.8 K (e).

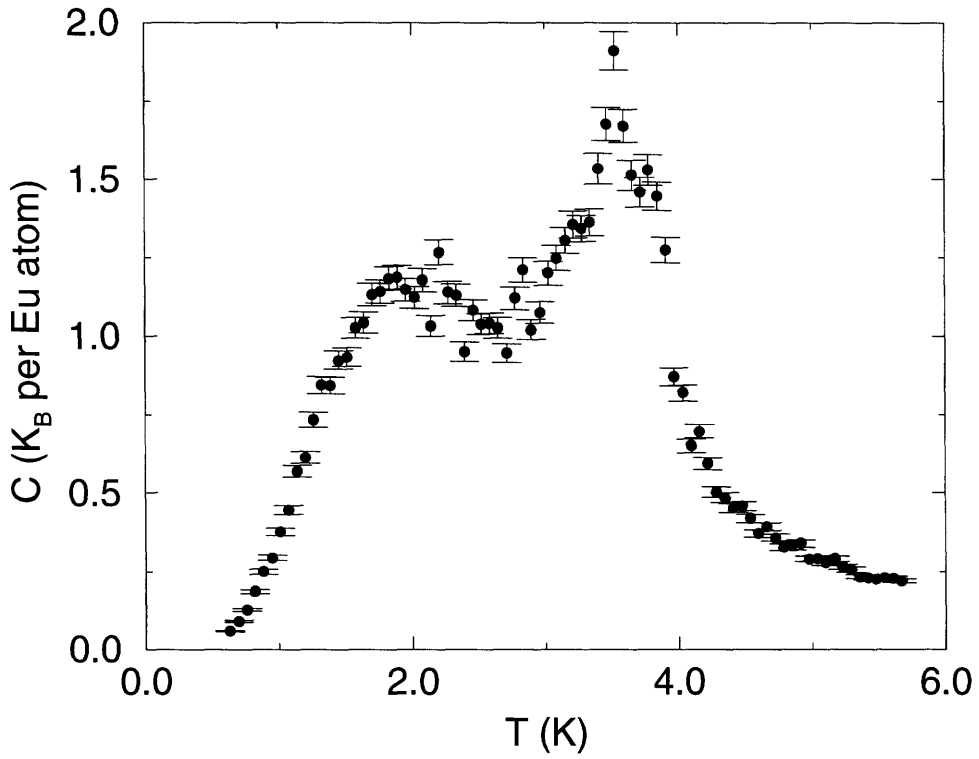

Figure 7-17: Specific Heat C vs. T for an EuTe(3)/PbTe(9) SL using the Clock model. We use the peak in C to determine the transition temperature T_c as 3.4 K.

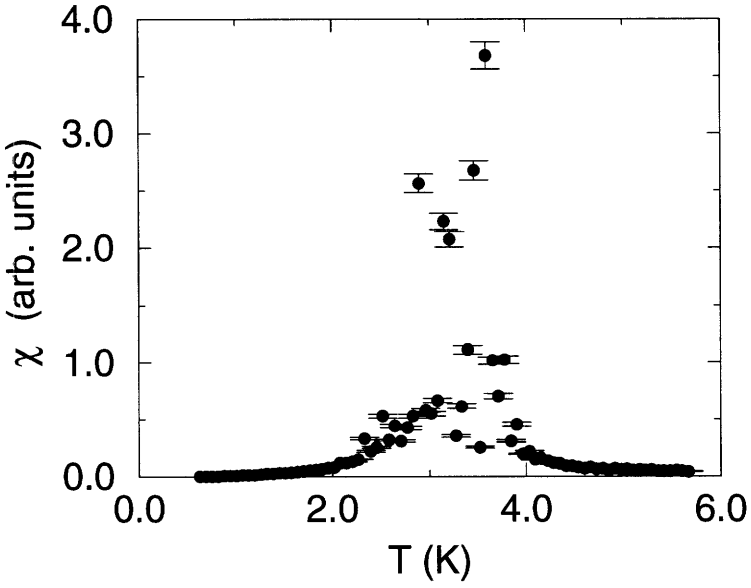

Figure 7-18: Monte Carlo simulation of $\chi_\perp$ vs. T for an EuTe(3)/PbTe(9) SL using the Clock model with 6-fold symmetry.

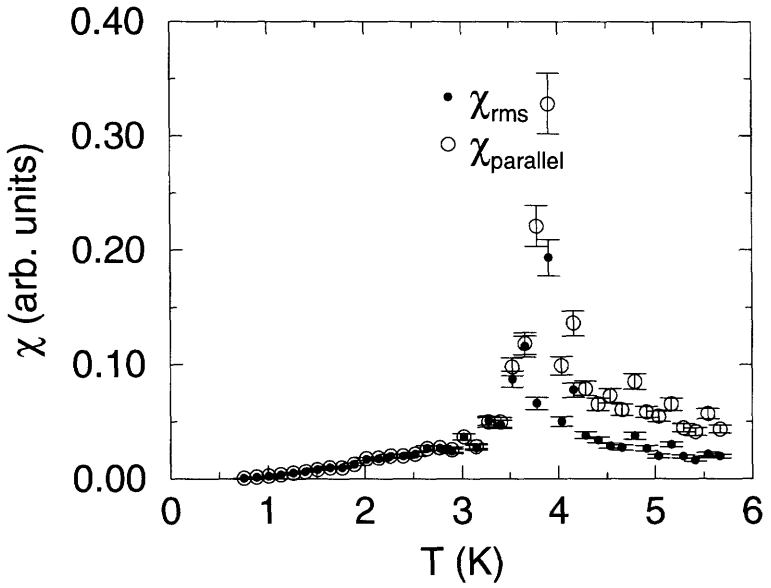

Figure 7-19: Monte Carlo simulations of $\chi_{\|}$ (open circles) and χ_{rms} (closed circles) vs. T for an EuTe(3)/PbTe(9) SL using the Clock model with 6-fold symmetry.

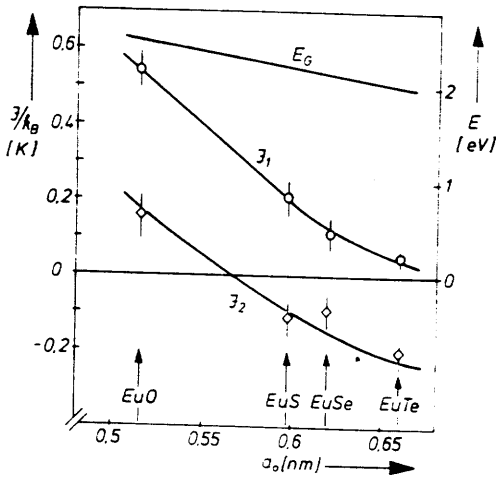

Figure 7-20: Values of the exchange couplings J_1 and J_2 for various europium chalcogenides as a function of the lattice constant.[50]

Chapter 8

Conclusions and Future Work

8.1 Conclusions

In general when a bulk magnet has been reduced to several atomic layers in thickness while maintaining its macroscopic dimensions in the x and y directions, the magnetic properties change dramatically, as we have seen in our EuTe/PbTe SLs. High quality MBE grown EuTe/PbTe SLs embody the experimental realization of an ideal 2D Heisenberg antiferromagnet with localized spins and isotropic exchange interactions. Therefore, the magnetic studies of EuTe/PbTe SLs are of great interest and importance from a basic research point of view. In this section, we summarize the key results on the magnetic studies of these SLs in three experimental areas: neutron scattering, static magnetization, and zero field susceptibility.

Neutron diffraction measurements have unambiguously identified that the magnetically ordered phase in the EuTe/PbTe SLs (with $\xi \geq 2$) is that of a type-II antiferromagnet, the same as the magnetically-ordered phase of bulk EuTe. Unlike bulk EuTe, only a single (111) magnetic domain exists in the EuTe/PbTe SLs, a direct consequence of the SL structure and dipole interactions.

As we have seen in the studies of EuTe/PbTe SLs, the temperature-dependence of the magnetization varies continuously as the EuTe layer thickness ξ increases from one to seven among the SLs we have studied. Specifically, ferromagnetic-like behavior in $M(T)$ is observed for the EuTe(3)/PbTe(9), EuTe(5)/PbTe(15) and

EuTe(7)/PbTe(21) SLs, whereas antiferromagnetic-like behavior is seen for the ξ=even EuTe(4)/PbTe(12) and EuTe(6)/PbTe(18) SLs. We have attempted to use both a mean-field approach and Monte Carlo simulations to quantitatively describe these $M(T)$ measurements.

From the zero field susceptibility measurements we have observed the divergent behavior in χ_{in} and the anisotropy between χ_{in} and χ_{out} for SLs with $\xi \geq 3$. A Heisenberg model with dipolar interactions is successful in explaining those two features. Furthermore, Monte Carlo simulations using the same model show that dipolar interactions can stabilize long-range antiferromagnetic order in EuTe/PbTe SLs. EuTe/PbTe SLs to our knowledge represent the first experimental realization of long-range order stabilized in a 2D Heisenberg spin system by dipolar interactions.

8.2 Indications for Future Research

From what we already know about the magnetic properties of EuTe/PbTe SLs, we can readily extend our research on these SLs in several directions.

The first research interest will be to measure the zero field susceptibility of an EuTe(1)/PbTe(3) SL down to lower temperatures and compare that to the 2D Heisenberg model, albeit there may be some influences due to dipole interactions.

Another project is to study the $M(H)$ of SLs with ξ=15 and 16 for $T<T_c$. The focus here is to test the theory on the surface spin-flop transition. A theory was presented by Keffer and Chow,[74] who argued that the surface spin-flop state evolves continuously into the bulk spin-flop phase. Recent experiment and theory developed by Wang and Mills,[75] suggest some differences in the surface spin-flop transition process between a SL with an even number of monolayers and a SL with an odd number of monolayers. The evolution from a surface spin-flop state to a bulk spin-flop phase requires certain minimum thicknesses for SL samples. The work of Wang and Mills suggests that ξ=15 and 16 are appropriate for this purpose.[75]

Another project is the study of the temperature-dependent neutron scattering of the EuTe(2)/PbTe(6) SL since the zero field susceptibility data for this SL sample

shows anomalous $\chi_{in}(T)$ behavior at temperatures above T_c.

Bibliography

[1] M. E. Fisher and D. Jasnow, Phys. Rev. B **3**, 907 (1971).

[2] L. Onsager, Phys. Rev. **65**, 117 (1944).

[3] J. M. Kosterlitz and D. J. Thouless, J. Phys. C **5**, L124 (1972).

[4] J. M. Kosterlitz and D. J. Thouless, J. Phys. C **6**, 1181 (1973).

[5] N. D. Mermin and H. Wagner, Phys. Rev. Lett. **17**, 1133 (1966).

[6] R. J. Birgeneau, H. J. Guggenheim, and G. Shirane, Phys. Rev. Lett. **22**, 720 (1969).

[7] L. J. de Jongh and A. R. Miedema, in *Experiments on Simple Magnetic Model Systems*, (Taylor & Francis Ltd London, 1974).

[8] S. V. Maleev, Sov. Phys. JETP **43**, 1240 (1976).

[9] P. W. Anderson, Science **235**, 1196 (1987).

[10] J. G. Bednorz and K. A. Muller, Z. Phys. **B64**, 189 (1986).

[11] T. Barnes, International Journal of Modern Physics C **2**, 659 (1991).

[12] L. M. Falicov, Physics Today **45**, 46 (1992).

[13] R. F. C. Farrow, in *Magnetism and Structure in Systems of Reduced Dimensions*, (Plenum Press New York, 1993), Vol. 309. NATO ASI series B.

[14] P. K. Streit and G. E. Everett, Phys. Rev. B **21**, 169 (1980).

[15] P. Wachter, in *Handbook on the Physics and Chemistry of Rare Earths*, (North-Holland Publishing Company, Amsterdam, 1979).

[16] P.W. Anderson, in *Magnetism*, chapter 2, (Academic Press, 1963).

[17] J. Heremans and D. L. Partin, Phys. Rev. B **37**, 6311 (1988).

[18] D. Kostyk, Y. Shapira, E. McNiff Jr, T. Q. Vu, and A. Twardowski, Solid State Commun. **92**, 473 (1994).

[19] D. L. Partin, J. Electron. Mater. **13**, 493 (1984).

[20] G. Bauer, Surface Science **168**, 462 (1986).

[21] G. Bauer, Semicond. Sci. Technology **5**, 122 (1990).

[22] G. Springholz, in *MBE Growth of Lead Salt IV-VI Semiconductors*, (Johannes Kepler University Linz Austria, 1994). PhD Thesis.

[23] G. Springholz and G. Bauer, Phys. Rev. B **48**, 10998 (1993).

[24] G. Springholz and G. Bauer, J. Appl. Phys. **77**, 540 (1995).

[25] C.W. Snyder, B.G. Orr, D. Kessler, and L.M. Sander, Phys. Rev. Lett. **66**, 3032 (1991).

[26] D.J. Srolowitz, Acta Metall. **37**, 621 (1989).

[27] G. Springholz, N. Frank, and G. Bauer, Appl. Phys. Lett. **64**, 2970 (1994).

[28] J.W. Matthews and A.E. Blakeslee, J. Cryst. Growth **27**, 118 (1974).

[29] N. Frank, G. Springholz, and G. Bauer, Phys. Rev. Lett. **73**, 2236 (1994).

[30] M. Shima, L. Salamanca-Riba, G. Springholz, and G. Bauer, Symposium on the Evolution of Epitaxial Structure and Morphology, Fall MRS 1995 (1995).

[31] Z. Wilamowski W. Jantsch and G. Springholz, Materials Science Forum **182-184**, 669 (1995).

[32] J.M. Gallego, S. Kim, T.J. Moran, D. Lederman, and I.K. Schuller, Phys. Rev. B **51**, 2550 (1995).

[33] I.K. Schuller, Phys. Rev. Lett. **44**, 1597 (1980).

[34] G.E. Bacon, in *Neutron Diffraction*, (Clarendon Press, Oxford, 1975). An introductory overview of magnetic neutron diffraction and general reference on the subject.

[35] G. Will, S. J. Pickart, A. Alperin, and R. Nathans, Phys. Chem. Solids **24**, 1679 (1963).

[36] M. B. Salamon, Shantanu Sinha, J. J. Rhyne, J. E. Cunningham, R. W. Erwin, J. Borchers, and C. P. Flynn, Phys. Rev. Lett **56**, 259 (1986).

[37] C. F. Majkrzak, J. W. Cable, J. Kwo, M. Hong, D. B. McWhan, Y. Yafet, J. V. Waszczak, and C. Vettier, Phys. Rev. Lett. **56**, 2700 (1986).

[38] T.M. Giebultowicz, V. Nunez, G. Springholz, G. Bauer, J. Chen, M.S. Dresselhaus, and J.K. Furdyna, J. Magn. Magn. Matt. **140-144** (1995).

[39] A. P. French, in *Vibrations and Waves*, (W. W. Norton & Company Inc. New York, 1970).

[40] K. E. Meyer, G. P. Felcher, S. K. Sinha, and Ivan K. Schuller, J. Appl. Phys. **52**, 6608 (1981).

[41] Quantum Design Inc., in *MPMS5 User's Manual 1993*, (Quantum Design Inc, 1993).

[42] J.C. Gallop, in *SQUIDs, the Josephson Effects and Superconducting Electronics*, chapter 3, (Adam Hilger, 1991).

[43] J. W. Battles and G. E. Everett, Phys. Rev. B **1**, 3021 (1970).

[44] J. I. Kaplan, J. Chem. Phys. **22**, 1709 (1954).

[45] F. Keffer and W. O'Sullivan, Phys. Rev. **108**, 637 (1957).

[46] Y.A. Izyumov and R. P. Ozerov, in *Magnetic Neutron Diffraction*, page 28, (Plenum Press New York, 1970).

[47] D. S. Rodell, I. S. Jacobs, and J. Owen, Phys. Rev. Lett. **11**, 10 (1963).

[48] M. E. Fisher, Phil. Mag. **7II**, 1731 (1962).

[49] A. S. Carrico and R. E. Camley, Phys. Rev. B **45**, 13117 (1992).

[50] R. W. Wang and D. L. Mills, Phys. Rev. B **46**, 11681 (1992).

[51] C. Kittel, in *Introduction to Solid State Physics*, (John Wiley and Sons New York, 1986).

[52] W. Zinn, J. Magn. Magn. Mater. **3**, 23 (1976).

[53] C. A. Ramos, D. Lederman, A. R. King, and V. Jaccarino, Phys. Rev. Lett. **65**, 2913 (1990).

[54] J. A. Borchers, M. J. Carey, R. W. Erwin, C. F. Majkrzak, and A. E. Berkowitz, Phys. Rev. Lett. **70**, 1878 (1993).

[55] T. M. Giebultowicz, P. Klosowski, N. Samarth, H. Luo, J. K. Furdyna, and J. J. Rhyne, Phys. Rev. B **48**, 12817 (1993).

[56] T. M. Giebultowicz, W. Faschinger, V. Nunez, P. Klosowski, G. Bauer, H. Sitter, and J. K. Furdyna, J. Crystal Growth **138**, 877 (1994).

[57] Robert M. White, in *Quantum Theory of Magnetism*, (Berlin and New York and Springer-Verlag, 1983).

[58] N. F. Oliveira, S. Foner, Y. Shapira, and T. B. Reed, Phys. Rev. B **5**, 2634 (1972).

[59] E. L. Nagaev, in *Physics of Magnetic Semiconductors*, page 63, (Mir Publishers Moscow, 1983).

[60] Quantum Design Inc., in *MPMS User's Manual*, (Quantum Design Inc, 1994).

[61] J.J. Chen, G. Dresselhaus, M. S. Dresselhaus, G. Springholz, C. Pichler, and G. Bauer, Phys. Rev. B **54** (1996).

[62] C. Kittel, in *Introduction to Solid State Physics*, page 446, (John Wiley and Sons New York, 1986).

[63] M. E. Fisher, Am. J. Phys. **32**, 343 (1964).

[64] Alan D. Sokal, in *Monte Carlo Methods in Statistical Mechanics: Foundations and New Algorithms*, (New York University Press, 1989).

[65] N. Metropolis, A. W. Rosenbluth, M. N. Rosenbluth, A. H. Teller, and E. Teller, J. Chem. Phys. **21**, 1087 (1953).

[66] M. B. Priestley, in *Spectral Analysis and Time Series*, (Academic Press London, 1981). Chapters 5-7.

[67] D. Stauffer, F. W. Hehl, V. Winkelmann, and J. G. Zabolitzky, in *Computer Simulation and Computer Algebra*, (Springer-Verlag Berlin, 1988).

[68] Rodney J. Baxter, in *Exactly Solved Models in Statistical Mechanics*, page 308, (Academic Press, 1982).

[69] Editor and K. Binder, in *Monte Carlo Methods in Statistical Physics*, (Springer-Verlag Berlin, 1986).

[70] R. E. Watson, M. Blume, and G. H. Vineyard, Phys. Rev. B **2**, 684 (1970).

[71] D. P. Landau, Phys. Rev. B **13**, 2997 (1976).

[72] John W. Negele and Henri Orland, in *Quantum Many-Particle Systems*, chapter 8, pages 408–410, (Addison Wesley, 1988).

[73] L. Bergomi, (). to be published.

[74] F. Keffer and H. Chow, Phys. Rev. Lett. **31**, 1061 (1973).

[75] R. W. Wang, D. L. Mills, E. E. Fullerton, J. E. Mattson, and S. D. Bader, Phys. Rev. Lett. **72**, 920 (1994).